Numerical Simulation of a single emitter colloid thruster in pure droplet cone-jet mode

by

Jorge Alejandro Carretero Benignos

Submitted to the Department of Mechanical Engineering in partial fulfillment of the requirements for the degree of

Doctor of Philosophy

at the

MASSACHUSETTS INSTITUTE OF TECHNOLOGY

February 2005

Author .....
Department of Mechanical Engineering
December 10, 2004

Certified by .....
Manuel Martínez-Sánchez
Professor, Aeronautics and Astronautics
Thesis Supervisor

Read by .....
Ain Sonin
Professor, Mechanical Engineering
Committee Chair

Accepted by .....
Lallit Anand
Chair, Committee on Graduate Students

Numerical Simulation of a single emitter colloid thruster in pure droplet cone-jet mode

by

Jorge Alejandro Carretero Benignos

Submitted to the Department of Mechanical Engineering
on Dec 10, 2004, in partial fulfillment of the
requirements for the degree of
Doctor of Philosophy

Abstract

New Scientific missions call for emerging propulsion technologies capable of fine tuning a satellite's relative position and cancelling small disturbances. One candidate technology that holds promise for these type of missions are colloidal thrusters. These thrusters are electrostatic accelerators which do not rely on gas ionization (plasma), are intrinsically small, and operate at low power levels, while having small plume divergence angles to avoid spacecraft (S/C) contamination problems. Colloid thrusters deliver low thrust (0.1 μN/emitter) which can be multiplied many times over by integrating them in microfabricated arrays. An important advantage is that with proper choice of propellant and operating regime their specific impulse can be tailored from 500-7000 seconds making them viable candidates for a multitude of mission profiles.

In the past many research groups have worked on developing colloid thrusters; however, their basic physics are still not completely understood. For this reason, we have undertaken the development of a numerical simulation of a colloid thruster to complement experimental and analytical research in the area. The goal of this project has been to create a flexible numerical tool to compute single-emitter current, droplet size, velocity, electric field strengths for a given geometry, fluid, flow rate, and voltage.

We have approached this issue from the numerical perspective by developing a simulation of a colloid thruster operating in the single cone-jet pure droplet mode. Our numerical simulation models the cone-jet transition region of the colloid jet; starting from the needle up to the extractor grid, thus reproducing a typical electrospray experimental configuration. The liquid is modelled as an incompressible viscous fluid with constant conductivity. Surface charge relaxation effects are included, and the potential and electric fields are solved for. The equations have been simplified by employing a slenderness approximation except for the free surface boundary conditions where the terms have been kept exact, in order to reproduce the Taylor cone shape correctly.

Simulation results are shown to compare well to experimental data for a variety of liquids, and flow rates. In more detail, this thesis presents (a) results for a broader parametric range than previously published materials; (b) careful comparison to available experimental data and scalings proposed by several authors; (c) validation of several simple sub-models for the cone and jet sections; (d) analysis of length scales in the cone-jet transition region; (e) clarification of the role of relative permittivity for the range 7-110; (f) discussion of electrode geometry and counter-electrode effects; (g) preliminary results for the onset of ion evaporation.

Thesis Supervisor: Manuel Martínez–Sánchez
Title: Professor Aero & Astro, MIT

Thesis Supervisor: Akintunde Ibitayo Akinwande
Title: Professor EECS, MIT

Thesis Supervisor: Vlad Hruby
Title: President, Busek, Co.

Thesis Supervisor: Ain Sonin
Title: Chairman, Department of Mechanical Engineering

Acknowledgments

"Men wanted for hazardous journey. Small wages, bitter cold, long months of complete darkness, constant danger, safe return doubtful. Honor and recognition in case of success."
Atributed to Sir Ernest Shackleton, Imperial Transantarctic Expedition, 1914

An adventure indeed, and what an adventure!!!

First, I would like to thank my advisor Professor Manuel Martínez-Sánchez. He has been the best advisor I could have ever hope to have. Not only is he an extraordinarily gifted scientist but, perhaps more importantly a good honest man, who genuinely cares for his students. Thanks for letting me be part of your research group and for being always there when I needed help. Also many thanks are due to Professor Sonin, who throughout these years has been a great example. To Professor Tayo Akinwande, thanks for all your insights, help during this project, and for teaching me the finer details of Nigerian spanish. A special word for Dr. Vlad Hruby who graciously agreed to be part of my committee at the eleventh hour. Thanks Vlad!

Tatsuo once said that our office is the sunniest windowless office at MIT. He was definitely right. Especial thanks are due to the people that have made this experience so enjoyable: Mr. Blateau, for being a great friend and teaching me words in French that I shouldn't have learned. Tatsuo Onishi, who put up with all my wookie noises and laughed as hard as he could to all my bad jokes!. Paulo Lozano one of my best friends (the authentic SPL man) with whom sharing the office has always been a pleasure and lots of fun. Shannon "turtle " thanks for everything, you are one of my best friends and someone I could always count on to cheer up the day, thanks so much. Good Old Mark Santi, the man himself thanks for the great times we had here, at conferences, and in Europe... what a great trip. Kay, thanks for the amazing time we had in France, and here in the office. It is good to know someone who can catch every quote as obscure as it may be. Karen, thanks so much for the great coffees we have had. Noah, Yassir, and Ollie, the coolest SPL outpost in SSL land, thanks guys!. Finally, thanks to the rest of SPL. This is a great lab!!

Thanks to the Baty's, Kate and Gordon, who adopted me and with whom I have shared so many good times. Thanks for everything!

My mexican friends. When you are so far away from home your friends become your

family. All I can say is that I have the best family I could ever hope to have. Rodrigo Quintero, thanks for being my first friend here, and a great one at that. Ante, Marcos, Ana Barbara, Julio, Ana, and Martin (not quite mexican, a bit on the swedish side!) thanks guys I couldn't have made it through the dark years of my master's degree without your support. To Raymundo, my best friend throughout this adventure, thanks I wouldn't have made it without your help. To the crowd of the Ph.D. years and the tribe of the Jorge's: Gina (que hace el mejor pastel de tres leches de la comarca), Jorge Feuchtwanger, Jorge "El Oso" Vieyra, Jorge Ulises, Juan González, Yeri, Laia, Nuria and the rest of the media lab gang.

To my friends of the triathlon club!, thanks for those early morning swims and runs. Thanks Miriam for organizing everything, you are amazing. Also thanks to the core group, Patricio, Brian, Ian, Dave, Leigh, Kim and Micha.

To all my friends in Aero&Astro, and specially to Dave Robertson and Fred Coté, friends whith whom it was always a pleasure to hang out with.

My friends in Puebla, sorry I have been away so long. Thanks Edgar, Gabriel, Diana, Yuria, Pliego, and Sam. Although, I usually see you guys only twice a year, I always have a great time down there. Thanks for supporting me all this time and always believing I could make it.

And finally to my family my mom Olga Alicia, my dad Jorge, and my brother Eduardo. I would have never been able to even try this without all your support and love. Los quiero muchísimo, y les estoy infinitamente agradecido por todo el cariño y amor que siempre me han dado. No hay palabras para agradecerles, y sepan que siempre, donde quiera que ande están en mi corazón y pensamiento. Siempre cerca. Esta tesis se la dedico a mis abuelos Herman, Olga Alicia, Alfonso y Evita. Y con mucho cariño a L. y G., pues esta tesis es para ustedes.

Esta tesis se termino de imprimir el día 3 de Febrero de 2005,
en los talleres Italgraff. Chabacano Num. 65, Local "A".
Mexico D.F.
La Edicion consta de pocos ejemplares
y sobrantes para reposición.

Contents

List of Figures

List of Tables

Allá en la fuente había un chorrito
Se hacía grandote, se hacía chiquito
Estaba de mal humor el pobre chorrito tenía calor...

Over there in the fountain,
there is a little spurt It gets very big, it gets very small
And he was very mad poor little spurt! he was so hot . . .

El Chorrito Cancion popular mexicana (mexican folk song),
de Francisco Gabilondo Soler "Cri-Cri"

Chapter 1

Introduction

In the last few years a shift in satellite/probe missions has taken place. This change has been motivated by new scientific, economic and administrative mission requirements. Changing needs for scientific missions call for high precision propulsion systems capable of fine tuning a satellite's relative position and cancelling small disturbances. From the economic standpoint, these satellites are now designed to increase cost savings, reliability, system redundancy and survivability for any given mission. It is within this realm that new concepts have emerged moving away from stand–alone satellites to constellations of miniature ones. Examples of this approach are the Emerald, SPHERES, and LISA missions. An important drive for these missions is the miniaturization of the individual satellites (1000 Kg) to the scale of microsatellites (100 Kg) and nanosatellites (10 Kg). As mentioned before many of these missions require very precise relative position control, for instance the LISA mission, calls for three satellites flying in formation with relative spacings of 5 million Kilometers controlled down to nanometers in order to measure gravitational waves. In these case, the job of the propulsion system is to cancel any extraneous perturbations which would otherwise affect the measurements. For these missions the thruster will have to be compact, fuel efficient, and will be most likely power limited. Electrical propulsion engines are ideal for these time insensitive and power limited maneuvers as they work at relatively high specific impulse ($I_{sp} > 500sec$), [34].

One technology that holds promise for these type of missions is that of colloidal thrusters. These thrusters are electrostatic accelerators which do not rely on gas ionization (plasma) are intrinsically small, and operate at low power levels, while having small plume divergence

angles to avoid spacecraft (S/C) contamination problems.

1.1 Motivation

Electrosprays and colloid thrusters have been heavily studied for many years. From these studies much of the basic physics of the phenomenon has been learned. However, the topic is far from exhausted and is an active research area. The motivation for our work stems from a need to obtain a more complete picture of the physics at work in the electrospray. The aim of this thesis is to develop a numerical simulation of the cone-jet operating mode. The goal of this project is to create a flexible numerical tool to compute single-emitter current, droplet size, velocity, electric field strengths and spreading rate for a given geometry, fluid, flow rate, and voltage. The wealth of information obtained from such a tool is expected to complement and to some extent help us gain a more complete understanding of this complex electrohydrodynamic behavior.

1.2 Challenges

Electrospray modelling is by itself a complex and fascinating subject. The complexity stems from the non-trivial interaction between the evolving non-linear fluid jet structure, its electrical charges, and accompanying electric field. This coupling manifests itself in the conical fluid structure from which the high speed jet emanates. It is that point, where the cone transforms into a jet, the so called transition that lies at the core of this work. The challenge is to model this transition region including the relevant fluid, and electrostatic behavior. The transition from the cone to the jet section reduces the jet radius by an order of a 100. This important length scale change makes for a stiff mathematical and numerical problem.

From a physics perspective, this region bridges the gap between two dissimilar flow regimes, i.e. from a low speed conduction current controlled cone to high speed convection current controlled jet. A further complication is that being a free surface problem, the shape of the cone and jet are part of the solution and is in turn affected by the coupling of the flow physics and electrostatics. In other words it is a fascinating problem.

One important issue has is that it has been made a point to do so without relying on asymptotic estimates and other approximations. These approximations are very useful,

but their reliance on assumptions may make them true only for certain conditions and or regimes. The hope is that our work will help to confirm existing analytical estimates, and asymptotic expressions, while pointing out some of their limitations, thus serving as a stepping ground for other studies.

1.3 Contributions

Other numerical studies of this phenomenon have been published in the past. These works although they have targeted the same basic phenomenon, have focused for the most part on other operating regimes and lower conductivity liquids.

The contributions of this work are as follows :

1. A broader parametric range than previously published materials,
2. Careful comparison to available experimental data including $f(\epsilon)$, I *vs* V,and I *vs* Q
3. Validation of several simple sub-models, for the cone and jet section
4. Analysis of length scales in the transition region
5. Analysis of energy usage by the cone-jet.
6. Study of electrode spacing effects and needle boundary conditions
7. Integration of an ion evaporation model used to explore the mixed regime

In more detail, we have successfully compared our results to existing current scalings by Fernández de la Mora and Loscertales, as well as those by Gañán-Calvo. Simulations have been carried for many liquids spanning over an order of magnitude variations in surface tension, viscosity, relative permittivity and conductivity. Our results suggest, as originally predicted by Gañán-Calvo and other authors, that the liquid relative permittivity may not play a role in current scalings.

We have carried out various parametric studies with our simulation, some of those results are highlighted next. Our numerical results have successfully reproduced the almost linear voltage vs current behavior seen experimentally by Gamero *et al*, [52]. Furthermore, our simulation has shown that if the applied voltage is reduced beyond 20 % of the starting voltage the cone-jet becomes unstable as seen experimentally. Our results have been used to

evaluate the length scales proposed for several authors for the transition region. Our results show that the best agreement is obtained with R_g, [17]. On a side note, our comparisons for the transition region with the various length scales, reproduce the trends observed by Gamero and Hruby for the jet breakup radius scaling, [22]. We present the energy breakdown for the cone-jet, for various liquids and flow rates. The detailed information obtained for the cone and jet sections has been used to estimate the accuracy of simplified submodels for the E-field, and jet radius.

Other results have shown, as expected, that electrode distance is a secondary variable with weak effect on emitted current. Similar numerical results have shown that needle length may under certain circumstances have an effect on cone-jet behavior.

Initial studies for the onset of ion evaporation have shown some of the expected behaviors. Including, increasing ion evaporation current density with diminishing flow rate. However, our initial results have not been able to reproduce the ion current vs flow rate behavior seen experimentally.

1.4 Organization

This thesis starts in chapter 2 with a brief summary of the history of colloid thruster development and of numerical simulations of free jets. Chapter 3 is a short sketch of the basic physics and basic electrospray scaling laws. Chapter 4 develops and presents the numerical model for the simulation while chapter 5 deals with the numerical schemes used to solve the system of equations. Chapters 6 and 7 present the results of our simulations along with comparisons of our simulations to experimental data. Finally, we address some final thoughts, recommendations, and ideas for future work in chapter 8.

Chapter 2

Colloid thruster technology background

In this chapter a short introduction to previous research on colloid thrusters is presented. The chapter is broadly divided in two major areas: the first refers to general history of colloid thrusters whereas the latter part of the chapter emphasizes the history of the numerical simulation of free jets, both charged and uncharged. This review is by no means complete, but it is hoped that it will help to set the context for this thesis. Where appropriate, references will be given for books, and review papers that treat each subtopic in more detail.

2.1 History of colloid thruster development

2.1.1 Colloid thruster technology- 1960's

Pioneering work by Zeleny showed that a stable single cone spray could be obtained from a liquid issuing from a thin tube [65]. The existence of this stable operating mode, however, occurred only under certain flow and voltage conditions. It was only until 1964, that the cone structure was theoretically explained by G.I. Taylor [62]. Taylor found that for a perfectly conducting liquid a conical equipotential surface was formed. The surface was the result of a balance between electrical and surface tension stresses at its surface. His analytical model predicted that the cone semi–angle would be 49.3^o which he then confirmed experimentally. Nonetheless, his studies were not able to explain the formation and the physics of the thin

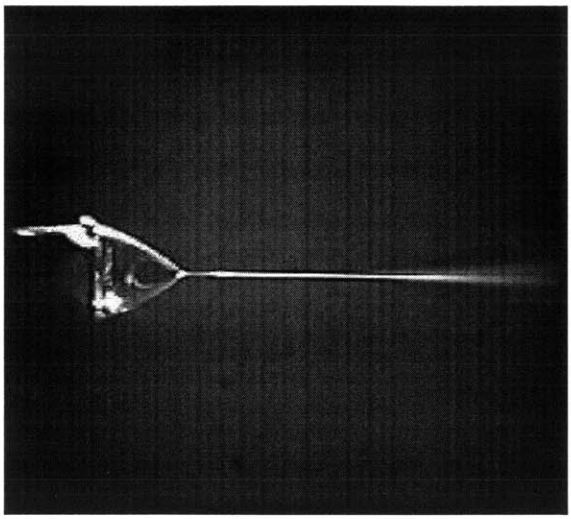

Figure 2-1: Colloid thruster operating in the single cone-jet mode. Notice the cone transition section, breakup and plume, Courtesy P. Lozano, [47]

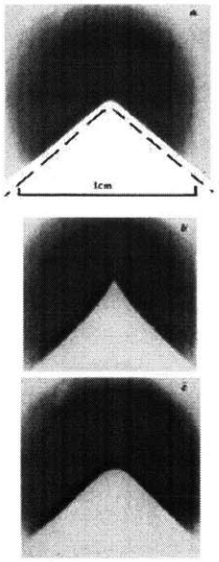

Figure 2-2: Three successive frames (in intervals of 1/64 s) showing a drop of water (which appears bright) forming a Taylor cone surrounded by oil. The first frame shows a comparison with the theoretical prediction of the cone angle; the other frames show the drop in two phases of its oscillation around this cone (Taylor, [62]).

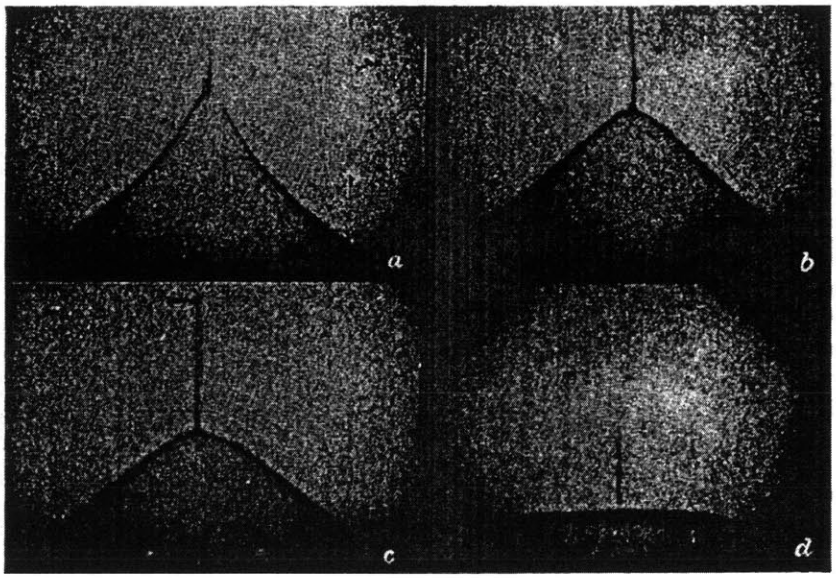

Figure 2-3: "Soap film, microsecond exposures of successive stages (a) of jet formation, (b),(c),(d) subsequent collapse." Reproduced from G. I. Taylor, [62]

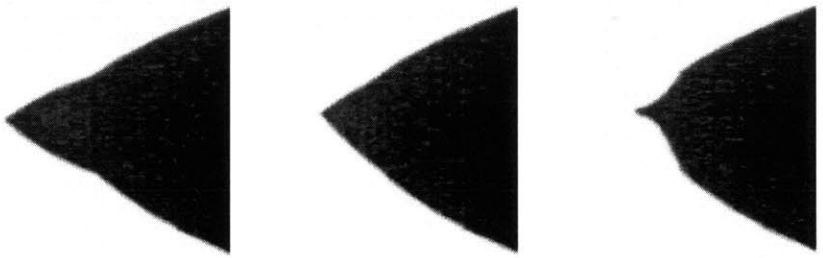

Figure 2-4: Taylor cones under various operating conditions. Liquid : Ethylene–Glycol, conductivity $K = 0.07$ Si/m. Courtesy Mangoubi and Lozano [50]

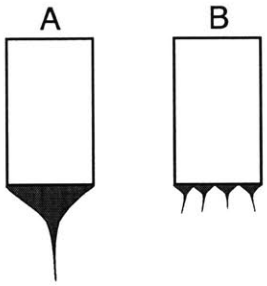

Figure 2-5: A) single cone-jet regime. B) Highly stressed regime (seen at higher voltages than the single cone-jet regime)

jet which emerged from the cone apex. Numerous semi–empirical models tried to explain the jet physics but the results were often contradictory.

Contemporary to Taylor other groups worked on developing colloid thrusters for propulsion purposes. Krohn and coworkers started experimenting with Liquid Metal Ion Sources (LMIS) and organic liquids in a variety of configurations aiming to identify suitable configurations of electrodes and liquids for propulsion purposes [40]. Work by Cohen , Shelton and others at TRW incorporated for the first time Time–of–Flight (TOF) techniques to the analysis of colloidal thruster plumes [39, 8]. At this time much of their work focused in achieving the highly stressed regime (multiple cone-jets per emitter) as opposed to the more amenable single-cone-jet regime (see Figures 2-1, 2-3, and 2-4, 2-5). At the time, colloid thrusters were envisioned for main on–board propulsion purposes requiring a relatively high thrust density and therefore high operating voltages (order of KV). Their inability to compete with Kaufmann ion engines, which had the required performance at lower voltages, and the general downturn of the space program after the Apollo era contributed to their disappearance. Research in colloid thrusters after the 1970's is almost nonexistent.

2.1.2 Colloid thruster- 1990's- present day

In 1989 the discovery by Fenn *et al* that large organic molecular ions could be extracted intact from an electrostatic electrospray revolutionized mass spectrometry [12]. Up to that point mass spectrometry had been limited to materials which could be introduced as a vapor in a gas without decomposing in the ionization process. The renewed interest in electrospray technology spurred research in the area and rekindled its propulsion application.

In 1994, basic scalings for the pure droplet regime, were published by Fernández de la Mora and Loscertales. Their work gave simple non–dimensional scalings for current vs flow rate and liquid properties [13]. Alternative scalings for the current *(I)* and droplet size were obtained by Gañan-Calvo (1997), [15, 17]. The results from Gañán-Calvo's model suggested that the polarity of the liquid (i.e. relative permittivity) played no role in determining the current and droplet size of the electrospray. Many studies of the cone, transition, and jet region have been carried out by several authors such as (Gañán-Calvo[16], Cherney[6], Higuera[28]) resulting in estimates of the variables as function of liquid properties and operational parameters. However, the complexity of the phenomenon is far from completely understood, and remains an active area of research.

Research in the 60's showed that electrosprays could emit both electrically charged drops and solvated ions, [8]. Three main regimes have been observed: pure droplet, mixed ion-droplet and pure ion (the latter only in the last three years). The appearance of each depends on the liquids employed and operational parameters such as flow rate and applied voltage. Experiments with a few organic liquids such as formamide ($K \sim 1Si/m$) operating at low flow rates $\eta \approx 1$ showed the existence of ions evaporating from the liquid surface. Work by Gamero and Lozano has shown that field–enhanced ion evaporation in organic liquids behaves in similar manner as that of liquid metal ion sources (LMIS), [21, 49].

Further information on the history of colloidal thruster development can be found in the thesis of Jose M. López-Urdiales, [45], a review paper by Martinez-Sánchez *et al*, [52], and the review by Grace and Marijnissen, [24]. Detailed information on mass spectrometry can be found in the book by Prókay, [58]. A comparison between organic electrosprays and LMIS is provided by Forbes, [14]

2.2 History of numerical studies of free jets

Computational fluid dynamic simulations have progressed significantly in the last few years. In many cases these simulations compare quite accurately with experimental data and in certain areas have actually displaced experimental work altogether. The numerical simulation of free surface flows, on the other hand, remains as a challenge and active research area. A brief introduction to the topic of free jets is given next.

2.2.1 Non-charged free jets

In this work we are particularly interested in free jet flows. These flows have various properties which make them difficult to model numerically including: variable flow geometry (in fact it is part of the solution and is prone to instabilities), breakup events (for free jets) as well as important topological changes [37, 36]. During the breakup event of a nanojet it is not even clear if near the breakup point continuum fluid mechanics gives a suitable description of the governing flow physics. Other studies have shown that these flows are prone to develop cusp singularities. It appears that surface tension effects present little resistance to the formation of singularities. Instead, it seems as if the coupling of the bulk fluid dynamics and the surface evolution make the whole simulation much more sensitive to noise, and numerical instabilities of which little is known.

Various approaches have been used to numerically model free jets, and here we will only present a brief description of the main types, as discussed by Eggers, [9]. Three main techniques have been used in the past to model free jets : boundary integral formulations, Navier-Stokes formulations, and one dimensional approximations (inviscid and viscous).

Boundary Integral Formulations

This formulation only evolves the surface of the fluid and is limited by the fact that it can only be applied in those cases in which the governing equations are linear (i.e. its Green's function is known), [9]. Fluid equations have linear properties for two limiting cases : inviscid irrotational flow and highly viscous flow. A nice property of this formulation is that all the information is carried by the surface and there is no need to calculate the interplay of the internal flow and surface evolution. An obvious drawback of this approach is that it will either neglect inertial or viscous forces both of which may be important.

In the case of inviscid irrotational flow, a high frequency nonlinear numerical instability (sawtooth) appears. The origin of this instability has not been identified, a study by Moore 1983 suggests that the equations themselves may not have a regular solution (independent of the numerical scheme employed), [54]. Numerical procedures such as filtering, numerical viscosity and regridding have been used to counter this instability with varying degrees of success.

In the Stokes approximation, the fluid problem is much less sensitive to perturbations

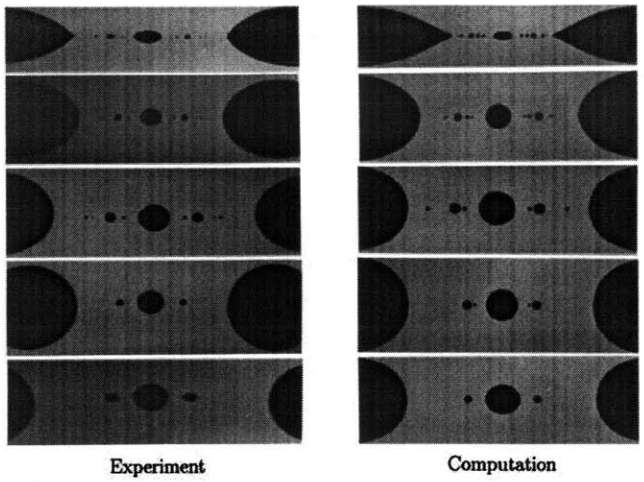

Figure 2-6: Breakup of a filament into satellite and subsatellite drops. As the viscosity ratio l is decreased, the final state of the system has an increasingly complicated fractal structure (Tjahjadi, Stone, and Ottino, [63]). The pictures are, from top to bottom, for l = 0.01, 0.067, 0.4, 1, and 2.8.

and no numerical instabilities have been reported. Stone and Leal used this approach to study drop breakup with excellent results as shown in figure 2-6, [61, 63].

Navier–Stokes formulations

In contrast to boundary integral models, the Navier-Stokes formulations track the surface evolution as well as the internal flow dynamics. The evolution of both is very complex and complicated by the fact that they are coupled. Practical concerns also arise with the movable surface which implies deformations of the computational domain. At pinch points the full Navier-Stokes equations need to be solved since at these sites both inertial and viscous effects are important. In general the major problem with Navier-Stokes formulations is that they are too complicated if analytical solutions are to be obtained. For this reason appropriate simplifications to the Navier-Stokes equations are sought. The goal of these approximations is to obtain a simplified set of equations which capture the essential nonlinear physics. One situation that is amenable to such an approximation is the case in which the liquid jet becomes long and thin. These approximations are treated next.

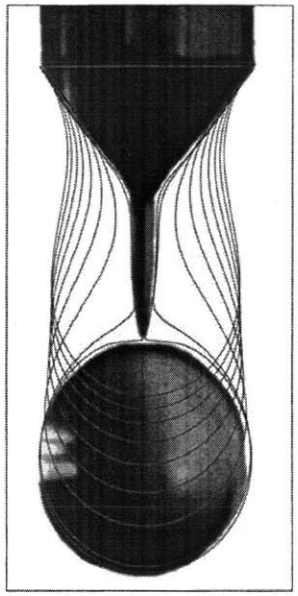

Figure 2-7: Comparison of experimental and numerical solutions with the lubrication equations of Eggers and Dupont, [10]. The lines represent the profile at various time distances and at the time of pinchoff.

Quasi-one dimensional approximations of N-S

These approximations were originally inspired by shallow water wave studies by Peregrine,[56]. Lee studied the inviscid nonlinear liquid jet dynamics which presented spurious singularities which in turn may have affected the pinching process, and contaminated the results, [42]. In 1976 Green studied the viscous form, using for this the so called Cosserat equations. These equations can be obtained by appropriate averaging over slices of the fluid, [25]. A systematic derivation of these equations from the full Navier–Stokes equations was first presented by Dupont in 1993, [10]. Next we reproduce their basic formulation, since our numerical model will be based on a similar approach. Eggers and Dupont started from the axisymmetric Navier–Stokes equations in cylindrical coordinates. Considering that the study will focus on thin columns of liquid the velocities in the radial and axial direction are represented with a Taylor series expansion with respect to the radius, r and complemented by a radial velocity which satisfies conservation of mass:

$$v\,|_z\,(z,r) = v_0 + v_2 r^2 + \ldots \tag{2.1}$$

$$v\,|_r\,(z,r) = -\frac{1}{2}v_0' r - \frac{1}{4}v_2' r^2 - \ldots \tag{2.2}$$

$$\tag{2.3}$$

Note that the primes denote derivatives with respect to axial direction z. The pressure is expressed in the same fashion:

$$p(z,r) = p_0 + p_2 r^2 + \ldots \tag{2.4}$$

Using these expansions the Navier–Stokes equations are solved to the lowest order in r. The resulting simplified equations are:

$$\frac{\partial h}{\partial t} = -v\frac{\partial h}{\partial z} - \frac{1}{2}h\frac{\partial v}{\partial z} \tag{2.5}$$

$$p = \gamma\left\{\frac{1}{h\,(1+h_z^2)^{1/2}} - \frac{h_{zz}}{(1+h_z^2)^{3/2}}\right\} \tag{2.6}$$

$$\frac{\partial v}{\partial t} = -v\frac{\partial v}{\partial z} - \frac{\partial p}{\partial z} + \frac{3\nu}{h^2}(h^2 v_z)_z \tag{2.7}$$

where $r = h$ at the liquid surface, and the subscript 0 has been dropped. The boundary conditions for this system are given by:

$$h(L\pm,t) = h\pm \tag{2.8}$$

$$v(L\pm,t) = v\pm\cdot \tag{2.9}$$

The properties of these quasi–one–dimensional equations are that near the breakup (asymptotic limit) they approximate the correct behavior and have also been used successfully away from it by Brenner *et al*, [1]. The total energy of the system only decreases and in the case of equilibrium surfaces they reproduce the behavior of the full Navier–Stokes equations, corresponding to the minimum potential energy. A secondary benefit comes from the stability arena, in which it is shown that short wavelength perturbations will not grow

and the dispersion behavior obtained reproduces that of the full Navier–Stokes, [1]. The results obtained with this model gave results that compared very well to experiments, see figure 2-7.

A thorough review of uncharged free jets is given by Eggers (an important part of this section is based on that work) including history, experimental, analytical and numerical work, [9].

2.2.2 Charged free jet simulations

Numerical modeling of electrospray phenomena has been an active area of research for many years. Many models have been developed, some dedicated to LMIS, some for liquid menisci, and some others meant to study the cone–jet transition and its the downstream plume.

In recent years several numerically based models have been presented to simulate the cone-jet transition region. The numerical work in this area may be traced back to the model of Eggers and Dupont [10], and Brenner *et al* [1], for gravity and pressure driven fluid jets. The success of these and subsequent models suggested that a similar approach could be used for electrified jets. On electrified jets several models have been presented such as the static model of Pantano *et al* [55], the hybrid model of Gañán-Calvo [16], and the asymptotic model for the low flow rate limit of [6]. As of this writing several numerical models have been published such as the works of Hohman *et al* [32], Hartman *et al* [27], Yan [64], and Feng [11].

In 1994, Pantano and coworkers developed a zero flow limit simulation of the electrospray problem [55]. Pantano constructed an axisymmetric model which included: the needle and extractor as well as a perfectly conducting liquid menisci. In this case the goal was to predict the shape of the menisci for different voltage settings. The results obtained, he reasoned, could be used as a leading order term in a perturbation scheme of the electrospray problem. A later study by Gañán-Calvo (1998) employed a hybrid experimental-numerical technique to calculate the surface charge of jets as well as other parameters, [16]. He experimentally obtained a digital representation of the jet section which was then fitted using a hyperbolic regression (8th order) thus obtaining the jet shape in close analytical form. The jet shape was then fed to a quasi-one dimensional flow model from which the surface charge characteristics were calculated. This information along with measured current for each case allowed him to develop scaling relations for the emitted current (Eq. 3.47), droplet diameter

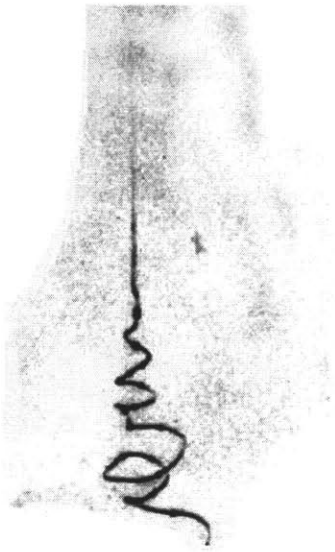

Figure 2-8: Strobe photograph of the overall picture of an unstable jet. The shutter speed is 3 μs. On large scales, it appears as a whipping rope, with blob-like varicose protrusions. From Hohman *et al* FIG. 11., [32]

(Eq. 3.26) and surface charge density.

In 1999, Hartman *et al* developed the first simulation of a full cone-jet, [27].The model used by Hartman assumed a plug flow profile for the liquid. Hartman's work obtained results for Ethylene glycol, n-Butanol, methanol and heptane. The highest conductivities were in the order of $K = 0.2\ mSi/m$.

Hohman *et al* developed a simulation to predict the behavior of electrospun polymer fibers, [32]. These fibers are made by forcing a polymeric fluid through a needle under the action of an applied electric field. The electrospinning phenomenon is similar to that of electrospraying, and Hohman's work built on previous electrospray studies. In this case Hohman's model is basically an extension of the model of Brenner *et al* for uncharged jets. Hohman *et al* compared their results to experimental data and noticed that the electrode setup had an important effect on their results. Significant improvement of their results were obtained when the effect of fringe fields at the liquid-needle interface was added to their simplified electrostatic model. This work concluded that the whipping jet instability (see figure 2-8) results from an interaction of the surface charge of the jet and the externally applied E-field. This whipping instability suppresses the varicose instability (of typical free

jets) allowing the formation of long thin fibers.

The third work to appear in this area is that of Yan et al. This work followed on the steps of that of Hartman et al. The major difference is that Yan introduced a parabolic velocity profile in his formulation as opposed to a plug flow profile used by Hartman. This group's work reproduced the experimental data of Hartman *et al*, [27].

In 2001 Feng presented a new simulation for electrospun fibers,[11]. This work only concentrated on the initial thinning of the fiber due to the electric stretching without actually simulating the whipping instability. Feng's work built on the previous efforts of Hohman *et al* contributing a more accurate representation for the electrostatic fields, and a careful comparison for non-Newtonian and Newtonian jet behavior. The important contributions of Feng from the electrospray perspective are: A) was able to explain and clarify the ballooning instability seen by Hohman's electrostatic model and B) performed a series of parametric studies of the surface charge density boundary condition. For this condition he concluded that it was only relevant within a small region (boundary layer like behavior) still far from the cone-jet transition zone,(see section 4.6).

One of the more recent papers on the numerical simulation of colloid thrusters is that of Higuera, [28]. In this work Higuera simulates the cone-jet transition section of the free jet. He uses asymptotic approximations both upstream (instead of actually simulating the needle-exit condition) and downstream (no jet breakup, infinitely thinning condition) of the transition as his boundary conditions. His results reproduce the basic current scalings of Fernández de la Mora and Loscertales as well as those of Ganan-Calvo, [13, 15]. Higuera includes a very rich discussion on the detailed scaling of various flow variables: surface charge, jet radius, E-fields, etc.

A good review paper on the leaky dielectric paper used for describing charged free jets is that by Saville, [59].

2.2.3 Mixed ion-drop regime simulations

Original research on ion emission came about from studies of the physics of charged drop generation and evaporation. Research on ion emission from liquids dates back to the mobility measurements of Chapman, [3]. In his experiments he generated (by spraying and bubbling) charged droplets of aqueous solutions with various concentrations of dissolved salts. His results led him to suggest that the electrically charged drops were singly charged,

[3]. Further work by Iribarne and Thompson [33] confirmed that the high mobility carriers seen evaporating from water droplets were singly charged clusters. Their experiments also showed that depending on the drop size ions separated by evaporation or by Rayleigh's instability (Coulombic explosion for drops). Iribarne and Thompson proposed a theoretical model for the field enhanced ion evaporation based on absolute reaction theory and included estimates of the solvation energy of the extracted clusters. This model theorized that the potential attracting the escaping ion was due to polarization of the droplet by the ion.

The group of Fenn and coworkers [12] realized that using an electrospray it was possible to generate electrically charged droplets of complex organic molecules. These drops were then passed through a drying chamber which further reduced their size increasing its electrical field which led to the desorption of solvated ions or Coulombic explosions. The resulting quasi-particles would then enter a mass spectrometer for analysis. This novel technique allows the analysis of proteins and other delicate polar molecules without destroying them, effectively revolutionizing the mass spectrometry field.

Work by Loscertales and Fernández de la Mora [46], confirmed that the mechanism for ion extraction is field evaporation. They proposed a new extraction model based on image potential theory (effectively a Schottky type model) and compared it to experimental data with good success. Loscertales and Fernández de la Mora also obtained estimates for the drop field intensities required for field evaporation which range between ($E \approx 1 - 2V/nm.$)

Further work on electrosprays with high conductivity ($K \approx 1Si/m$) and low flow rates showed that an important fraction of the collected current came from ions. Detailed experimental research in this topic by Gamero-Castaño, Fernández de la Mora, Lozano and Martinez-Sánchez showed that solvated ions could be emitted from the cone–jet transition region, the jet breakup region and the inflight droplets, [20, 21, 48, 49, 47]

Very little numerical work has been done on the mixed ion-droplet regime, and onset of ion evaporation. The subject is much more developed for liquid metal ion sources (LMIS) where the currently is only ionic (plus occasional droplets). For a more detailed discussion on the LMIS subject see [57]. For organic liquids, the work of Higuera is one of the most recent, [29]. In this work Higuera extends the basic cone-jet simulation of his previous electrospray paper ([28]) to the onset of ion evaporation. Higuera based his ion evaporation model on a Schottky type model (thermionic emission), but due to the numerical difficulty of the problem had to artificially reduce some of the parameters (see ch. 7). The results obtained

with these artificially low parameters, however, reproduced qualitatively the behaviors seen experimentally by Fernández de la Mora. The theory of ion desorption is treated in depth in the paper of Gomer, [23] and the previously referred to Prókay book, [58] .

2.3 Summary

In this chapter a brief overview of the history of research on colloid thrusters has been provided with emphasis on the theoretical modeling work. Starting from the pioneering work of Zeleny at the turn of the century to the most recent developments in the field. In the next chapter, the basic physics of electrosprays will be presented.

Chapter 3

Physics

3.1 Taylor cone

It is well known that when a liquid drop is subjected to a sufficiently high electric potential its surface experiences an electrostatic pull which if strong enough will deform the surface of the liquid. The surface deformation, is triggered by small perturbations of the surface (ambient vibration), which in turn enhance the local electric field (through charge concentration), further increasing the electrostatic pull in a cascading effect, [51]. If the applied potential is high enough the surface deformation will start to resemble a liquid cone (see figure 3-1). A limiting case is reached when the apex of the cone approaches a point, i.e. a singularity. It is at this point that a high speed thin jet is observed to emanate from the apex of the cone, see figure 3-2.

The first explanation of this phenomenon was offered by G. I. Taylor, who in 1964 Obtained the first analytical model for the cone structure. He constructed a model of a perfectly conducting liquid cone at equilibrium (with no jet from the apex) for a given

Figure 3-1: Ethylene Glycol Liquid menisci. Left meniscus V=0 V, right meniscus $V = 2.5KV$ with superposed spherical coordinate system, photos courtesy Paulo Lozano, MIT

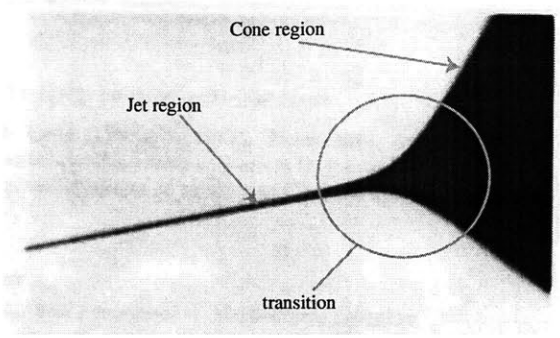

Figure 3-2: Structure of the cone jet for Ethylene-Glycol, $\eta = 2$, Re=10.2, courtesy of Fernández de la Mora and Loscertales [13]

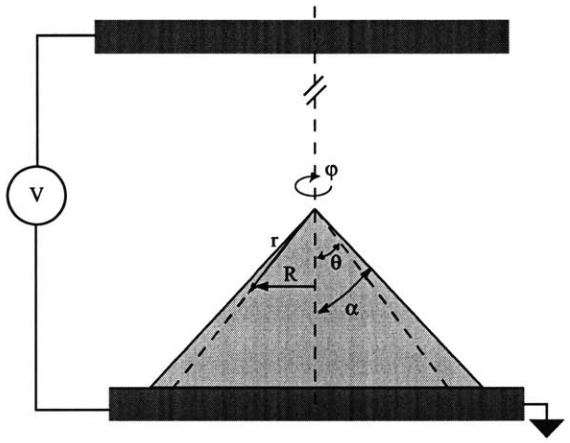

Figure 3-3: Conical coordinate system

applied potential, V_{st}. Taylor hypothesized, that the conical shape resulted from a perfect equilibrium of two opposing forces: the liquid's surface tension and the electrostatic stress on the liquid's surface. The surface tension force per unit area can be described as

$$f_{st} = \gamma \left(\frac{1}{R_1} + \frac{1}{R_2} \right) \tag{3.1}$$

where γ is the surface tension coefficient for a given liquid and R_1 and R_2 are the principal surface radii of curvature. For a cone the curvature of the normal section is $R_1 = \cot\theta / r$ while the second curvature tends to zero ($R_2 \to \infty$) leading to

$$f_{st} = \gamma \left(\frac{\cot \theta}{r} \right) \tag{3.2}$$

The electrostatic stress for a liquid is described by the classical equilibrium model put forth by Landau and Lifshitz [41]. We apply this thermodynamic model to our problem even though it is clearly out of equilibrium. A better option would be based on liquid kinetic theory, however, it is poorly developed and therefore the thermodynamic based model is preferred. The electrostatic stress tensor is given by :

$$\overline{\overline{T}}_E = \epsilon\epsilon_0 \vec{E}\vec{E} - \frac{1}{2}\epsilon\epsilon_0 \left[1 - \frac{\rho}{\epsilon} \left(\frac{\partial \epsilon}{\partial \rho} \right)_T \right] (\vec{E} \cdot \vec{E}) \overline{\overline{\delta}} \tag{3.3}$$

where ϵ is the liquid relative permittivity, ϵ_0 is the free space permittivity, $\vec{E}$ is the electrical field, and $\overline{\overline{\delta}}$ is Kronecker's delta. For the normal and tangential directions the electrical stress components are obtained by subtracting the outer and inner stresses and neglecting the $(d\epsilon/d\rho)$ contribution leading to:

$$\|\hat{n} \cdot \overline{\overline{T_E}} \cdot \hat{n}\| = \frac{\epsilon_0}{2} \left[(E_n^o)^2 - \epsilon (E_n^i)^2 + (\epsilon - 1) E_t^2 \right] \tag{3.4}$$

$$\|\hat{n} \cdot \overline{\overline{T_E}} \cdot \hat{t}\| = \epsilon_0 E_t (E_n^o - \epsilon E_n^i) = \sigma E_t \tag{3.5}$$

where E_n^o is the normal external electric field, E_t is the tangential field and E_n^i is the normal internal field. The last two are zero for a perfectly conducting liquid, simplifying the expression to:

$$f_{ne} = \|\hat{n} \cdot T^E \cdot \hat{n}\| = \frac{\epsilon_0}{2} \left[(E_n^o)^2 \right] \tag{3.6}$$

$$f_{te} = \|\hat{n} \cdot T^E \cdot \hat{t}\| = 0 \tag{3.7}$$

Equating the normal electrostatic stress to the surface tension force per unit area leads to

$$\frac{\gamma \cot \alpha}{r} = \frac{1}{2} \epsilon_0 E_n^2 \tag{3.8}$$

Inherent in this force balance is the assumption that the internal pressure of the liquid

is zero.

For a perfectly conducting material (in this case liquid) the surface is an equipotential, and the field is described by Laplace's equation, $\nabla^2\phi = 0$. Laplace's equation for the conical section (with symmetry about φ) is:

$$\nabla^2\phi \equiv \frac{1}{r^2}\frac{\partial}{\partial r}\left(r^2\frac{\partial\phi}{\partial r}\right) + \frac{1}{r^2\sin\theta}\frac{\partial}{\partial\theta}\left(\sin\theta\frac{\partial\phi}{\partial\theta}\right) \tag{3.9}$$

with θ measured from the inside the conical section. This problem has known solutions in terms of Legendre polynomials given by :

$$\phi = A\mathbf{P}_\upsilon(\cos\theta)r^\upsilon \tag{3.10}$$

$$\phi = A\mathbf{Q}_\upsilon(\cos\theta)r^\upsilon \tag{3.11}$$

Another possible solution is $1/r^{\upsilon+1}$ instead of r^υ but it diverges too fast as $r \to 0$. The Legendre polynomials present singularities at $\theta = 180°$ for the $\mathbf{P}_\upsilon$ and at $\theta = 0°$ for $\mathbf{Q}_\upsilon$. In this case we choose the $\mathbf{Q}_\upsilon$ family of solutions since the singularity is then inside the cone. The parameter υ still needs to be determined, this is done by calculating the normal field from the potential solution

$$E_n = -\frac{1}{r}\frac{\partial\phi}{\partial\theta} = A\frac{d\mathbf{Q}_\upsilon}{d(\cos\theta)}\sin\theta\frac{1}{r^{1-\upsilon}} \tag{3.12}$$

The key here is to notice that in order for the normal E-field to equilibrate the surface tension effect the exponent has to be $\upsilon = 1/2$. The complete solution is then:

$$\phi = A\mathbf{Q}_{1/2}(\cos\theta)r^{1/2} \tag{3.13}$$

The solution shows that the potential ϕ will vary with r. In order to satisfy the equipotential condition at the liquid surface the potential has to be independent of r. This condition is met if $\mathbf{Q}_{1/2}(\cos\theta) = 0$, in other words the root of the Legendre function. The condition is met for $\theta = 49.29°$ thus predicting the semiangle of the perfectly conducting cone. Notice that this angle is independent of the applied potential, and liquid properties. Taylor's prediction has been experimentally corroborated,[62]. The constant A is solved for

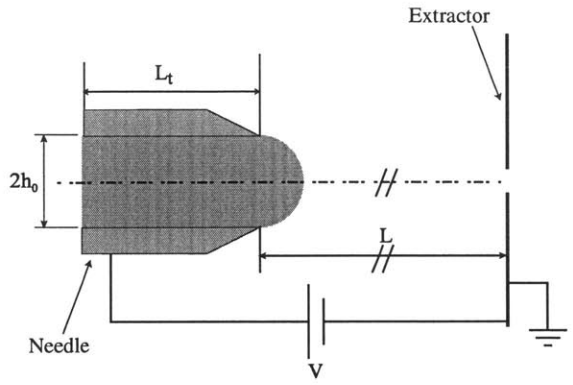

Figure 3-4: Meniscus and capillary arrangement. L is distance between needle and collector, L_t is the needle length, and h_0 is the inner radius of the conducting needle.

by substituting expression 3.12 into 3.8 for $\theta = \alpha_T = 49.29°$

$$A = \left(\frac{2\gamma \cot \alpha_T}{\epsilon_0}\right) \frac{1}{\mathbf{Q}'_{1/2}(\cos \alpha_T)}. \tag{3.14}$$

The Taylor cone and its angle (α_T) are however not an exact representation of what happens with any liquid when nonzero current is flowing, since liquids have finite conductivities, and near enough the tip the potential cannot remain constant. Another issue to consider is that under Taylor's model the potential difference is set between two equipotentials, that of the liquid cone and that of the external electrode, the shape of which is that of one of the iso-lines of $r^{1/2}Q_{1/2}(\cos\theta)$. In experiments, the actual electrode setup may not replicate the geometry of Taylor's model. Another important effect is the absence of the charged jet in Taylor's model. The charged jet will modify the potential distribution of the conical section leading to deviations from Taylor's angle. Given these observations, it is conceded that the Taylor model was and is a very important step in understanding the behavior of liquid cone-jets, and is in fact quantitatively correct in a wide intermediate range of r, between the vicinity of the jet and some distance from the cone's base.

3.2 Starting potential

In the preceding section reference was made to the critical applied potential. This potential if reached would result in the Taylor cone (actually it overshoots the Taylor cone by about

10 %, since it takes more field to overcome a spherical than conical meniscus), and in practice it is an approximation to the minimum potential needed to develop a jet from the cone's apex. From a practical standpoint it is useful to make an estimate of this critical potential. The starting voltage is calculated based on an estimate of the normal electric field of an equipotential surface with a round tip (described by a confocal hyperboloid in prolate spheroidal coordinates) with respect to a ground plane (symmetry plane of said coordinate system). For a liquid meniscus formed at the exit of a conducting needle with inner radius h_0 we can assume that the radius of curvature R_c will be of the same order as h_0:

$$V = \sqrt{\frac{\gamma h_0}{\epsilon_0}} \ln\left(\frac{4L}{h_0}\right). \tag{3.15}$$

where γ is the liquid's surface tension coefficient, and L is the distance between the exit of the needle and the ground collector, see figure 3-4. This formula only gives an approximation to the required starting voltage(experimentally verified within 10%) for each simulation but thus providing a reasonable starting point for the simulation, [51].

3.3 Cone-jet physics

Once the emission condition for the electrostatically accelerated jet is reached, a number of new parameters arise. The most important ones are flow rate and collected current. Significant previous research has been done to better understand the physics of jet formation, jet radius, emitted current, etc., and how they relate to liquid properties and operating parameters. In what follows we include a summary of the basic scalings for these jets.

3.3.1 Cone-jet transition length scales

The basic physics of colloidal thrusters has been addressed in numerous experimental and theoretical papers. These papers have successfully yielded basic scaling laws for the cone and jet regions as seen in the works of Fernández de la Mora & Loscertales [13], Gañán-Calvo [15, 19, 16, 18, 17], Hohman *et al*[32], Cherney [6], Higuera [28], and Clopeau *et al* [7] to name a few.

The basic model and scalings of Fernández de la Mora & Loscertales [13] will be quickly reviewed as background for later discussion. Two basic assumptions are at its root: (a) The

static Taylor equilibrium is maintained to the point where the flow time becomes shorter than the electrical relaxation time; beyond this, the cone transitions quickly to a jet, (b) At the same point, the current, which in the cone was carried by the bulk conduction (conduction current, I_{cd}) transitions rapidly to surface free charge convection by the accelerating liquid stream, (convection current, I_{cv}). Assumption (a) yields a characteristic distance r^* from the apex where flow time is of the order of the electrical relaxation time :

$$\frac{\epsilon\epsilon_0}{K} = \frac{r^{*3}}{Q} \tag{3.16}$$

where Q is the flow rate, and K the liquid conductivity. Inertia has been conspicuously absent from this discussion. Yet, a non-dimensional factor $\eta^2 = inertia/capillarity$ at the neck was found empirically to play an important role, in that the minimum flow rate for stable cone-jet structure was found to be given roughly by $\eta = 1$. In more detail,

$$\eta^2 = \frac{\rho Q^2}{\gamma r^3} \tag{3.17}$$

and for $r = r^*$, using 3.16,

$$\eta^2 = \frac{\rho K Q}{\gamma \epsilon \epsilon_0} \tag{3.18}$$

The final aspect of the Fernández de la Mora model that we want to mention here is that it predicts a jet initial radius of the order of r^*, however, Fernández de la Mora concedes that under $\eta > 1$ conditions inertia may play a role in the transition. For this reason an alternate length scale is defined. As the liquid flows towards the cone apex with a local radius h and average velocity u, the dynamic pressure $\rho u^2 \approx \rho Q^2/h^4$ at some point becomes comparable to the capillary pressure $\sim \gamma/h$. This cross-over occurs at a characteristic radius

$$R_d = \left(\frac{\rho Q^2}{\gamma}\right)^{1/3} \tag{3.19}$$

and then $\rho u^2 > \gamma/h$ at smaller radii. In reality because Bernoulli's equation applies, from zero pressure far upstream,

$$p + \frac{1}{2}\rho u^2 \approx 0 \tag{3.20}$$

so the significance of the "dynamic pressure" is a liquid bulk tension (negative pressure). At $h < R_d$, this bulk tension replaces capillarity as the force resisting the electrostatic surface traction. However, the liquid dynamics under these conditions may be unstable with respect to shape oscillations. A theory of this instability is lacking, but a simple argument will make it plausible: if the flow is temporarily restricted (by pinching of the cone's surface, for instance) the velocity will decrease and by Bernoulli's equation, the pressure will increase (become less negative). At the same time, the electrostatic surface traction may actually increase, if the deformation responsible for the pressure increase also creates convexity. The combined effect is to accelerate the fluid outwards strongly, both dominant forces cooperating.

This (admittedly sketchy) argument leads us to postulate that, under conditions of $\eta > 1$ the jet may actually form at $h \approx R_d$ rather than at $r = r^*$. The direct numerical evidence for this distinction is not clear enough, since our results cluster close to $\eta = 1$, where both distances are equal since they relate by

$$\eta^{2/3} = \frac{R_d}{r*}. \tag{3.21}$$

A third length scale R_g has been proposed by Gañán–Calvo [15, 17]. This length scale can be derived from a simplified set of electrospray equations (valid near the transition region), as given by Gañán-Calvo [16]:

$$\epsilon_0 E_n^2 \approx \frac{\rho Q^2}{R_o^4} \tag{3.22}$$

$$\frac{\rho Q^2}{R_o^4 L_o} \approx \frac{\epsilon_0 E_n E_t}{R_o} \tag{3.23}$$

$$\frac{\epsilon_0 Q E_n}{R_o} \approx R_o^2 K E_t \tag{3.24}$$

$$E_t \approx \left(\frac{\gamma}{\epsilon_0 L_o}\right)^{1/2} \tag{3.25}$$

Eq. 3.22 establishes that the pressure depression (related to dynamic pressure) at the transition is balanced by the electrostatic pull. Eq. 3.23 approximates the axial momentum equation where the dominant terms are the nonlinear convective term and the electrostatic acceleration term. Near the transition the convection and conduction current become equal,

Eq. 3.24 . Finally, Eq. 3.25 approximates the tangential electric field near the transition arguing that its behavior is dominated by the cone contribution. These four equations comprise a closed system for which we can solve for $R_o \equiv R_g$ resulting in:

$$R_g = \frac{1}{\pi^{2/3}} \left(\frac{\rho \epsilon_0}{\gamma K} \right)^{1/6} Q^{1/2} = \frac{1}{\pi^{2/3}} \left(\frac{r^* R_d}{\epsilon^{1/3}} \right)^{1/2} \tag{3.26}$$

which can also be expressed in terms of r^* and R_d. In subsection 6.2.4 we will address again the transition length scale issue and see how r^*, R_d, and R_g compare to numerically obtained results.

The scaling analysis by Gañán-Calvo also obtains two non-dimensional parameters (in his notation, [17]):

$$\alpha_\rho = \frac{\rho K Q}{\gamma \epsilon_0} = \epsilon \eta^2 \tag{3.27}$$

$$\alpha_\mu = \frac{K^2 \mu^3 Q}{\epsilon_0^2 \gamma^3} = \frac{\epsilon^2 \eta^2}{\Pi_\mu^3} \tag{3.28}$$

$$\tag{3.29}$$

α_ρ and α_μ which have the same function as η. In other words both α's define non-dimensional flow rates (Q/Q_{scale}). The difference resides in the reference (or scaling) flow rate, Q_{scale}. For α_ρ the reference is derived from equations (3.22-3.25) and is given by:

$$Q_{scale} = \frac{\gamma \epsilon_0}{\rho K}. \tag{3.30}$$

The second group α_μ describes a different flow behavior than that given by equations (3.22-3.25). In this case equations 3.22 and 3.23 are substituted by:

$$\frac{\mu Q}{R_o^3} \approx \frac{\gamma}{R_o} \tag{3.31}$$

$$\frac{\mu Q}{R_o^3 L_o} \approx \frac{\epsilon_0 E_n E_t}{R_o} \tag{3.32}$$

respectively. This means that for highly viscous fluids (where viscous effects dominate over inertia) the viscous stress will dominate over the electrostatic pull near the transition region. Solving for Q in this new set of equations results in:

$$Q_{scale} = \frac{\gamma^3 \epsilon_0^2}{\mu^3 K^2} \tag{3.33}$$

which in turn defines $\alpha_\mu = Q/Q_{scale}$ of equation 3.28. The range over which these non-dimensional flow rate scalings are valid is discussed in detail in section 3.3.3

3.3.2 Viscous effects

Previous studies have addressed the importance of viscous effects on cone-jet electrohydrodynamics such as Fernández de la Mora and Loscertales [13], Gañán–Calvo *et al* [18, 17], and Cherney [6]. Fernández de la Mora and Loscertales define the Reynolds number in terms of r^*:

$$Re^* = \frac{Q}{\nu r^*} = \Pi_\mu \eta^{4/3} \tag{3.34}$$

where ν is the kinematic viscosity, and the nondimensional group Π_μ is:

$$\Pi_\mu = \left(\frac{\gamma^2 \rho \epsilon \epsilon_0}{K \mu^3} \right)^{1/3} \tag{3.35}$$

which only depends on the liquid properties and serves as an approximate measure of the ratio of inertial to viscous forces (since $\eta \approx \mathrm{O}(1)$) for a given liquid.

Scaling arguments by Fernández de la Mora and Loscertales argue that viscous effects become negligible when the non-dimensional viscous parameter $Zf(\epsilon)/\epsilon$ is small:

$$Z = \Pi_\mu \eta^{-2/3} = \frac{Re^*}{\eta^2} \tag{3.36}$$

$$Z \frac{f(\epsilon)}{\epsilon} \ll 1 \tag{3.37}$$

where Z(equation 17c, [13]), is a measure of the radial variations in the axial velocity and $f(\epsilon)$ is an experimentally obtained parameter of order 20,(equation 18a, [13]). Viscous effects tend to make the velocity profile flat while electrical traction shows the opposite effect.

Gañán-Calvo defines a Reynolds number based on his two non-dimensional groups (Eq. 3.27, 3.28):

$$Re_g = \left(\frac{\alpha_\rho}{\alpha_\mu^{1/4}} \right)^{4/3}. \tag{3.38}$$

which can be rewritten in its classical form:

$$Re_g = \left(\frac{\rho K^2}{\gamma \epsilon_0^2} \right)^{1/3} \frac{Q}{\nu} \tag{3.39}$$

where the length scale is R_g evaluated with $Q = \gamma\epsilon_0/(\rho K)$ from 3.22- 3.25.

The importance of viscosity is most readily seen by using the scaling parameters of Gañán–Calvo where viscosity dominates over inertia ($Re_g \ll 1$) for $\alpha_\rho < \alpha_\mu^{1/4}$. Colloid thrusters and typical electrosprays (such as the results of Fernández de la Mora and Loscertales [13]) fall in the category of $\alpha_\rho \gg \alpha_\mu^{1/4}$ relegating viscous terms to a secondary role with little effect on the current scaling, [17]. Viscous effects do become important in other circumstances such as in the electrospinning of fibers.

3.3.3 Current scaling

(b) At the same point, the current, which in the cone was carried by the bulk conduction (conduction current, I_{cd}) transitions rapidly to surface free charge convection by the accelerating liquid stream, (convection current, I_{cv})

The second assumption of the Fernandez de la Mora and Loscertales model (see section 3.3.1) which describes the transition from a dominating bulk conduction current to a convected current near the transition region. It is this assumption which allows current to be calculated. At about the crossover from conduction (I_{cd}) to convection (I_{cv}), the convective current (which rapidly becomes all of the current) is approximated by

$$I_{cv} \approx 2\pi h u \sigma \tag{3.40}$$

where σ is the free surface charge density. In order of magnitude, $h \sim r^*$, since both transitions are assumed to be co-located. Also $u \approx Q/\pi h^2$ and since surface charge equilibrium has been maintained right up to r^*, $\sigma \approx \epsilon_0 E_n^o$, where E_n^o is as in Taylor's static equilibrium (surface tension balancing electric traction) :

$$E_n^o = \sqrt{\frac{2\gamma \cot \alpha}{\epsilon_0 r^*}}. \tag{3.41}$$

combining and ignoring numerical factors,

$$I \approx \frac{Q\sqrt{\epsilon_0 \gamma}}{r^{*3/2}} \tag{3.42}$$

and using equation 3.16:

$$I \sim \sqrt{\frac{\gamma K Q}{\epsilon}}. \tag{3.43}$$

The factor of proportionality, f was argued to depend at most on the dielectric constant ϵ, though the details of the finite- width transitions were ignored. In all,

$$I = \frac{f(\epsilon)}{\sqrt{\epsilon}}\sqrt{\gamma K Q} \tag{3.44}$$

where $f(\epsilon) \simeq 18 - 20$ for $\epsilon > 40$, decreasing more or less linearly to zero for smaller ϵ. Because of the central role of η in selecting the flow rate (we normally want flows close to the minimum), it is worth rewriting the current expression 3.44 in terms of η

$$I = f\gamma\sqrt{\frac{\epsilon_0}{\rho}}\eta \tag{3.45}$$

which points to a convenient scale for current, namely I($\eta = 1$) :

$$I^* = I_{(\eta=1)} = f\gamma\sqrt{\frac{\epsilon_0}{\rho}} \tag{3.46}$$

A similar current scaling is proposed by Gañán–Calvo [15, 17]:

$$I_{GE} = \sqrt{\gamma K Q} \tag{3.47}$$

differing from equation 3.45 in that it has no dependence on the relative permittivity (ϵ). Gañán–Calvo, mentions that two main regimes exist for colloid thrusters. The first one, inertially-electrically dominated flows, (IE in his notation) follows the current scaling of equation 3.47. The second one is inertia-polarization dominated (IP), [17] and scales current as:

$$I_{GP} = \left(\frac{\gamma K^2 Q^2}{(\epsilon - 1)\epsilon_0}\right)^{1/2} \tag{3.48}$$

Estimate	symbol	Equation	Reynolds number range	flow rate range
F. de la Mora	I_{fdm}	3.44	$Re^* << 1$	$\eta \geq 1$
IE	I_{GE}	3.47	$\alpha_\rho >> \alpha_\mu^{1/4}$	$\frac{\alpha_\rho}{(\epsilon-1)} >> 1$
VE	I_{GE}	3.47	$\alpha_\rho << \alpha_\mu^{1/4}$	$\frac{\alpha_\mu}{(\epsilon-1)^4} >> 1$
IP	I_{GP}	3.48	$\frac{\alpha_\rho}{(\epsilon-1)} >> \frac{\alpha_\mu}{(\epsilon-1)^4}$	$\frac{\alpha_\rho}{(\epsilon-1)} << 1$

Table 3.1: Main current scalings, [13, 17]. Note that in the case of the F. de la Mora scale the current scaling holds even for $Re^* >> 1$, showing the same trends as the IE and VE current scaling.

The IE regime is the most common one and the data of Fernández de la Mora and Loscertales belongs to this group,[13] while the IP regime has been observed from López-Herrera data and according to Gañán–Calvo for the Formamide and water results of Fernández de la Mora, [43, 17]. Gañán–Calvo discusses two viscosity dominated regimes : VE which is viscosity and pressure suction dominated (originally proposed by Higuera, [28]) and is typical of highly viscous liquids and of electrospinning. In this regime the current also scales as given by equation 3.47 while the jet radius scales as [28, 17]:

$$R_{VE} = \frac{1}{2}\left(\frac{\mu\epsilon_0^2 Q^3}{\gamma K^2}\right)^{1/8}. \tag{3.49}$$

The last regime is the viscous and polarization dominated regime (VP) which has not been observed (no published data has been found to comply with this scaling), [17]. Numerical results will be compared to these scalings in chapter 6. The domains of applicability of the scalings proposed by Fernández de la Mora and Gañán–Calvo are presented on table 3.1

In this work results are reported using the Fernández de la Mora scaling where the flow rate (Q) is reported in terms of the dimensionless variable η and the current is reported in terms of the dimensionless group ζ :

$$\eta = \sqrt{\frac{\rho K Q}{\gamma\epsilon\epsilon_0}} \tag{3.50}$$

$$\zeta = \frac{I}{\gamma(\epsilon_0/\rho)^{1/2}}. \tag{3.51}$$

3.3.4 Drop characteristics

Downstream of the transition region the jet will continue thinning out and eventually when it reaches a radius (R_b) it breaks up into charged droplets. Experiments have shown that droplet radius (r_d) is approximately $r_d = 1.89R_b$, conforming to the Rayleigh-Taylor breakup prediction for un-charged jets, [51]. Theoretical upper and lower bounds for the charge to mass ratio of the primary drops are presented next. The upper bound is based on the maximum charge that a liquid drop can sustain for a given radius. Under equilibrium conditions the balance of the electrostatic pull vs surface tension for a spherical drop is:

$$E_n^o = \frac{q}{4\pi\epsilon_0 r_d^2} \tag{3.52}$$

$$\frac{1}{2}\epsilon_0 (E_n^o)^2 = \frac{2\gamma}{r_d} \tag{3.53}$$

solving for the charge (q) and dividing the resulting expression by the drops mass (m) gives:

$$\left[\frac{q}{m}\right]_{max} = \frac{6(\epsilon_0\gamma)^{1/2}}{\rho r_d^{3/2}} \tag{3.54}$$

this expression is known as the Rayleigh limit for the charge to mass ratio of a liquid droplet. The minimum bound for the charge to mass ratio is based on a thermodynamic energy minimization argument which concludes that the minimum charge to mass ratio for a droplet is half of the Rayleigh limit $q/m|_{max} = 2\ q/m|_{min}$, [51]. For a high conductivity formamide solution ($K \approx 1\ Si/m$) the highest charge per unit mass measured has been in the order of $q/m = 10,000 C/Kg$, [47].

Our work will not address the droplet formation process. which include complex interactions among viscous, electrical, inertial, and capillary effects and lead to phenomena such as satellite droplets, long fiber formation, etc. For more information on this see for instance the work of López-Herrera and Gañán–Calvo, [44].

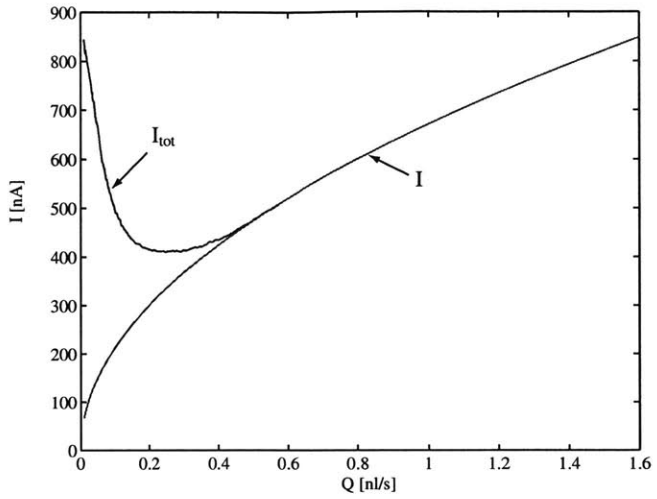

Figure 3-5: Flow rate vs current plot showing the onset of ion evaporation. I pure droplet current ($I \propto Q^{1/2}$), $I_{tot} = I + I_i$, I_i accumulated ion current. Courtesy Paulo Lozano, [47]

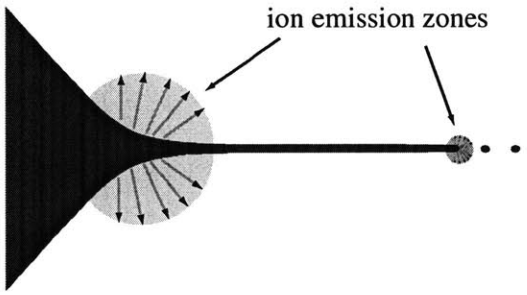

Figure 3-6: Possible electrospray ion emission zones

3.4 Mixed ion -droplet regime

Under certain operating conditions the electric field present at the surface of the electrostatically accelerated jet may be strong enough that ions begin to evaporate from it. In this section we first develop the models used to describe the field desorption of these ions. Secondly, we describe the typical characteristics of the extracted ions. Thirdly we address the effects of space-charge on the jet surface E-fields.

The onset of ion evaporation can be seen in a collected current vs flow rate plot as a departure from the $I \propto Q^{1/2}$ behavior typical of the pure droplet regime. This behavior is depicted in figure 3-5 which shows that as the flow rate decreases ion current (I_i) becomes

of the order or larger than the drop current (I) resulting in $I_{tot} > I$. In the cone-jet mode a decrease of flow rate results in a higher surface field. If the surface field reaches a threshold value before the jet instability condition ($\eta \leq 1$) is reached, ions will begin to evaporate from its surface. The condition for ions to be emitted can then be expressed in terms of $Q_{\eta=1} < Q_{E=E_{crit}}$. The maximum fields are expected in charge concentration areas, in this case the cone-jet transition and the jet breakup point. It is these zones that are the most likely to evaporate ions, see figure 3-6. A maximum field estimate for the cone-jet transition region is given by,[21]:

$$E_{max} = \frac{\gamma^{1/2} K^{1/6}}{\epsilon_0^{2/3} Q^{1/6}} \tag{3.55}$$

substituting equation 3.18, E_{max} is reexpressed as:

$$E_{max} = \left(\frac{\gamma^2 \rho}{\epsilon_0^5 \epsilon}\right)^{1/6} \frac{K^{1/3}}{\eta^{1/3}} \tag{3.56}$$

for high conductivity liquids ($K \approx 1\ Si/m$) the surface field may approach 1 V/nm (the threshold field). A quick estimate (using Eq. 3.56) shows that for a formamide solution ($\eta = 1$) the required minimum conductivity for ion evaporation is $K = 1.3\ Si/m$ which is of the same order as seen experimentally,[21, 47].

At this very high field ions begin to evaporate from the liquid's surface with an ion current density (j_i). For the case of the cone-jet transition (meniscus), the current per unit length Λ is:

$$\Lambda = 2\pi h j_i \tag{3.57}$$

and the total accumulated ion current is:

$$I_i = \int_0^{z'} \frac{2\pi h j}{\cos\alpha} dz. \tag{3.58}$$

The total collected current is then $I_{tot} = I + I_i$. The ion current density j_i is discussed in more detail in the next section.

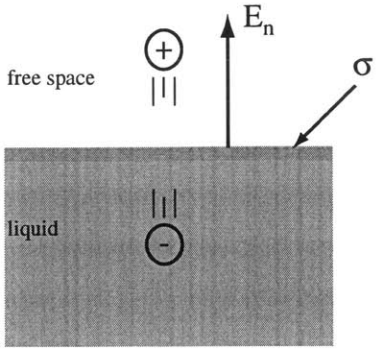

Figure 3-7: ion desorption from jet surface, image potential

3.4.1 Ion emission mechanism

Iribarne and Thompson developed a model based on absolute reaction theory to describe the extraction process with good results, [33]. Further work by Loscertales and Fernández de la Mora [46] on a more accurate model based on image potential theory, effectively a Schottky type model for the ion current density, gives:

$$j_i = \frac{\sigma K_B T}{h_p} \exp\left(\frac{W_{max} - G_0}{K_B T}\right) \tag{3.59}$$

where, σ is the surface free charge density, K_B is Boltzmann constant, T is the liquid temperature, h_p is Planck's constant, G_0 is the solvation energy of the ions. W_{max} is the Schottky depression which is function of the normal field E_n^o:

$$W_{max} = \left(\frac{q^3 E_n^o}{4\pi\epsilon_0}\right)^{1/2} \tag{3.60}$$

where q is the charge of the evaporated ions. A full derivation of this model is presented by Lozano [47]. Notice that if $W_{max} = 0$ the process is then thermally controlled. In this case for formamide ($G_0 \approx 1.7\ eV$) under standard conditions (T=300 K) Eq. 3.60 results in negligible evaporation since the exponential term is very small and overpowers the rest. Once the applied electrical field reaches a threshold limit things change dramatically. An order of magnitude estimate of the E-field for evaporation can be obtained by equating $W_{max} = G_0$ and solving for the field:

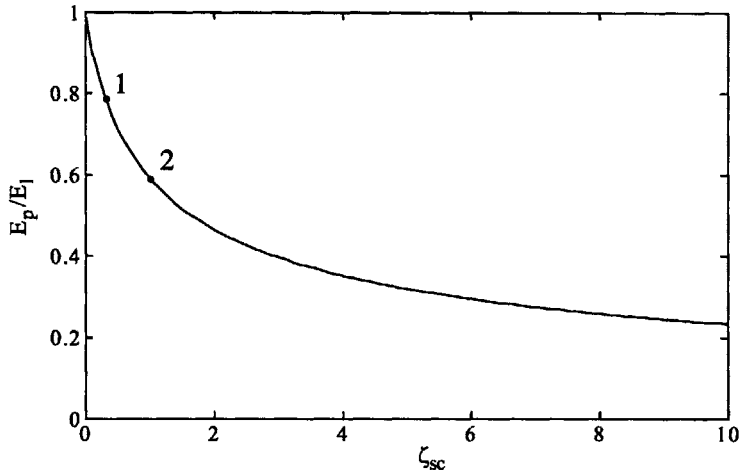

Figure 3-8: Space charge effect ζ_{sc}(Eq. 3.63) on field fraction (E_p/E_n^o), Eq. 3.62. Space charge is estimated based on formamide $K = 2.1\ Si/m$, $I_i = 400\ nA$, $\phi \approx 800\ V$, $q/m \approx 350 \times 10^3\ C/Kg$, and $E_p \approx 1\ V/nm$. (1) Refers to a jet radius $h = 10$ nm and (2) to a jet radius $h = 30$ nm

$$E^* = \frac{4\pi\epsilon_0 G_0^2}{q^3} \tag{3.61}$$

which for $G_0 = 1-2eV$ requires $E^* = 0.6-2.8V/nm$. Experimentally it has been found that only high conductivity $K \approx 1\ Si/m$ liquids are able to evaporate ions, for the reason discussed in connection with Eq. 3.56, [46, 21, 47].

Experimental studies have determined that in many cases the evaporated ions are solvated, [33, 46, 21, 47]. As an example for a formamide solution doped with NaI the charge to mass ratio of the Na^+ ions is estimated (from experimental data) at $q/m = 350,196\ C/Kg$, [47] . Assuming that the ions are singly charged, the evaporated ion mass is $m_i = 275$ amu. The ion mass is considerably larger than that of the Na^+ (23 amu) which suggests that ions are solvated. The degree of solvation i.e. the number of formamide molecules (m = 45 amu) per each Na^+ is estimated at $n_s = 4-5$ [47].

3.4.2 Space charge effects

One of the effects of ion evaporation from the liquid surface is that the in-flight ions will modify the surface potential distribution according to Poisson's equation $\nabla^2\phi = -\rho_e/\epsilon_0$ where ρ_e is the charge density distribution. The ion evaporation model is based on a one-

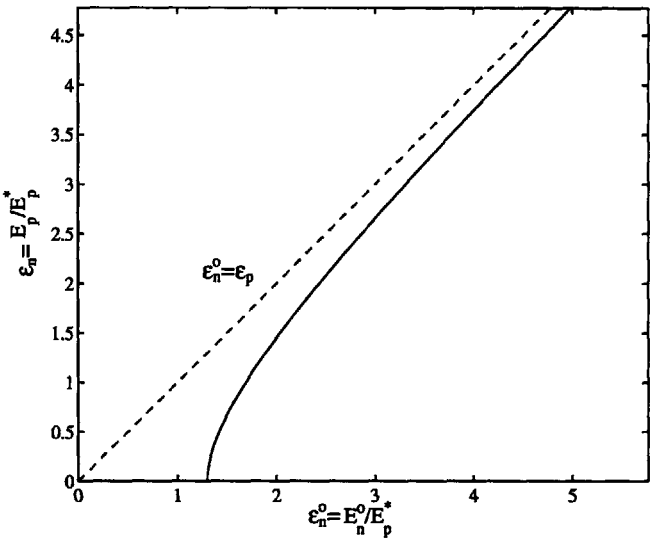

Figure 3-9: Space charge effect as given by equation 3.66. Notice the two limiting cases: Child-Langmuir space charge limited case $\varepsilon_p = 0$, and weak space charge case, $\varepsilon_n^o \to \infty$ and $\varepsilon_p \to \infty$

dimensional approximation derived by Stern *et al* [60] and reproduced by Prewett & Mair [57]. This model estimates the reduction of the electric field (Laplace field) due to the effect of space charge. The ratio of the the Poisson field (E_P) to the Laplace field (E_n^0) is given by

$$E_P = \frac{8E_n^o}{27\zeta_{sc}^2}\left(1 + \left(\frac{3}{2}\zeta_{sc} - 1\right)(1 + 3\zeta_{sc})^{1/2}\right) \tag{3.62}$$

where the dimensionless space charge strength is ζ_{sc} is given by

$$\zeta_{sc} = \frac{4j_i}{3\epsilon_0 E_p^2}\sqrt{\frac{\phi_B}{2q/m}}. \tag{3.63}$$

where j_i is the ion current density, ϕ_B the liquid potential at the extraction point, and q/m the charge to mass ratio of the extracted ions. In the limit where $\zeta_{sc} \ll 1$ (weak space charge), equation 3.62 becomes $E_P = E_n^0(1 - \zeta_{sc})$. For the case where $\zeta_{sc} \gg 1$, the result is the Child-Langmuir law for a diode (space-charge limited case):

$$j_{cl} = \frac{4\sqrt{2}}{9}\sqrt{\frac{q}{m}}\frac{\phi_B^{3/2}}{d^2} \tag{3.64}$$

and d is the distance over which space charge effects are important.

In figure 3-8 this simplified model is shown and two sample cases are presented. Based on experimental data for a formamide solution of high conductivity, [29] with two estimates of the corresponding jet radius $h = 10\ nm$ (point 1 figure 3-8), $h = 30\ nm$ (point 2 same figure). Note that this simple calculation shows that the fields may be modified by as much as 40% and may therefore significantly control the emission characteristics of the meniscus.

Formula 3.62 is deceiving, in that it gives E_p in terms of ζ_{sc}, which itself depends on E_P. A clearer representation may be obtained if we reexpress formula 3.63 in terms of $\zeta_{sc} = (E_p^*/E_p)^2$ where:

$$E_p^* = \sqrt{\frac{4j_i}{3\epsilon_0 E_p^2}} \left(\frac{\phi_B}{2q/m}\right)^{1/4} \tag{3.65}$$

which can be substituted into equation 3.62 and recast in the form:

$$\varepsilon_n^o = \frac{E_n^o}{E_p^*} = \frac{27/8}{\varepsilon_p^3 + [\frac{3}{2} - \varepsilon_p^2][\varepsilon_p^2 + 3]^{1/2}} \tag{3.66}$$

where $\varepsilon_p = E_p/E_p^*$. Equation 3.66 is plotted in figure 3-9. For the space charge limited case $\varepsilon_p = 0$ and the ion current density is that given by Child-Langmuir, formula 3.64 ($\varepsilon_n^o = \sqrt{27}/4$). For the opposite case weak space charge ($\varepsilon_n^o = \varepsilon_p$), actually $\varepsilon_n^o \to \infty$ and $\varepsilon_p \to \infty$. There is still the fact that ϕ_B enters in E_p^*, and it should not be the full surface potential, only the (unknown) potential drop in the space-charge region near the surface. This however, is harder to remove without a full 3D solution.

3.5 Summary

In this chapter a short summary of the relevant physics of colloid thrusters has been presented. The first part of the chapter concentrated on the Taylor cone as precursor to an emitting electrospray. Once a threshold voltage is reached the cone apex deforms and a thin jet emerges. Estimates of the size of the cone-to-jet transition region have been presented. The electrified jet's current is estimated based on analytical and semi-empirical scalings introduced by several authors. Finally, for some liquids of sufficiently high conductivity ion evaporation from their surface is observed. The physics of this evaporation process are discussed and a simple ion evaporation model is introduced.

Chapter 4

Cone–jet numerical model

In this chapter we derive the equations for the electrostatically accelerated free-jet flow. The derivation process is outlined and the simplifying assumptions employed are justified. The model includes viscous effects, charge relaxation effects, complete free surface boundary conditions, and the effects of the needle length on the liquid potential. Ion evaporation from the jet surface is added to the basic model as an extra module. The ion model includes a simplified space-charge effect E-field reduction model, as well as modifications to the conservation of mass and charge equations. Finally, boundary conditions for the system of equations are introduced.

4.1 Computational domain

Previous numerical work on cone–jet simulations has presented two main approaches to the upstream boundary condition of the cone flow. The first approach favored by Higuera, Cherney and others is to assume that far upstream from the transition zone the cone approaches, in the limit, Taylor's angle and becomes truly equipotential, [28, 6]. The reasoning behind this is that considering the disparity of length scales the cone–jet transition will be a local behavior without any major influence from the external electrode configuration. This idea is supported by Fernández de la Mora, who mentions that if the ratio of inner capillary radius vs jet radius is $h_0/hj \geq 100$ then the external electrostatics (i.e. electrode configuration) will have little effect on the transition behavior, [13]. Experimental photographic evidence presented by Gañán–Calvo *et al* shows that for a variety of flow rates and operating voltages, far from the transition region, the cone will not deviate much from Taylor's angle,

figure 2-2, [19]. On the other hand, the zeroth–order cone simulation of Pantano shows that equilibrium shapes at higher angles than Taylor's are physically possible, [55]. This is supported by photographic evidence from Taylor's original paper, ([62], Figure 2-2). It seems that under many circumstances imposing that upstream from the transition region the cone approaches Taylor's angle is not a bad assumption, but it may not be applicable to all conditions, as can be seen in Figure 2-3), [62]. Similar pictures have been obtained by Mangoubi and Lozano, some of those can be seen in Figure 2-4.

The second approach includes simulating the liquid cone–needle interface as done by Pantano, Yan, Hartman, Hohmann and this work, [55, 32, 27, 64]. These authors observed that the numerical results were affected by the electrode configuration. One thing to keep in mind is that in various cases other numerical codes have had problems, as is expected, at the liquid–solid interface (see section 4.6.)

4.2 Free jet model

The free jet numerical model for the cone-jet transition is based on the concepts put forth by Eggers, Dupont and Brenner for non-charged liquid free-jets. Their model was based in a "one-dimensional long wavelength approximation of the full hydrodynamic equations" as seen in Eggers & Dupont [10] and Brenner *et al* [1](see chapter 2). Their simulation results showed very good agreement with experimental data. The model we will present next extends some of these ideas to electrostatically accelerated jets.

Our simulation reproduces the basic setup of Fernández de la Mora & Loscertales with a conducting capillary needle facing a ground electrode at a distance L, as seen in Figure 4-1, [13]. The liquid is modelled as it emerges from the needle (i.e. flow inside the needle is not modelled) until it passes through the ground electrode screen.

Most free jet models (electrically charged or not) assume that the jet is axisymmetric and describe its form in cylindrical coordinates [1, 27, 32, 11]. In our case we have chosen spherical coordinates, due to the conical form of the problem in the essential upstream region, [15, 6]. The liquid surface is described using a local axisymmetric (about φ)conical approximation as seen in Figure 4-2. The free-surface boundary conditions are kept exact in order to preserve the correct equilibrium shapes for the jet but more importantly, for the cone section as suggested by Brenner *et al* [1]. The model uses continuum fluid equations

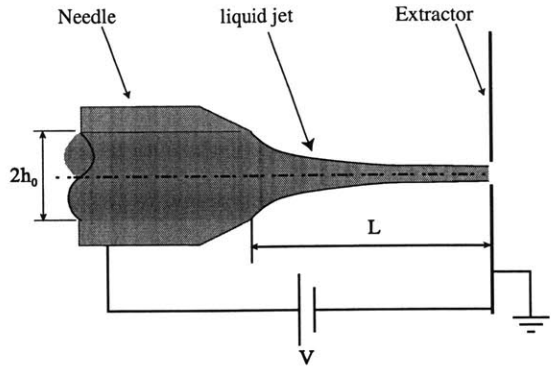

Figure 4-1: Simulation setup with conducting needle and ground extractor electrode

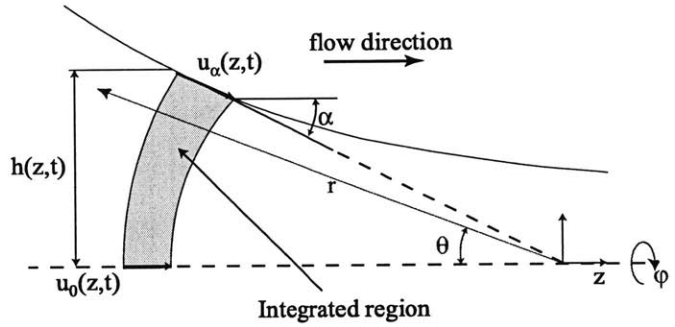

Figure 4-2: Local spherical coordinate system used for the derivation of the fluid equations

complete with viscous effects. Laplace's equation is solved to obtain the potential and electric fields, at the outer surface of the electrodes and of the liquid via a panel method. The formulation assumes that the liquid has a constant conductivity. This last point deserves some extra attention, because it is not immediately obvious how the charge carriers (ions) will redistribute themselves in the fluid, given the strong fields and accelerations present,(see Appendix A of [2]).

4.2.1 Fluid mass and momentum equations

A parametrically described parabolic velocity profile in the $r - direction$ is assumed, of the form

$$u_r(u_\alpha, u_0, \theta, \alpha) = -\left(u_0 + (u_\alpha - u_0)\left(\frac{\sin\theta}{\sin\alpha}\right)^2\right) \tag{4.1}$$

where u_α is the velocity at the jet surface, u_0 is the velocity at the symmetry axis, θ is the conical angle and α is the angle of the jet surface to the *z-axis* as seen in figure 4-2. This formulation will have problems in those cases when $\alpha \rightarrow 0$ and care is taken to obtain the physically correct limits in such cases.

A corresponding consistent velocity profile in the *transverse-direction* (increasing θ) is obtained by substituting the radial velocity profile, of equation 4.1 into the mass conservation equation (in spherical coordinates) and solving for u_θ

$$u_\theta = -\frac{1-\cos\theta}{r\sin\theta}\frac{\partial}{\partial r}\left(r^2\left[-u_0 - \frac{(1-\cos\theta)(2+\cos\theta)}{3}\frac{(u_\alpha - u_0)}{\sin\alpha^2}\right]\right) \tag{4.2}$$

The two velocity profiles are now substituted in the *r-component* and *θ-component* of the momentum equation in spherical coordinates and every term is integrated for θ. The force terms have been projected in the z-direction (axial) in order to obtain a more physically meaningful expression. The integration in the *θ-direction* is carried out from $\theta = 0°$ (the *z-axis*) to just underneath the surface of the colloid jet $\theta < \alpha$ at constant r.

$$\int_0^\alpha \left[(term)r^2\sin\theta\cos\theta\right]d\theta. \tag{4.3}$$

r is substituted by $r = h/\sin\alpha$ and derivatives are transformed according to

$$\frac{\partial(\,)}{\partial r} = -\cos\alpha\frac{\partial(\,)}{\partial z} \tag{4.4}$$

is order to relate the equations to the axial *z-direction.* A small angle approximation is made ($\alpha << 1$) and only terms up to α are maintained (i.e. $\alpha^n, n > 1$ are assumed small). The small angle approximation is not applied in two cases: the surface tension term of the normal surface boundary condition and for the calculation of the electrical fields on the surface of the liquid jet. The surface tension terms are kept exact so that the model equations reproduce the static equilibrium surfaces of the complete equations, [10].

A useful construct is to define two velocities, the mean velocity u and a "shear velocity", u':

$$u = \frac{u_\alpha + u_0}{2} \tag{4.5}$$

$$u' = \frac{u_\alpha - u_0}{2}. \tag{4.6}$$

This change of variables is only meant to simplify and compact the representation of the equations. The resulting equation of conservation of mass is given by

$$\frac{\partial(h^2)}{\partial t} = -\frac{\partial(h^2 u)}{\partial z} \tag{4.7}$$

where h is the local jet radius, and u is the average velocity as defined by equation 4.5. The net volumetric flow rate at a section is given by

$$Q = \frac{2\pi h^2}{1+\cos\alpha}\left[u_0 + \frac{(2+\cos\alpha)}{3(1+\cos\alpha)}(u_\alpha - u_0)\right] \tag{4.8}$$

from which the small angle approximation yields $Q \approx \pi h^2 u$ where Q is constant in the steady state, but can fluctuate in space and time during transients. The momentum equation in the *r-direction* becomes after much algebra and simplification:

$$\frac{\partial u}{\partial t} = -\frac{1}{2}\frac{\partial}{\partial z}(u^2 + \frac{u'^2}{3}) + \frac{u'}{h^2}\frac{\partial}{\partial z}(h^2(\frac{u}{2} + \frac{u'}{6})) - \frac{1}{\rho}\frac{\partial P_0}{\partial z} + \frac{8\nu u'}{h^2} + g_z. \tag{4.9}$$

and in the $\theta - direction$

$$P_\alpha - P_0 = -2\mu\frac{\partial u'}{\partial z}. \tag{4.10}$$

P_α denotes the pressure at the surface of the liquid, P_0 the liquid pressure at the jet axis, ν is the kinematic viscosity, and μ is dynamic viscosity.

4.2.2 Charge Conservation Equations

The electrical charge formulation of the system assumes that the fluid is undergoing a charge relaxation process with constant conductivity K. The movement of charges in the axial and radial direction is modelled by an internal (Figure 4-3, bulk control volume C.V.2) charge conservation equation which assumes that there are no free charges within the liquid, resulting in

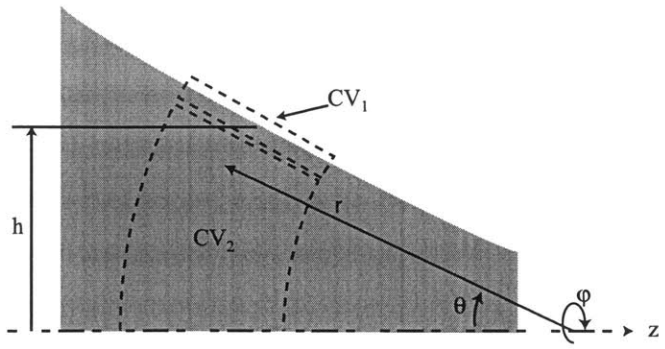

Figure 4-3: Section of the liquid jet showing the Control Volume C.V. 1 used to derive 4.12 and C.V. 2 used in the derivation of equation 4.11.

$$\frac{2\pi h K E_n^i}{\cos\alpha} + \frac{\partial}{\partial z}\left(\frac{2\pi K E_t h^2}{1+\cos\alpha}\right) = 0 \tag{4.11}$$

where E_n^i and E_t are the components of the internal electric field normal and tangent to the surface. The first term of equation 4.11 is the conduction current from the bulk to the surface ($\theta - direction$) while the second term is the rate of change of the conduction current in the axial direction.

The rate of charge accumulation on the surface (Figure 4-3, control volume C.V.1) is comprised of the surface charge convergence due to convection (left-hand-side) and charge contributed by the normal current density arriving from the bulk, $j_n = KE_n^i$.

$$\frac{\partial}{\partial t}(h\sigma) + \cos\alpha \frac{\partial}{\partial z}(h\sigma u_\alpha) = hKE_n^i \tag{4.12}$$

where σ is the free charge density at the liquid surface, and u_α is the surface velocity($u_\alpha = u + u'$). The free charge at the surface interface gives a jump condition between the internal (E_n^i) and external field (E_n^o) derived from Gauss law : $\sigma = \epsilon_o(E_n^o - \epsilon E_n^i)$,[5]. The tangential fields are not affected by the presence of free charges and are therefore continuous at the interface $E_t = E_t^o = E_t^i$. In the case of a fully relaxed fluid $E_n^i = 0$ which reduces the surface condition to $\sigma = \epsilon_o E_n^o$.

4.2.3 Free surface boundary conditions

The description of the free surface of the liquid jet requires normal and tangential stress balance boundary conditions. The normal condition is given by :

$$\Delta P = P_\alpha - P_v = \gamma\kappa + \mu\|\hat{n}\cdot\tau\cdot\hat{n}\| - \|\hat{n}\cdot T^E\cdot\hat{n}\| \tag{4.13}$$

where P_α is the pressure inside the liquid just below the surface, P_v is the pressure outside the liquid equal to zero in vacuum, κ represents the local curvature of the liquid, τ the viscous stress tensor and T^E the quasi-equilibrium electrical stress tensor formulation of Landau & Lifshitz [41]

$$T^E = \epsilon\epsilon_0\vec{E}\vec{E} - \frac{1}{2}\epsilon\epsilon_0\left[1 - \frac{\rho}{\epsilon}\left(\frac{\partial\epsilon}{\partial\rho}\right)_T\right]\vec{E}\cdot\vec{E}\delta \tag{4.14}$$

where δ is Kronecker's delta. For the normal and tangential directions the electrical stress interface condition become:

$$\|\hat{n}\cdot T^E\cdot\hat{n}\| = \frac{\epsilon_0}{2}\left[(E_n^o)^2 - \epsilon(E_n^i)^2 + (\epsilon-1)E_t^2\right] \tag{4.15}$$

$$\|\hat{n}\cdot T^E\cdot\hat{t}\| = (\epsilon_0 E_n^o)E_t \tag{4.16}$$

where it is assumed that $d\epsilon/d\rho = 0$. One modification is made to the equilibrium formulation of Landau & Lifshitz [41] where for $\|\hat{n}\cdot T^E\cdot\hat{t}\|$ we substitute $\sigma_{relaxed} = \epsilon_0 E_n^o$ for σ which is not, in general, fully relaxed.

The normal viscous stress is expressed in spherical coordinates and a small angle approximation is made leaving only the leading terms. This approximation is made on the grounds that viscous stresses are assumed to be much smaller than the surface tension and electric stresses.

The normal surface condition is now expressed as

$$P_0 = \gamma\left(\frac{1}{h\left(1+\left(\frac{\partial h}{\partial z}\right)^2\right)^{1/2}} - \frac{\frac{\partial^2 h}{\partial z^2}}{\left(1+\left(\frac{\partial h}{\partial z}\right)^2\right)^{3/2}}\right) + \mu\left(\frac{2\alpha u'}{h} - \frac{\partial u}{\partial z}\right)$$

$$- \frac{\epsilon_0}{2}\left[(E_n^o)^2 - \epsilon(E_n^i)^2 + (\epsilon - 1)E_t^2\right] \tag{4.17}$$

where P_α has been eliminated by using equation 4.10. The tangential boundary condition expresses a balance between the viscous shear stresses and the corresponding tangential electrical stress.

$$u' = \frac{\sigma E_t h}{4\mu}. \tag{4.18}$$

4.3 Electrostatic problem

The electrostatics of the needle-liquid jet system are described by Laplace's equation ($\nabla^2\phi = 0$). This description neglects any space charge effects due to evaporated ions from the cone–jet surface. In those cases where ion evaporation becomes important a correction to the Laplacian field is made, see section 4.4. The relationship between the potential ϕ and the external normal field E_n^o is complex since every charge in the system (on the liquid as well as on the electrodes) influences each local potential. The problem is further complicated by the fact that while the system of equations is time marched the shape of the jet and the total charge at the surface will fluctuate thus modifying the potential and electric field of the system. Laplace's equation is solved using a panel method described in detail in section 5.2

4.4 Field enhanced ion evaporation

One of the effects of ion evaporation from the liquid surface is that the in-flight ions will modify the surface potential distribution according to Poisson's equation $\nabla^2\phi = -\rho_e/\epsilon_0$ where ρ_e is a charge density distribution. The ion evaporation model is based on a one-dimensional approximation derived by Stern *et al* [60] and reproduced by Prewett & Mair [57]. This model estimates the reduction of the electric field (Laplace field) due to the effect of space charge. The ratio of the Laplace field (E_n^0) to the Poisson field (E_P) is given by equation 3.62 and the ion current density by 3.59.

The rate of charge accumulation on the surface (control volume C.V.1, Figure 4-3) is comprised of the surface charge convergence due to convection (left-hand-side) and charge contributed by the normal current arriving from the bulk, $j_n = KE_n^i$, and that emitted by

the extracted ions.

$$\frac{\partial}{\partial t}(h\sigma) + \cos\alpha \frac{\partial}{\partial z}(h\sigma u_\alpha) = h(j_n - j_i)\cdot \tag{4.19}$$

Mass conservation is also affected by the evaporation of ions from the liquid surface. The effect is captured by the last term of the R. H. S. of equation :

$$\frac{\partial(h^2)}{\partial t} = -\frac{\partial(h^2 u)}{\partial z} - \left(\frac{m}{q}\right)_{ion} \frac{j_i}{\rho}. \tag{4.20}$$

4.5 Total current computation

The total current carried at a section of the jet is computed as the sum of convective, conductive, and free ion parts. The surface convective current I_{cv} due to the convected free charges at the surface of the jet is:

$$I_{cv} = 2\pi\sigma h(u + u') \tag{4.21}$$

where h is the jet radius, u is the average velocity, u' is the difference between the axial surface velocity and centerline velocity. The bulk conduction current I_{cd}:

$$I_{cd} = \frac{2\pi K h^2 E_t}{(1 + \cos\alpha)} \tag{4.22}$$

where K is the liquid conductivity, E_t is the tangential electric field and α is the angle of the jet surface relative to the centerline. Finally the accumulated ion current is

$$I_i = \int_0^{z'} \frac{2\pi h j}{\cos\alpha} dz\cdot \tag{4.23}$$

In the steady state, $I = I_{cv} + I_{cd} + I_i = const$, but I depends on time and space during the transients.

4.6 Boundary conditions

The mass and momentum equations require upstream boundary conditions. For the mass conservation equation (Eq. 4.7) the radius is set equal to the needle's inner radius ($h(0) = h_0$). The average velocity $u(0)$ is specified as $u(0) = Q/(\pi h_0^2)$. The surface charge density

boundary condition $\sigma(0)$ (i.e. liquid–needle interface) depends on the details of the electrode setup as well as the imposed fields as noted by Feng, [11]. To deal with this issue different approaches have been proposed. Pantano used an analytical approximation to take care of the singularity at the interface of his perfectly conducting liquid, [55]. Hohman *et al*, experimented with different values for the charge density in the liquid at this point. They concluded that the better results were obtained when its value was set to zero or near zero. Another important point made by Hohman was that it is important to include the fringe fields since experimentally it has been seen that they contribute in determining both shape and stability of the cone–jet, [32]. Hartman *et al* noticed that the cone shape calculation was quite unstable. They noticed that their error minimization code was able to converge (to zero error) if an appropriate value for liquid angle at the liquid–needle interface was chosen,[27]. Feng used an approximate model to calculate the E-field (based on Hohman's) and experimented with various values for the surface charge density boundary condition. From his results he noted that the actual boundary condition value only had an effect within a thin boundary layer ($0 < z < z_{bl}$) far from the transition. For $z > z_{bl}$ the behavior of the surface charge density became almost independent of its upstream boundary condition, [11].

In our case, our simulation includes the needle and liquid jet. The surface charge density boundary condition is updated based on the evolution of the E-field distribution. We have assumed that surface charge at the liquid-needle interface is fully relaxed and is therefore given by $\sigma(0) \approx \epsilon_0 E_n^0(1)$.

Chapter 5

Numerical Solvers

In this chapter we address the numerical approach for solving the system of equations derived in chapter 4. The system of equations can be subdivided into two coupled subsets: the first one describes the evolution of the jet (fluid mechanics) and its electrical charges, and the second one its potential distribution (electrostatics). Changes in one of the subsets reflect in the other. Our approach is to solve them sequentially until a steady state solution is reached. For each subset we present the numerical solver employed, the discretization schemes used, and the boundary and initial conditions required. Finally we address the interaction between both subsets as well as some practical information regarding gridding, time-stepping, etc.

5.1 Time dependent jet evolution

The system of equations presented in chapter 4 is split in two subsets which are solved sequentially. The first subsystem is comprised by the time dependent fluid equations, charge relaxation equations, and surface boundary conditions:

1. mass conservation, Eq. 4.7

$$\frac{\partial(h^2)}{\partial t} = -\frac{\partial(h^2 u)}{\partial z}$$

2. momentum conservation, Eq. 4.9

$$\frac{\partial u}{\partial t} = -\frac{1}{2}\frac{\partial}{\partial z}(u^2 + \frac{u'^2}{3}) + \frac{u'}{h^2}\frac{\partial}{\partial z}(h^2(\frac{u}{2} + \frac{u'}{6})) - \frac{1}{\rho}\frac{\partial P_0}{\partial z} + \frac{8\nu u'}{h^2} + g_z$$

3. surface charge relaxation, Eq. 4.12

$$\frac{\partial}{\partial t}(h\sigma) = -\cos\alpha\frac{\partial}{\partial z}(h\sigma(u_\alpha)) + hKE_n^i$$

4. normal surface boundary condition

$$\begin{aligned} P_0 &= \gamma\left(\frac{1}{h\left(1+\left(\frac{\partial h}{\partial z}\right)^2\right)^{1/2}} - \frac{\frac{\partial^2 h}{\partial z^2}}{\left(1+\left(\frac{\partial h}{\partial z}\right)^2\right)^{3/2}}\right) + \mu\left(\frac{2\alpha u'}{h} - \frac{\partial u}{\partial z}\right) \\ &- \frac{\epsilon_0}{2}\left[(E_n^o)^2 - \epsilon(E_n^i)^2 + (\epsilon - 1)E_t^2\right] \end{aligned}$$

5. tangential surface boundary condition

$$u' = \frac{\sigma E_t h}{4\mu}$$

5.1.1 Time marching numerical solver

The numerical scheme employed for time marching these equations is a general purpose fourth order Runge–Kutta. This is a well established time stepping scheme, which employs an explicit time integration method that has been successfully used in the past to solve the Euler equations, [35, 30]. For an initial value problem of the form $y' = f(t, y)$ the Runge-Kutta scheme is given by:

$$
\begin{aligned}
k^{(1)} &= f(t^n, y^n) \\
k^{(2)} &= f\left(t^n + \frac{\Delta t}{2}, y^n + \frac{k^{(1)}}{2}\right) \\
k^{(3)} &= f\left(t^n + \frac{\Delta t}{2}, y^n + \frac{k^{(2)}}{2}\right) \\
k^{(4)} &= f\left(t^n + \Delta t, y^n + k^{(3)}\right) \\
y^{(n+1)} &= y^n - \frac{\Delta t}{6}(k^{(1)} + 2k^{(2)} + 2k^{(3)} + k^{(4)})
\end{aligned}
\tag{5.1}
$$

This is a general version of the scheme. For fluids problems, however, the time dependent and spatial part can usually be separated as:

$$
\frac{dy}{dt} = -f(y) \tag{5.2}
$$

where the right hand side only has space derivatives and source terms. The scheme may then be written as:

$$
\begin{aligned}
k^{(1)} &= y^n \\
k^{(2)} &= y^n - \frac{\Delta t}{2}\,\overline{f(k^{(1)})} \\
k^{(3)} &= y^n - \frac{\Delta t}{2}\,f(k^{(2)}) \\
k^{(4)} &= y^n - \Delta t\,\overline{f(k^{(3)})} \\
y^{(n+1)} &= y^n - \frac{\Delta t}{6}\,(k^{(1)} + 2k^{(2)} + 2k^{(3)} + k^{(4)})
\end{aligned}
\tag{5.3}
$$

From a stability analysis this scheme is seen to be conditionally stable for central differenced convection equations, [30]. The basic Runge-Kutta scheme described above has been modified to include residual smoothing, and artificial viscosity terms. The residual smoothing is in essence an averaging process:

$$
\overline{f(y)}_i = \varepsilon[f(y)_{i-1} + f(y)_{i+1}] + (1 - 2\varepsilon)f(y)_i \tag{5.4}
$$

where ε is a constant parameter set in this case to 0.1. Hirsch points out that it is

sufficient to apply this modification to alternate stages (2^{nd} and 4^{th} in this case), assuming that ε is large enough, [31]. The numerical or artificial viscosity terms (N.V.T.) are applied to the momentum's equation right hand side (R.H.S) at every stage of the Runge-Kutta solver (i.e. $RHS(NVT) = RHS + NVT$). The form of the numerical viscosity is that proposed by Eggers and Dupont [10] and analogous to:

$$\frac{-1}{h^2}(h^2\overline{v}v_z)_z \tag{5.5}$$

where $\overline{v} = \nu_n v \Delta z$ where $\nu_n > 0$. The finite difference version is :

$$\overline{v}_{i+1} = \frac{\Delta z_i v_{i+1} + \Delta z_{i+1} v_i}{\Delta z_i + \Delta z_{i+1}} \tag{5.6}$$

$$h^2\overline{v}v_z|_{i+1} = h_{i+1}^2(v_{i+1} - vi)\nu_n\overline{v}_{i+1} \tag{5.7}$$

$$NVT = \frac{-1}{((h_{i+1} + h_i)/2)^2}\frac{h^2\overline{v}v_z|_{i+1} - h^2\overline{v}v_z|_i}{\Delta z_i} \tag{5.8}$$

The artificial viscosity is added to dissipate the high frequency oscillations seen around discontinuities and sharp gradients in second order central difference formulations. The basic idea is to replicate the viscous term of the momentum equation on the scale of the grid (mesh for 2–dimensional cases). The formulation is such that the N.V.T. induced upwinding is applied locally near the discontinuities and becomes negligible in smooth regions, [35, 31, 10].

5.1.2 Spatial discretization

The right hand side of the time marched equations , $f(y)$ (Eq. 5.2), is discretized on a non-uniform grid. The grid has a higher concentration of nodes near the needle exit. The rationale is that the steeper gradients will occur near the needle's exit. Due to the non-uniformity of the grid we use non-uniform second order finite difference formulas to approximate the derivatives. For the first derivative (2^{nd} order central difference):

$$(f_z)_i = \frac{1}{\Delta z_i + \Delta z_{i+1}}\left[\frac{\Delta z_i}{\Delta z_{i+1}}(f_{i+1} - fi) + \frac{\Delta z_{i+1}}{\Delta z_i}(f_i - f_{i-1})\right] - \mathbf{R}\left(\frac{\Delta z_i \Delta z_{i+1}}{6} f_{zzz}\right) \tag{5.9}$$

one sided differences are used for end points. The forward difference is:

$$(f_z)_i = \left(\frac{\Delta z_{i+1} + \Delta z_{i+2}}{\Delta z_{i+2}} \frac{(f_{i+1} - fi)}{\Delta z_{i+1}} - \frac{\Delta z_{i+1}}{\Delta z_{i+2}} \frac{(f_{i+2} - f_i)}{\Delta z_{i+1} + \Delta z_{i+2}}\right) + \mathbf{R}\left(\frac{\Delta z_{i+1}(\Delta z_{i+1} + \Delta z_{i+2})}{6} f_{zzz}\right) \tag{5.10}$$

For reference these formulas are taken from Hirsch [30], but they are derived from a Taylor series expansion. Second derivatives are calculated by differentiating (with the same schemes) the first derivatives.

5.2 Electric potential calculation

The second part of the problem requires us to calculate the electric potential, and electric field intensities at the surface of the liquid which will vary as the surface charges and the liquid jet shape fluctuate. As mentioned in chapter 4 this requires the solution of Laplace's equation. A full two dimensional axisymmetric solution is one option, but it would require mesh refinement near the jet surface to capture accurately the effect of the surface charge density. The challenge here is that the jet shape and surface charge are fluctuating, and therefore the mesh refinement would have to be adaptive and computationally expensive. A second approach is to use a boundary element solver, as previously employed by Lozano *et al* [48],Khayms [38], and Pantano *et al* [55]. This method yields only the fields and potential at the surface of the liquid and needle, which is sufficient for our purposes. This subset of equations is comprised by:

1. internal charge conservation 4.11

$$\frac{2\pi h K E_n^i}{\cos\alpha} + \frac{\partial}{\partial z}\left(\frac{2\pi K E_t h^2}{1+\cos\alpha}\right) = 0 \tag{5.11}$$

2. potential equation as function of total charges

$$\phi = f(z, h, E_n^o, E_n^i) \tag{5.12}$$

3. Tangential field equation (Laplace's equation)

$$E_t = -\cos\alpha \frac{d\phi}{dz} \tag{5.13}$$

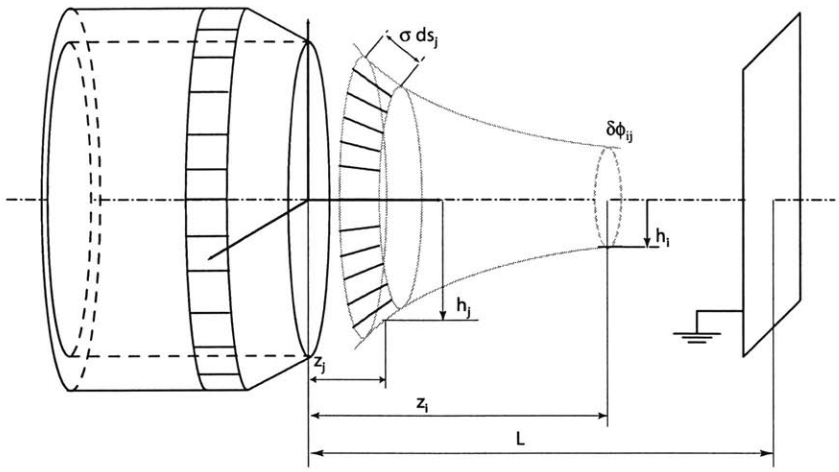

Figure 5-1: Depiction of the ring elements used to calculate the normal and tangential electric fields on the surface of the jet.

The total charge (free + dipoles) per unit length in the jet and cone is discretized into rings, and the joint potential of these rings, their images on a ground plane, and the free charge on an equipotential feed tube, acting as the emitter is computed on points on the liquid surface, thus yielding, by differentiation, the tangential field. As illustrated in figure 5-1 the contribution of a ring of charge j to the potential at i is calculated by

$$\delta\phi_{ij} = \frac{\sigma_j^T ds_j h_j}{4\pi\epsilon_0}\frac{2}{\sqrt{a}}\int_0^{\pi}\frac{d\varphi}{\sqrt{1-\frac{b}{a}\cos\varphi}} \tag{5.14}$$

$$a = h_i^2 + h_j^2 + (z_i - z_j)^2 \tag{5.15}$$

$$b = 2h_i h_j \tag{5.16}$$

The electrostatic boundary surface element solver has been modified from its original form as presented by Lozano *et al* [48]. In Lozano's case the electrical charges were assumed to be fully relaxed, so that $\sigma^T = \epsilon_0 E_n^o$. In our case the liquid is not fully relaxed such that $\sigma^T = \epsilon_0(E_n^o - E_n^i)$. Expression 5.14 can be integrated in terms of complete elliptic integrals of the first kind *K(m)*, and the potential at node i can be expressed as a linear superposition of those due to all the elements dz_j as

$$\delta\phi_i = N_{ij}(\sigma^T)_j \tag{5.17}$$

where

$$N_{ij} = \frac{1}{2\pi\epsilon_0}[\sqrt{m}K(m) - \sqrt{m_i}K(m_i)]\sqrt{\frac{h_j}{h_i}}\frac{\delta z_j}{\cos\alpha_j} \tag{5.18}$$

$$m = \frac{4h_ih_j}{(z_i - z_j)^2 + (h_i + h_j)^2} \tag{5.19}$$

$$m_i = \frac{4h_ih_j}{(z_i - z_j + 2L)^2 + (h_i + h_j)^2} \tag{5.20}$$

The ground electrode is simulated by adding a mirror image about $z = L$ of every ring. The images are denoted by $(m_i, K(mi))$. The full matrix N_{ij} is then partitioned into blocks representing potential at liquid points due to charges on liquid elements (N_{ll}), potential at liquid points due to charges on the metal supply tube (N_{lt}), etc. The liquid (ϕ^l) and needle (ϕ^t) potential are expressed in matrix form by

$$\begin{bmatrix} \phi^l \\ \phi^t \end{bmatrix} = \begin{bmatrix} N_{ll}N_{lt} \\ N_{tl}N_{tt} \end{bmatrix} \begin{bmatrix} \sigma_l^T \\ \sigma_t^T \end{bmatrix}. \tag{5.21}$$

Noticing that $\phi^t = V$ is the applied voltage we obtain a single equation:

$$B = N_{lt}N_{tt}^{-1}V \tag{5.22}$$

$$\bar{A} = (N_{ll} - N_{lt}N_{tt}^{-1}N_{tl}) \tag{5.23}$$

$$\phi^l = B + \bar{A}[\epsilon_0(E_n^0 - E_n^i)] \tag{5.24}$$

where the vector B comprises the effect of charges on the needle on the liquid potential and the full matrix $\overline{A}$ the effect of liquid charges on the liquid potential [48]. The electrostatic solver neglects any external space charge effects and assumes that the non-neutral and ambipolar layers of the liquid are thin.

The electrostatic equations 5.24, 5.13, and the conservation of internal charge 4.11, are used to obtained the new spatial distributions of E_n, E_t, and ϕ for the updated jet shape (h, α), velocity (u), and surface charge of the jet (σ). This procedure is an analog of the Poisson solving step in a Particle in Cell (PIC) codes. The new field and potential distribution is calculated by using a modified internal charge conservation equation, [26]:

$$\frac{dE_n}{dt} \equiv HEn \tag{5.25}$$

where the right hand side is the steady state internal charge conservation, Eq. 5.11:

$$HEn = \frac{\sigma}{\epsilon_0} - E_n^0 + \frac{\epsilon \cos\alpha}{2\pi h K} \frac{\partial}{\partial z} \left(\frac{2\pi K E_t h^2}{1+\cos\alpha} \right). \tag{5.26}$$

The modified equation is time marched to steady state ($dE_n/dt \rightarrow 0$) using an RK4 scheme. At each stage of the RK4 iteration equations 5.24 and 5.13 are used to obtain a closed system of electrostatic equations. In more detail at each stage of the RK4 HEn is recalculated using the value of E_t from the previous stage. This HEn is used to obtain a new E_n^{new} and subsequently ϕ_l^{new} and E_t^{new} as shown next:

$$\begin{aligned}
HEn &= \frac{\sigma}{\epsilon_0} - E_n^0 + \frac{\epsilon \cos\alpha}{2\pi h K} \frac{\partial}{\partial z} \left(\frac{2\pi K E_t h^2}{1+\cos\alpha} \right) && (5.27)\\
E_n^{new} &= E_n^0 + \frac{\Delta t_e}{\beta_i} HEn && (5.28)\\
\phi_l^{new} &= B + \bar{A}[\epsilon_0 (E_n^{new} - E_n^i)] && (5.29)\\
E_t^{new} &= -\cos\alpha \frac{d}{dz} (\phi_l^{new}) && (5.30)
\end{aligned}$$

where the coefficient β changes for each of the i stages $\beta_i = 1.0, 2.0, 2.0, 1.0$ where $i = 1, 2, 3, 4$. These new values are used as updated predictors for the subsequent stages of the solver. At the end of each complete loop the normal field is computed :

$$(E_n^0)^{m+1} = (E_n^0)^m + \frac{\Delta t_e}{6} (HEn_1 + 2HEn_2 + 2HEn_3 + HEn_4) \tag{5.31}$$

Once $(E_n^0)^{m+1}$ is computed the potential ϕ_l^{m+1}, and tangential E_t^{m+1} fields are updated as well from Equations 5.13, and 5.24. The iteration continues until the desired level of convergence is achieved. After trial and error the non-dimensional "time step" and required number of iterations were set to $\Delta t_e = 5 \times 10^{-5}$ and 5000 iterations.

In order to check that the effects on the liquid potential due to needle length are calculated correctly they are checked against those obtained with the Maxwell code, [53]. This independent check benchmarks the electrostatic subset. The checks are carried out only considering the needle and ground electrode setup, i.e. no liquid jet. The needle is set at

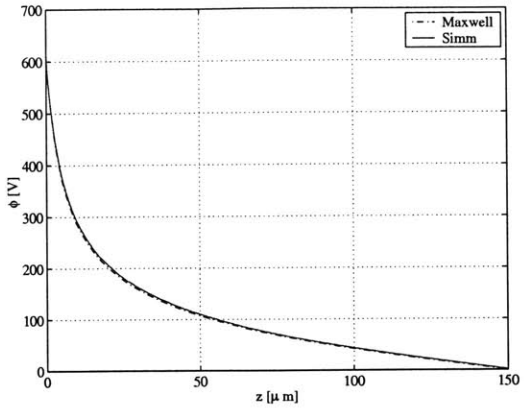

Figure 5-2: Comparison of numerical solutions for a finite length needle– electrode arrangement

an operating potential V relative to the ground electrode. The Maxwell simulation is an axisymmetric full 2–D simulation and the potential drop between the needle and electrode is read at the symmetry axis. These results are compared to those obtained with our panel method. For the case with no liquid charges the potential at the liquid surface is calculated by:

$$\phi^l = B = N_{lt} N_{tt}^{-1} V \tag{5.32}$$

where the liquid surface charge is zero from equation 5.24. The comparison between both codes is not direct, since one is read at the axis of symmetry and the other at the liquid surface (effects due to liquid charges are ignored). The difference between the two cases is minor due to the fact that the liquid jet is $h_j << h_0$ Our results are shown in figure 5-2. The results match each other very closely, the differences being of the order of 2–3 Volts at each location.

In figure 5-3 we can see the effect of increasing the aspect ratio $\mathbf{R} = Lt/(2h_0)$ of the conducting needle. These results clearly show that if the electrode configuration is modified the potential distribution is affected dramatically. However, as the aspect ratio continues increasing the effect tends to a limiting value (although the aspect ratio of the needle is of the order $\mathbf{R} \approx 1000$).

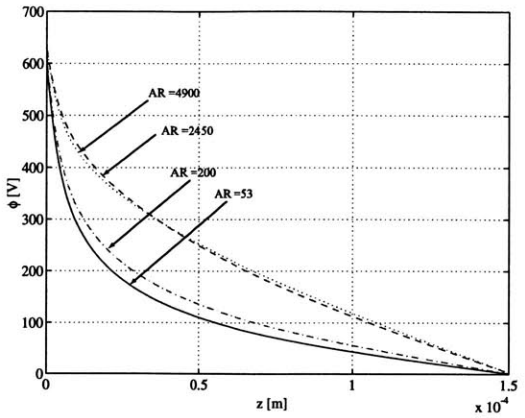

Figure 5-3: Effect on needle–ground potential distribution for increasing needle aspect ratio ($Lt/2h_0$)

5.3 Integration of solvers

The two subsets described above are solved sequentially using the updated information of one to update the other until steady state is reached.

In detail the time dependent equations (4.7, 4.9, and 4.12) are time marched for n steps while holding the electrical fields constant (E_n^0 and E_t). After these n-steps, the electric field is updated with the new values for radius (h), velocity (u and u'), and surface charge (σ). The number of steps $n < t_e/\Delta t$ where $t_e = \epsilon\epsilon_0/K$ is the electrical relaxation time and Δt is the time-step. A second criterion used to choose the time step is to ensure that the $C.F.L.$ condition is satisfied in order to preserve the stability of the Runge-Kutta scheme. Typical values for Δt are of the order of $10^{-9} sec.$ Trial and error were used to find a good operating point.

For the electrostatic solver the number of iterations and its time-step where by trial and error since the iteration is based on a fictitious time dependence.

5.3.1 Gridding

Ideally the grid used for discretizing the system of equations would be homogeneous, with sufficient resolution to capture the cone to jet transition. Practical considerations, however, discourage this approach. On one hand the first subset of equations (subsection 5.1) benefits from having a fine grid that allows high definition of the transition zone. On the other

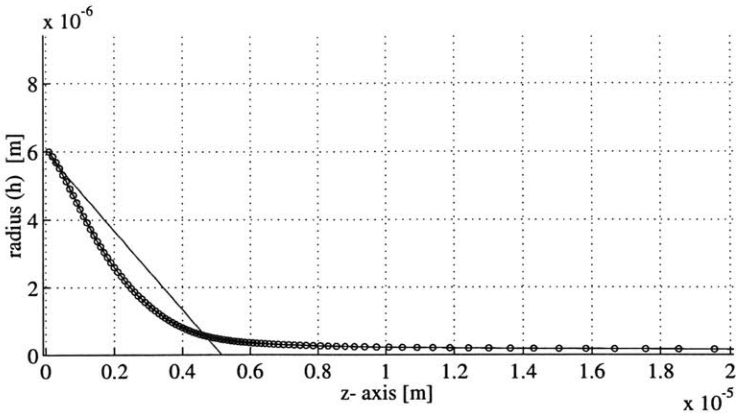

Figure 5-4: Jet radius vs z-axis for a typical simulation. Needle exit radius $h_0 = 6\mu m$, total length of liquid domain $L = 150\mu m$. The markers show the z-axis position of the grid nodes, notice the higher density near the needle exit.

hand the electrostatic calculation (subsection 5.2) becomes increasingly expensive with fine grids. For a grid with M nodes the electrostatic solver has to deal with a full matrix N with $M \times M$ entries (Eq. 5.18), therefore, using a fine grid benefits the fluid part but makes the electrostatic calculation much more expensive. From a physics point of view, most of the action occurs at the transition region once the jet is formed there are no strong gradients which suggests that there is no need for high resolution in the jet region. For these reasons a non-uniform grid is employed. This grid has a high resolution near the cone-jet transition region and a decreasing resolution in the jet region, as seen in Figure 5-4 for a typical case. For the most part the minimum grid spacing ($\Delta z_i = z_{i+1} - z_i$) is set such that the jet radius $h > \Delta z$.Typically for the high resolution section the spatial resolution should be about a factor of 10 smaller than jet radius ($\Delta z \approx min(h_{jet})/10$).

5.3.2 Initial and boundary conditions

Initial conditions for this simulation were obtained by starting with a jet at high flow rate and no voltage. The reason for this is that the initial conditions for the surface charge density, as well as the electric fields are unknown. Alternatively analytical estimates may be used as initial conditions. In our case we decided to use the first approach since it would give us a gentler initial condition for each case. Subsequent runs lowered the flow rate and increased the operating voltage. Each run used as initial conditions the data from the

previous converged solution, finally leading to the regime of interest.

Upstream boundary conditions are stipulated for the mass conservation, momentum, and charge relaxation equations. As mentioned before the simulation reproduces the basic setup of [13] with a conducting capillary needle facing a ground electrode at a distance L. For the time dependent equations boundary conditions are given only for the upstream end (needle exit). The initial jet radius is set equal to the needle inner radius (h_0), the velocity is set as $u_0 = Q/(\pi h_0^2)$. The surface charge density boundary condition is specified as described in section 4.6. The applied operating voltage is given by equation 3.15

5.3.3 Residue calculation

The convergence of the simulation is monitored by keeping track of the residues for each of the subsets. For the time dependent equations the residues are defined for the radius (h), velocity (u), and surface charge per unit length (uh):

$$RES_h = \max\left(\frac{h^{n+1} - h^0}{\Delta t}\right) \tag{5.33}$$

$$RES_u = \max\left(\frac{u^{n+1} - u^0}{\Delta t}\right) \tag{5.34}$$

$$RES_{\sigma h} = \max\left(\frac{(\sigma h)^{n+1} - (\sigma h)^0}{\Delta t}\right) \tag{5.35}$$

Theoretically as time approaches infinity the residues should approach zero for a stable scheme with solutions. In practice the degree of convergence is dictated by practical considerations such as an acceptable variation of the solution.

As mentioned above the potential solver is run every n number of steps to update the E-field and potential distribution. For the potential solver the residues are:

$$RES_{En} = \max\left(E_n^{n+1} - E_n^0\right) \tag{5.36}$$

$$RES_{Et} = \max\left(E_t^{n+1} - E_t^0\right) \tag{5.37}$$

$$RES_{\phi} = \max\left(\phi^{n+1} - \phi^0\right) \tag{5.38}$$

In this case, it is also checked that the fluctuations of the variables tend to zero. other

parameters that are checked for convergence are the total current which should be constant along the jet ($dI/dz = 0$), the calculated flow rate at every axial location should also be constant and equal to the one specified as upstream boundary condition. Through post-processing an energy breakdown is made in order to check that energy has been conserved (see section 6.2.3).

5.4 Summary

In this chapter the numerical schemes used to solve the system of numerical equations developed in chapter 4 have been presented. The equations are separated in two subsets: time dependent electrohydrodynamics and electrostatic sets. The details of the numerical scheme used in each case have been presented along with their corresponding initial and boundary conditions. Finally, the integration of both solvers has been presented.

Chapter 6

Results for droplets

6.1 Results and discussion

In the following, we present a comparison of our numerical results for emitted current to experimental data from Fernández de la Mora & Loscertales [13]. Our numerical simulations have validated Fernández de la Mora current vs. flow equation to within experimental accuracy, and have also loosely confirmed his empirical minimum flow condition. But in addition, they have illuminated the inner workings of the electrospray phenomenon and have uncovered subtle variations on the general theme. Some of these are in retrospect, understandable from simple basic balances, others remain obscure. We attempt to combine numerical results and observations with basic principles to see if a clear pattern can be discovered.

6.1.1 Reference experiments

Fernández de la Mora and Loscertales experimental data were obtained using a fairly standard electrospray setup where the meniscus emerged from the end of a stainless steel capillary needle facing a perpendicular flat ground electrode (9 mm away from the needle, in most cases). Two sizes of needles were used: one with 1.07 mm OD and 0.81 mm ID, and the other with 0.41 mm and 0.24 mm respectively. The experiments were conducted at laboratory pressure and temperature (and in the case of H_2O with a CO_2 atmosphere to prevent breakdown). Current measurements were made with an electrometer connected between the collector electrode and ground. The flow rate was controlled by an imposed pressure

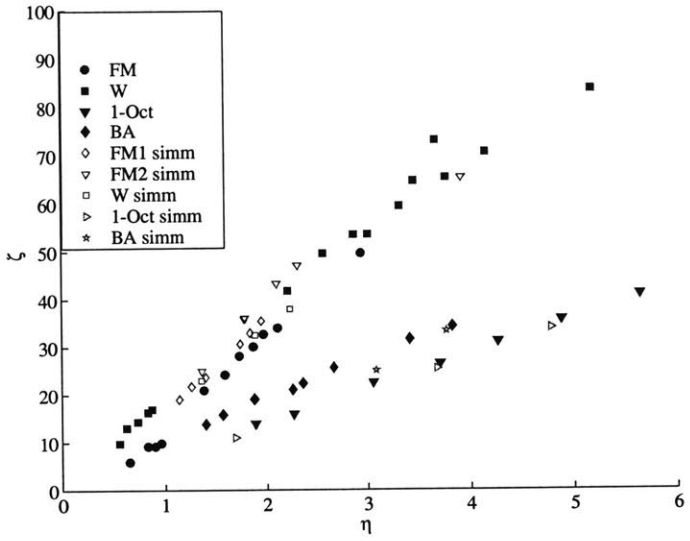

Figure 6-1: Dimensionless spray current ζ [Eq. 3.51] versus η [Eq. 3.50] comparison between experimental (shaded symbols) and numerical data(unshaded symbols). Experimental data from [13].Numerical data based on various liquids (Table 6.1) and flow rates ($\eta > 1$).

difference ΔP and was inferred in many cases from the linear relation $\Delta P/Q$ obtained experimentally at higher Q (originally calibrated by the moving bubble front method).

6.1.2 Numerical results and Comparison

Figure 6-1 shows a comparison of the numerically computed results versus experimental data using η and ζ, from equations 3.50 and 3.51. The properties of the liquids employed in the simulations can be seen in Table 6.1. It can be seen that the numerically computed currents compare quite well to the experimentally observed values of Fernández de la Mora & Loscertales, [13]. The empirically determined proportionality factor introduced by Fernández de la Mora, $f(\epsilon)$ is the slope of each data line in Figure 6-1.

Figure 6-2 shows three sets of data. The first set are experimental values for $f(\epsilon)$ from Fernández de la Mora and Loscertales, [13]. The second experimental set of data is from Chen & Pui, [4]. The third set of data are our computed values for $f(\epsilon)$ for the fluids of Table 6.1. The simulations show good agreement across the Fernández de la Mora experimental range. Chen and Pui suggest that the deviations they see at high permittivities $\epsilon > 80$ relative to Fernández de la Mora and Loscertales may be due to the fact that they

liquid	ϵ	K $[Si/m]$	$\gamma[N/m]$	$\rho[Kg/m^3]$	$\mu[Pa \cdot s]$	f(ϵ)(experimental)
Formamide-1	111	0.00100	0.058	1130	$3.80x10^{-3}$	18
Formamide-2	111	0.01000	0.058	1130	$3.80x10^{-3}$	18
Water	80	0.00215	0.073	998	$1.00x10^{-3}$	18
Benzyl Alcohol	13.1	0.00790	0.040	1040	$7.76x10^{-3}$	8.5
1-Octanol	10.34	0.00116	0.026	825	$1.06x10^{-2}$	7
Ethylene- Glycol	38.66	0.01690	0.048	1100	$21x10^{-3}$	17

Table 6.1: Properties of liquids used in the simulations from [13]

employed different doping agents to increase the conductivity of their solutions.

Only our simulation results for Ethylene Glycol show an important difference relative to experimental data. Three cases were run for various flow rates and in every case the total current was well described by expression 3.43. The value for $f(\epsilon)$ as computed was 13 instead of 17 as given by Fernández de la Mora. Previous studies by Gañán–Calvo and coworkers have produced current *(I)* vs flow rate *(Q)* scalings which are independent (or nearly so) of the liquid relative permittivity, [15, 18, 16, 17]. Gañán–Calvo's scaling (Eq. 3.47) suggests that $f(\epsilon) \approx \sqrt{\epsilon}$, i.e. cancelling out the effect of the relative permittivity (ϵ) in Eq. 3.45. It is noteworthy that a simple fit to our results of the form $f(\epsilon) \approx 2\sqrt{\epsilon}$ would be fairly accurate. This is in closer agreement to the scaling of Gañán-Calvo obtained with a hybrid experimental-numerical technique. In that work $f(\epsilon) = 2.6\sqrt{\epsilon}$, [16]. From equation 3.44, this indicates that the current has very weak dependence on the dielectric constant. We will later see from detailed computational results that the surface charge σ is in all cases within 20% of its equilibrium value $\epsilon_0 E_n^0$, even in the neck region. If the surface charge were everywhere fully relaxed, the dielectric constant ϵ would not play any role in the charge and fluid dynamics, and our results for the current appear to come close to this limit.

6.2 Sample results and parameter studies

The numerical results shown next were obtained using Formamide (K=0.005 Si/m) with a needle (capillary tube) radius of $h_0 = 10\mu m$, the collector was set at $L = 300\mu m$, and the applied voltage was computed from the startup formula (Eq. 3.15), $V = 1150V$. Two cases are shown in Figure 6-3 and 6-4; the first one (solid line) with $\eta = 2.2$ and the second

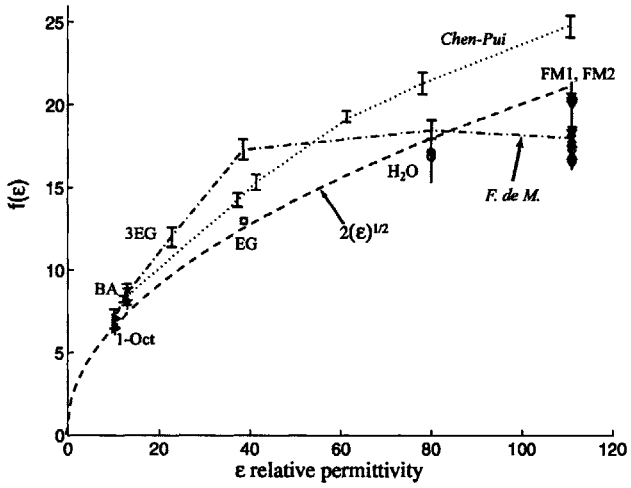

Figure 6-2: Comparison of experimental data from [13] and [4] to numerical results for various dielectric permittivities,(ϵ) versus non-dimensional slope $f = \zeta/\eta$

one (dash-dot line) at $\eta = 1.6$. The plots show the jet radius (h), mean velocity (u), surface charge density (σ), liquid potential (ϕ_l), normal outside Electric field (E_n^o) and the tangential electric field (E_t) as one progresses from the needle to the collector.

These results (Fig. 6-4) show that as $\eta \rightarrow 1$ the transition region becomes sharper with the cone semi-angle (α) approaching the Taylor cone value ($\alpha_T = 49.3^o$), and the emitted jet becoming thinner. For a lower η the jet average velocity (u) increases significantly while its profile remains almost constant as shown by the very low values of the shear velocity, u', (Eq. 4.6, the difference between the surface and centerline velocity). The surface charge density in the jet is seen to decrease as $\eta \rightarrow 1$. It can be seen in both cases that the potential in the cone region remains almost constant. This nearly equipotential condition at the cone is similar to the behavior found in Taylor cones. Once the cone becomes a jet the potential changes rapidly until it reaches zero at the collector. The electric field distribution reaches a maximum somewhere in the cone-jet transition region. In all cases it is observed that the normal component is stronger than the tangential one. Notice that the normal component of the E-field increases (although weakly) as η decreases. The tangential component shows the same behavior but the change is more dramatic. As the liquid progresses into the jet section the fields slowly decrease in magnitude. Finally, the last subplot shows the spatial distribution of the total current (I) and its components: the conduction I_{cd} and convection

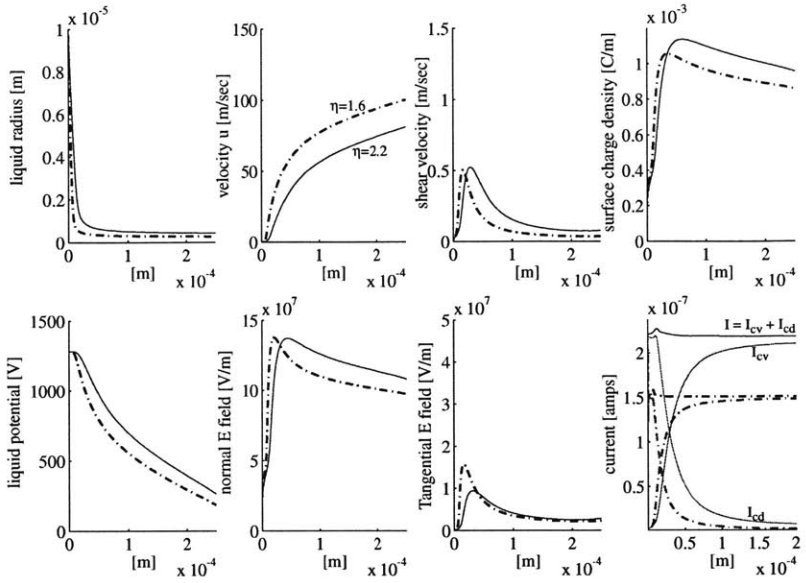

Figure 6-3: Simulation results for FM, $K = 0.005\ Si/m$ $h_0 = 10\ \mu m$, $L = 300\ \mu m$ and applied voltage $V = 1150\ V$. Two flow rates shown $\eta = 1.6$ (dash-dot line) and $\eta = 2.2$ (solid line)

current I_{cv}. The total current distribution ($I = I_{cd} + I_{cv}$) remains constant (i.e. dI/dz =0) which means that charge is conserved. Secondly, the total current decreases with η as expected (although not shown the computed current is in good agreement with the scales: Eq. 3.45 and Eq. 3.47). Thirdly, it can be seen that the conduction current dominates in the cone section and that the convection current dominates in the jet section. The point where both current components become equal is near the cone-jet transition, a few jet diameters into the jet.

6.2.1 Electrode distance effect

It should be noted that as the electrode is positioned further away the required starting voltage will increase as given by expression 3.15. As mentioned before this expression is only approximate and may be off by about 10% giving rise to slightly different total currents. The effect of varying the operating voltage on total current, at a given flow rate, is addressed in detail in section 6.2.7. One lesson learned from this set of numerical data is that in order to faithfully reproduce results the geometrical configuration of the needle-electrode needs to be well documented as well as the starting and operating voltages at which experimental

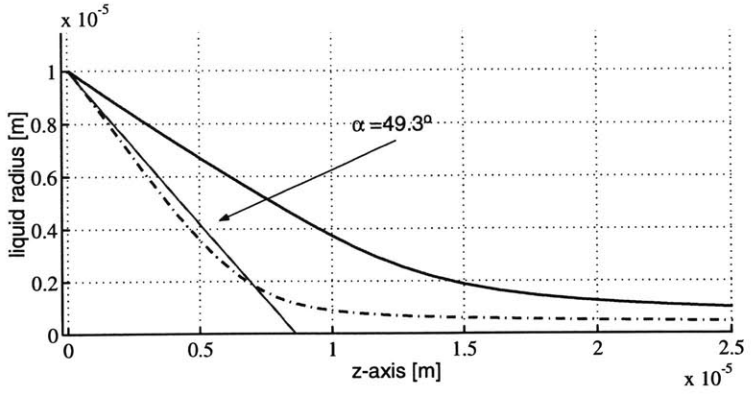

Figure 6-4: Close up of the cone-jet transition of figure 6-3, $K = 0.005\ Si/m$ $h_0 = 10\ \mu m$, $L = 300\ \mu m$ and applied voltage $V = 1150\ V$. Two flow rates shown $\eta = 1.6$ (dash-dot line) and $\eta = 2.2$ (solid line)

results are obtained.

Computations for various electrode distances ($L = 150, 300, 600 \mu m$) were carried out to characterize the effect of the ground electrode boundary condition (i.e. $\phi = 0$ at collector). The results in figure 6-5 show (a) that the sudden increase of the field intensity at the end of the computational domain is simply an artifact of the electrostatic ground boundary condition (b) that for lower conductivity liquids the residual conduction current may be affected by the electrode.

The minimum electrode distance was chosen based on the aspect ratio L/h_0 reported by [13]. In his case the aspect ratio was no less than 18. In our case the smallest aspect ratio was 15 up to, in some cases, 100.

A second numerical experiment is to fix the operating voltage to a given value and run the simulation for the three previously mentioned electrode distances. The results for this case are shown in figure 6-6. In this case the operating voltage was set to 1190 volts. In this case, however, the total currents are almost the same. This set of runs confirms that the spurious end effects at the electrode do not introduce significant errors in the important cone-jet transition region.

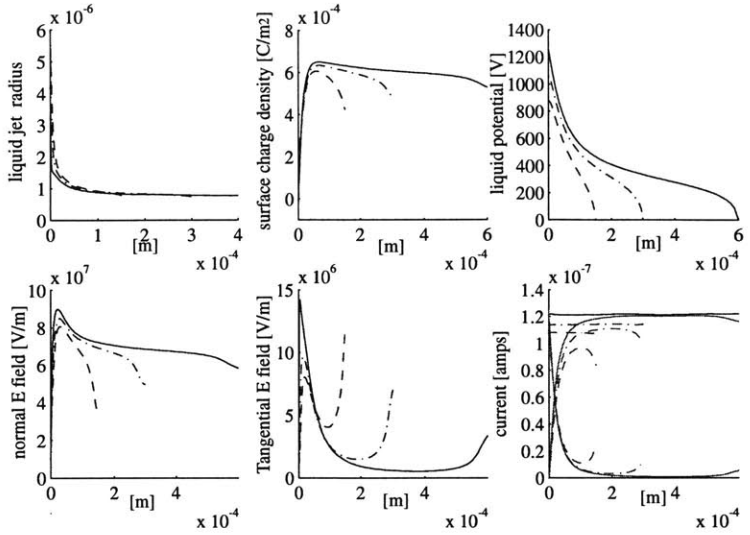

Figure 6-5: Simulation results for FM1, $h_0 = 6\mu m$, $\eta = 1.26$. Electrode distance is $L = 150\mu m$, $L = 300\mu m$, and $L = 600\mu m$, with applied voltages $V = 911V$, $V = 1050V$, and $V = 1188V$ respectively.

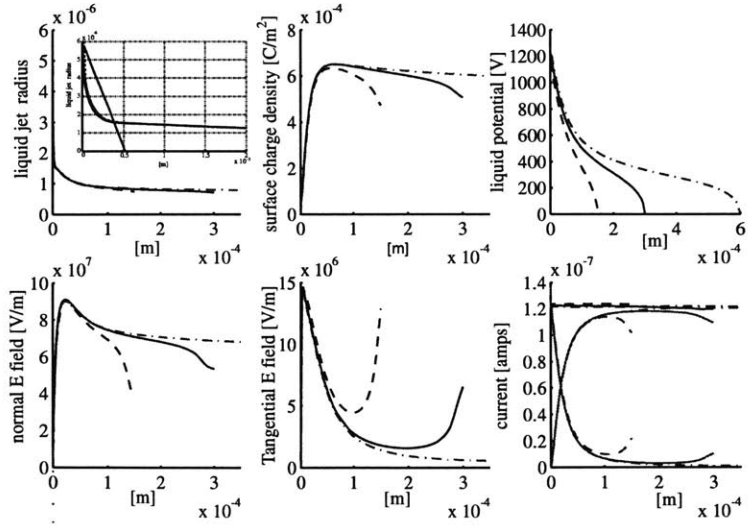

Figure 6-6: Simulation results for FM1, $h_0 = 6\mu m$, $\eta = 1.26$. Electrode distance is $L = 150\mu m$, $L = 300\mu m$, and $L = 600\mu m$, with applied voltages $V = 1190V$.

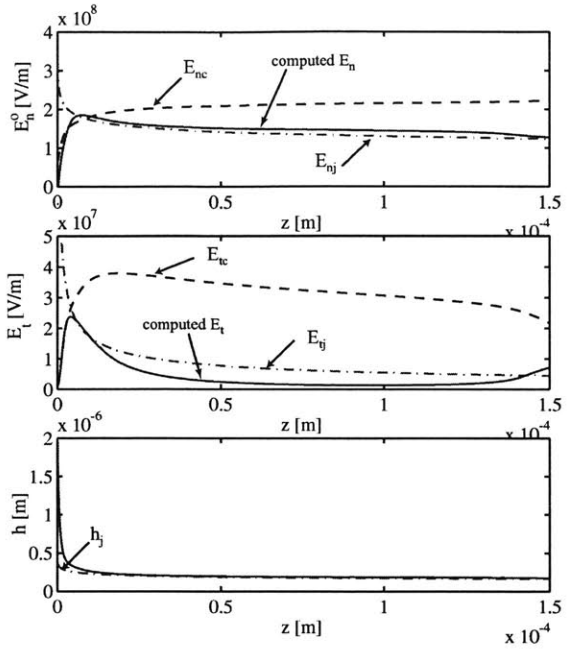

Figure 6-7: Comparison of analytical Estimates for Electric fields and jet radius to simulation data. Liquid data: FM2 at $\eta = 1.26$, $h_0 = 2\mu m$, $L = 150\mu m$

6.2.2 Analytical estimates compared to numerical results

In this section analytical estimates for the electrical fields of the jet and cone sections are presented. The present analysis assumes that the liquid charges are electrically relaxed; the numerical results show that this is true, with the possible exception of the cone-jet transition region.

Previous plots have shown that as the non-dimensional parameter $\eta \rightarrow 1$ the angle of the cone region tends towards the Taylor's angle (i.e. $\alpha_t = 49.29^0$) and the cone region tends to an equipotential. This similarity to the conditions upon which the Taylor's analysis is based suggests that the outside normal electric field, (E_n^o) can be approximated by an equilibrium between the electric and surface tension stresses, leading to

$$E_{nc}^o = \sqrt{\frac{2\gamma \cos \alpha}{\epsilon_0 h}} \tag{6.1}$$

Downstream from the transition zone most of the charge is convected on the surface allowing us to approximate the normal outside field by using Gauss law and noting that $dq/dx \approx I/u$, [21]

$$E^o_{nj} = \frac{hI}{2Q\epsilon_0}. \tag{6.2}$$

The tangential field in the cone region is estimated by using equation 4.22 and $I_{cd} = I - I_{cv}$ where I is given by 3.44 and I_{cv} by equation 4.21 for a fully relaxed cone (i.e. $\sigma = \epsilon_o E^o_n$). The result is

$$E_{tc} = \frac{f(\epsilon)}{\pi h^2}\left(\frac{\gamma Q}{\epsilon K}\right)^{1/2} - \frac{2Q}{\pi h^3 K}\left(\frac{2\gamma\epsilon_o}{h}\right)^{1/2} \tag{6.3}$$

The tangential field in the jet section is dominated by the charge from the cone region,. A first approximation to the tangential field distribution can be computed by evaluating the Taylor's cone field solution (cone with apex semiangle $\alpha_T = 49.3^o$ and no jet at $\theta = \pi$, i.e. at the *z-axis*), [15, 6].

$$C_T = \frac{1}{\sqrt{2\tan\alpha_T}}\frac{\mathcal{Q}_{1/2}(\cos\pi)}{\mathcal{Q}'_{1/2}(\cos\alpha_T)} = 0.67 \tag{6.4}$$

$$E_{tj} = C_T\left(\frac{\gamma}{\epsilon_o z}\right)^{1/2} \tag{6.5}$$

where $\mathcal{Q}_{1/2}$ is the Legendre function of the second kind, with degree 1/2 and order 0; while $\mathcal{Q}'_{1/2}$ is its derivative with respect to θ.

Finally the jet radius dependency given by Gañán-Calvo is a function of order $h \propto O(Q^{3/4}I^{-1/4}z^{-1/8})$, [15]. This estimate assumes that the jet is fully relaxed ($\sigma = \epsilon_0 E^o_n$) and that the normal electric field is well approximated by equation 6.2. The main assumption for this estimate is that in the jet region the momentum balance is given by :

$$\frac{1}{2}\frac{du^2}{dz} = \frac{2\sigma E_t}{\rho h} \tag{6.6}$$

which after integration gives the form:

$$h_j \simeq \frac{1}{(2\pi^2 C_T)^{1/4}}\left(\frac{\rho^2\epsilon_0}{\gamma}\right)^{1/8}\frac{Q^{3/4}}{I^{1/4}z^{1/8}}. \tag{6.7}$$

A comparison between these estimates and simulation data can be seen in Figure 6-7. The simulation data (solid line) shown is for FM2 at $\eta = 1.26$. It can be seen that the estimates give a reasonable approximation to the numerically computed results. An

exception is E_{tj}, which is overestimated by (6.5). Clearly, the jet charges do provide a fair amount of space charge and reduce the axial fields due to the cone alone.

Previously, in figure 6-3 it was observed that as $\eta \rightarrow 1$ the surface charge density decreased. Using the analytical estimates, this behavior can be explained qualitatively by noting that in the jet $I_{cv} \approx I$ and therefore $\sigma \approx \pi h I_{cv}/Q$ where *(h)* is approximated by equation 6.7. This shows that if $h \propto (Q^{5/8})$, and $I \propto (Q^{1/2})$(see equation 3.44), then the surface charge density, $\sigma \propto Q^{1/8} \propto \eta^{1/4}$. Notice that in terms of the spatial variation of the surface charge density $\sigma \approx \pi h I_{cv}/Q$ where only h is function of z, (equation 6.7). The surface charge density then can be seen to vary approximately as $\sigma \propto z^{-1/8}$. In the following sections these analytical approximations will be used to get a better grasp of the underlying physical phenomena observed in various numerical parameter studies.

6.2.3 Energy Conservation

We calculate the power input of the system by multiplying the extraction voltage by the total resulting current. This power is used for accelerating the flow, setting up the cone-jet shape (surface formation), and some of it is dissipated by viscous stresses, and Joule heating. In our case we present the energy analysis in terms of voltage $V = Power/I$ and energy percentage (V/V_{st}, V_{st} from Eq. 3.15). The sum of all the voltage contributions should ideally be the original extraction voltage (V_{st}). Detailed numerical results for Formamide ($K = 0.01\ Si/m$) vs η are shown in figure 6-8. In order of importance the different energy contributions are given below. The acceleration voltage (kinetic energy) is given

$$V_k = \frac{1}{2}\frac{\rho Q}{I} u|_{z=L}^2 \tag{6.8}$$

where u is velocity at $z = L$. This voltage is used to accelerate the fluid to its final velocity. The second contribution to the voltage is due to Joule heating. This voltage is calculated as

$$V_\Omega = \frac{K}{I}\int_0^L \frac{2\pi (hE_t)^2}{1+\cos(\alpha)} dz. \tag{6.9}$$

The third contribution is the energy needed to overcome surface tension and set the shape of the liquid jet. The expression for this voltage is:

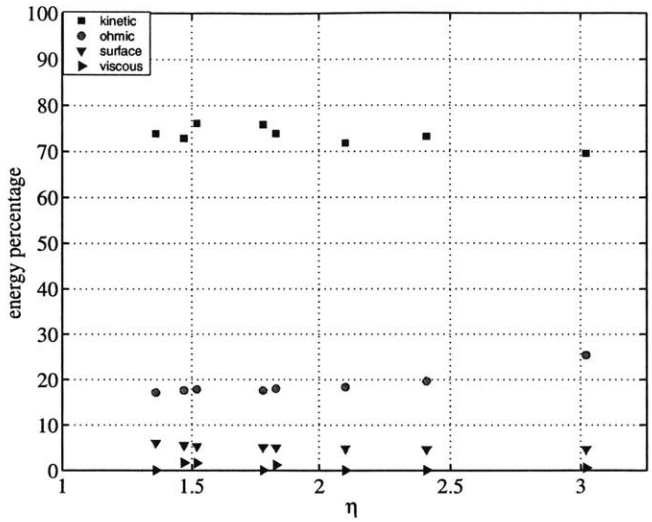

Figure 6-8: Energy breakdown (percentages) vs η for Formamide, $K = 0.01\ Si/m$

$$V_\gamma = \frac{\gamma\pi(hu)|_{z=L}}{I}. \tag{6.10}$$

The remaining contribution is that due to viscous dissipation given by:

$$V_\mu = \frac{3\pi\mu}{I}\int_0^L \left(h\frac{\partial u}{\partial z}\right)^2 dz. \tag{6.11}$$

Adding up all the different contributions the applied potential should be recovered. In reality a small percentage, in the order of 1- 3% of the applied potential is unaccounted for. This "lost" energy may be due to unaccounted smaller losses.

Figure 6-8 presents the voltage contributions (normalized by the starting voltage ,V_{st}) vs η for a formamide solution (FM2). In general the dominating contributions (for the liquids in this study) are the kinetic energy and the ohmic heating. The surface formation energy (surface tension term) varies between 5-10% and viscous losses amount to 1-3%. Figure 6-8 shows that as η increases the kinetic fraction decreases while the ohmic fraction increases. The contributions due to surface formation (surface tension related) remain almost constant, which makes sense since the basic shape of the cone and jet structure will not change dramatically with η.

Numerical results for the ohmic dissipation fraction V_Ω/V (formula 6.9) vs η for various

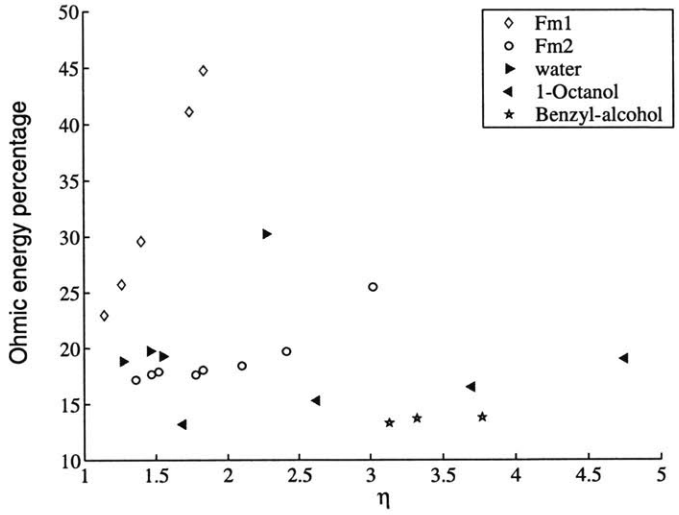

Figure 6-9: η vs Ohmic dissipation fraction (V_Ω/V) for multiple liquids.

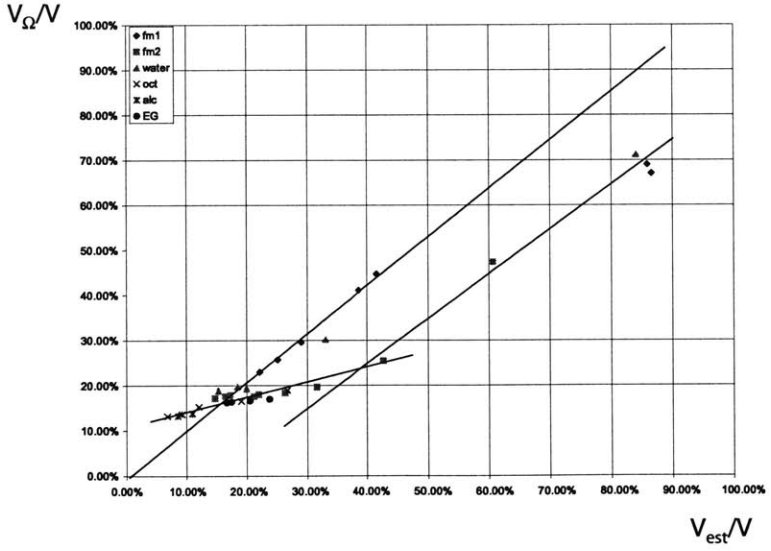

Figure 6-10: Plot of Ohmic dissipation for various liquids. x-axis estimate based on equation 6.12 vs simulation data

liquids are shown in figure 6-9. The numerical results show that as η increases the ohmic dissipation fraction increases as well. The trend shown in figure 6-9 is that the liquids with the slowest electrical relaxation time ($\epsilon\epsilon_0/K$) present higher levels of ohmic dissipation. This can be seen by noticing that in figure 6-9 FM1 has the slowest relaxation time ($t_e = 0.98\mu s$), and highest ohmic dissipation, vs Benzyl-alcohol which has the fastest relaxation time (66 times faster than FM1), and lowest ohmic dissipation.

A normalized estimate for the energy dissipated as ohmic heating can be obtained by integrating expression 6.9 divided by the total applied voltage 3.15. The integration is carried out using estimates 6.5, and 6.7 from the beginning of the jet region $z_0 = FR_d$ (where it is assumed $F \approx 2.3$) to $z \to \infty$

$$\frac{V_\Omega}{V} = \frac{2\epsilon}{F^{1/4}} \left(\frac{C_T}{f(\epsilon)}\right)^{3/2} \sqrt{\frac{R_d}{h_0}} \frac{\eta^{2/3}}{\ln(\frac{4L}{h_0})} \tag{6.12}$$

A comparison of the percentage of energy dissipated as ohmic heating between simulation results and equation 6.12 is shown in Figure 6.2.3. The plot shows that expression 6.12 captures the right trends but is not a very accurate estimate. Reasons for this inaccuracy may be traced back to the uncertainty of the transition point z_0 and also to the fact that expression 6.5 neglects the effects of charges on the jet.

6.2.4 Cone-Jet transition length scales

Previous research has aimed to identify the length scale that best describes the transition from the cone to the jet region. Fernández de la Mora suggested that the jet could scale with the electrical relaxation length r^* (3.16), or the inertial length R_d (3.19). Other studies by Gañán-Calvo led to the introduction of another length scale, R_g (3.26), [15].

In this case the transition has been defined as the point where the convection current equals the conduction current. Previous work by Gañán–Calvo [15] and numerical results by Higuera [28] have shown that $I_{cv} = I_{cd}$ occurs somewhat downstream of the point of maximum curvature. Nonetheless, choosing the crossover point (R_x) results in a non-ambiguous definition of the cone-jet transition and it serves as a lower bound of the transition radius.

Numerical results for various liquids were used to further investigate how the transition region relates to R_d, r^*, and R_g. The results are shown in figure 6-11 where the plots show on the horizontal axis the length scales R_d (top), r^* (center) and, R_g (bottom) in

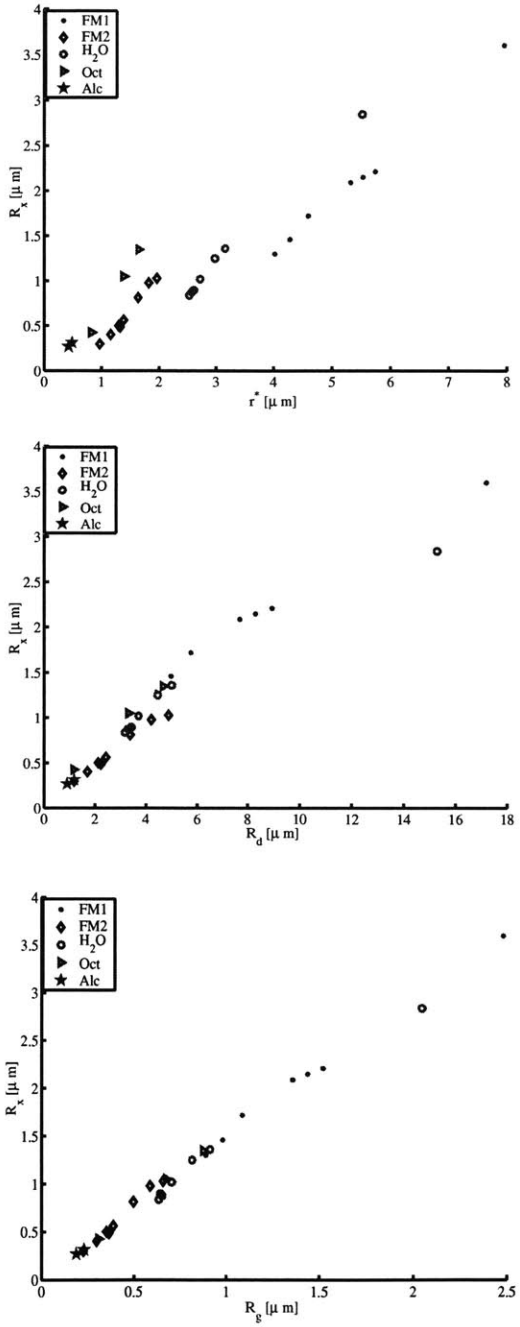

Figure 6-11: Cone to jet transition radius (R_x) vs proposed length scales. top r^* (Eq. 3.16), center R_d (Eq. 3.19) , bottom R_g

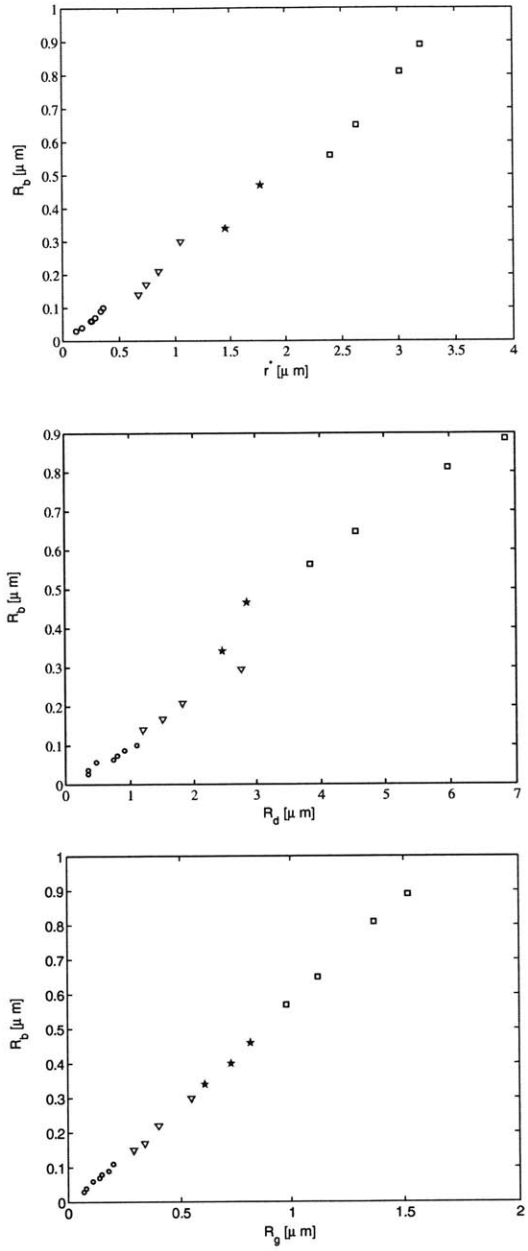

Figure 6-12: Breakup radius for TBP (various conductivities) (R_b) vs proposed length scales. top r^* (Eq. 3.16), center R_d (Eq. 3.19) , bottom R_g. Experimental data reproduced from Gamero and Hruby [22].

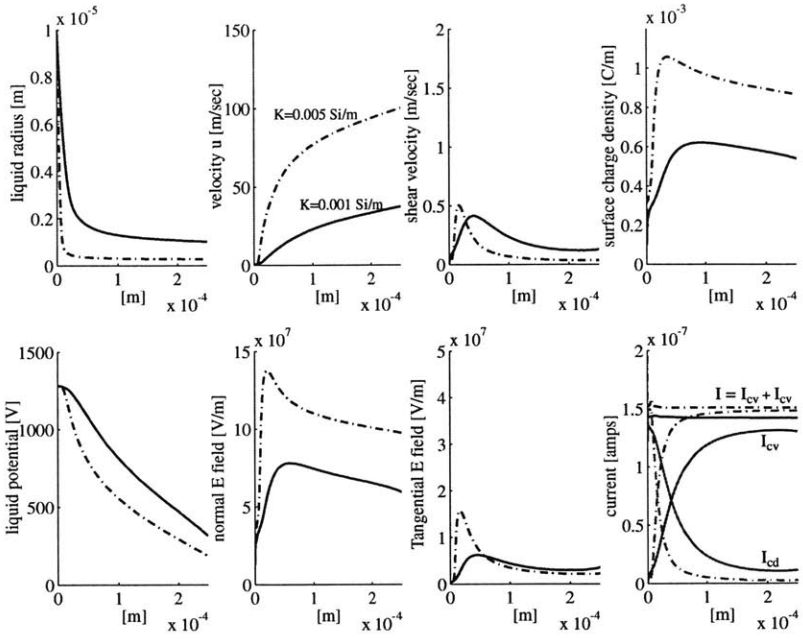

Figure 6-13: Formamide data $\eta = 1.6$, $h_0 = 10\ \mu m$, $L = 300\ \mu m$ and applied voltage $V = 1150\ V$. Two conductivities shown: Solid line K=0.001 Si/m, and dash-dot line K=0.005 Si/m

μm and on the vertical axis the crossover radius R_x also in μm. It can be seen from the plots that for the case of R_g most of the data collapse on one line. A linear regression for this case gives $R^2 = 0.9933$ with a slope of 1.45. Comparing these results to those obtained experimentally by Gamero and Hruby [22] we show the same qualitative behavior for r^*, R_d, and R_g vs their calculated breakup radius R_b (see figure 6-12). Gamero and Hruby report that $R_b \approx 0.6R_g$ (coinciding with the slope value given by Gañán–Calvo [15]) whereas for our numerical transition results indicate $R_x \approx 1.45R_g$. From the experimental data the better correlation to the breakup radius (R_b) is given by R_g, [22]. The same behavior is confirmed from our numerical results for the transition radius (R_x).

6.2.5 Conductivity effects

A set of results is shown in figure 6-13 for two conductivities, namely Formamide $K = 0.005\ Si/m$ and $K = 0.001\ Si/m$. These results were obtained with $\eta = 1.6$, $h_0 = 10\ \mu m$, $L = 300\ \mu m$ and applied voltage $V = 1150\ V$. Note the important differences between the two cases even though their non-dimensional slope $f(\epsilon)$ (and hence current) is about the

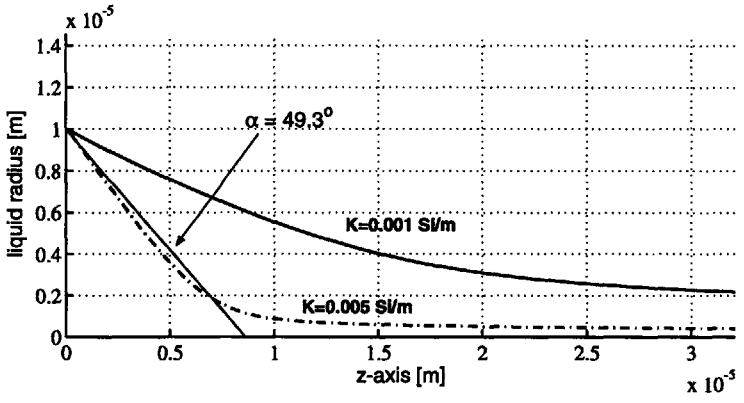

Figure 6-14: Close up of the cone-jet transition of figure 6-13. Formamide data $\eta = 1.6$, $h_0 = 10\ \mu m$, $L = 300\ \mu m$ and applied voltage $V = 1150\ V$. Two conductivities shown: Solid line K=0.001 Si/m, and dash-dot line K=0.005 Si/m

same (5% difference). The cases were run at the same $\eta = 1.6$ and both cases coincide with the current predicted by Fernández de la Mora from equation 3.44. It should be pointed out that in order to keep the same η for the two liquids the flow rate was decreased by an order of magnitude (i.e. $\eta \propto \sqrt{KQ}$) for the $K = 0.005\ Si/m$ data. Figure 6-13 shows an important change on the residual conduction current I_{cd} in the jet region as a function of liquid conductivity. The ratio of conduction current to total current in the jet can be estimated by :

$$\frac{I_{cd}}{I} \approx \frac{KE_t h^2}{I} \tag{6.13}$$

approximating the jet tangential field by 6.5 and the jet radius by 6.7 we obtain :

$$\frac{I_{cd}}{I} \approx \sqrt{\frac{C_T}{2}} \left(\frac{\epsilon}{f(\epsilon)}\right)^{3/2} \left[\frac{\gamma^{1/4}\epsilon_0^{1/2}}{K^{1/2}\rho^{1/4}}\right] \frac{\eta^{3/2}}{z^{3/4}} \tag{6.14}$$

This estimate shows the residual conduction current fraction is inversely proportional to square root of the conductivity, which corresponds to the trend shown in the numerical results of figure 6-13. Estimates using expression 6.14 give a conduction fraction of 0.071 (numerical result 0.077) for the $K = 0.001 Si/m$ solution and 0.032 for the $K = 0.005\ Si/m$ solution (numerical results give 0.018) at $z = 250\ \mu m$. Equation 6.14 also indicates the current fraction dependence to the liquid relative permittivity $I_{cd}/I \approx \epsilon^{3/4}$ (where $f(\epsilon) \approx$

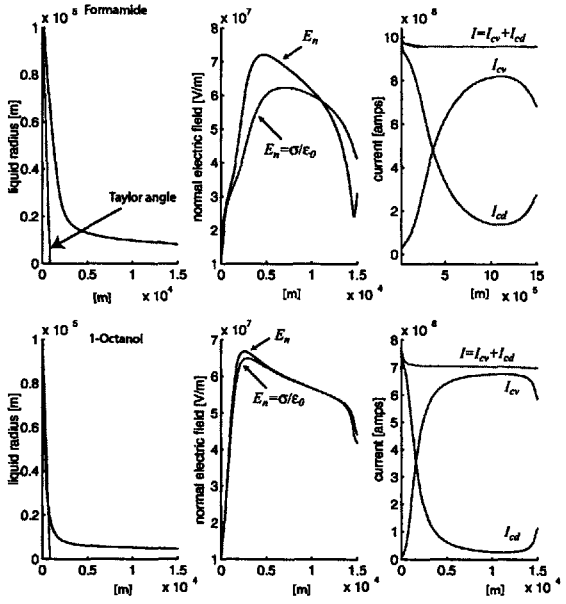

Figure 6-15: Formamide-1 ($\epsilon = 111$), and Octanol data ($\epsilon = 10.34$) . Both cases with $\eta = 1.96$

$\sqrt{\epsilon}$). We have verified numerically that this fraction is indeed higher for FM ($\epsilon = 111$) than 1-Octanol ($\epsilon = 10.34$), see figure 6-15.

6.2.6 Dielectric permittivity effects

Figure 6-2 shows two distinct behaviors, one for high dielectric permittivities ($\epsilon \geq 40$) and the second for the lower permittivities. Two runs were conducted for Formamide-1 and 1-Octanol both fluids at different extremes of the Fernández de la Mora's experimental range. The results for the final distributions of jet shape, normal electrical field, charge relaxation and current are shown in Figure 6-15. One of the important things to notice while comparing the jet shape for both fluids is that for the Octanol case the cone angle almost coincides with Taylor's cone angle for a conducting liquid ($\alpha = 49.3^o$). In this case the cone region becomes almost equipotential thus approximating Taylor's exact solution. The degree of charge relaxation (i.e. $En \rightarrow \sigma/\epsilon_0$) can be seen to have a strong correlation with the remaining fraction of conduction current in the jet region. The residual conduction current fraction is smaller for the 1-Octanol case (almost completely relaxed) as opposed to the Formamide-1 case. The importance of the relative permittivity for the conduction current fraction

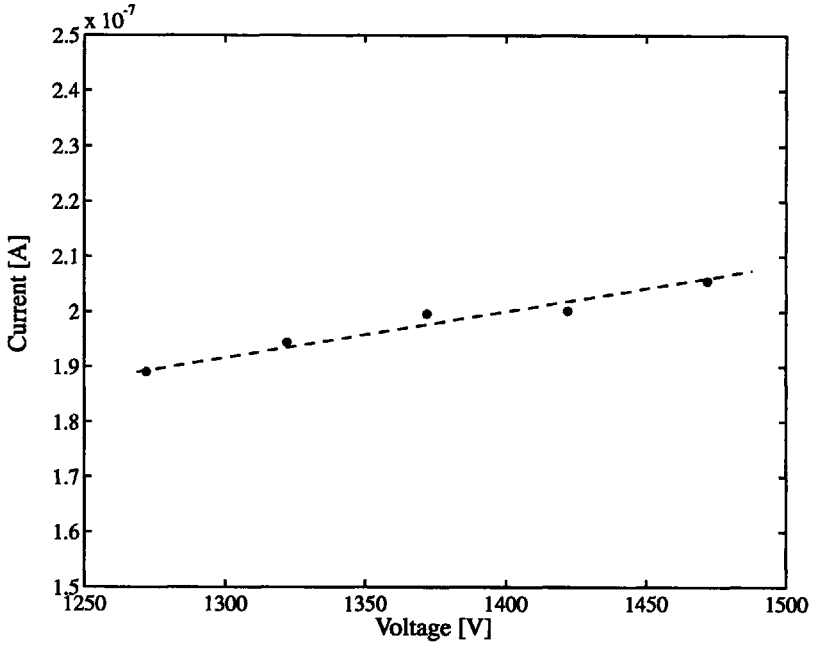

Figure 6-16: Total current ($I = I_{cd} + I_{cv}$) vs Voltage for water, $\eta = 1.55$, $h_0 = 10\mu m, L = 300\mu m$, original starting voltage $V = 1372\ V$.

can be seen from equation 6.14. The conduction current fraction is directly proportional to $(\epsilon/f(\epsilon))^{3/2}$ which is larger for Formamide-1 than for 1-Octanol. Expression 6.14 gives a conduction current fraction of 0.19 for FM1 (the computation shows $I_{cd}/I \approx 0.19$ at $z = 1x10^{-4}m$) and of 0.04 for 1-Octanol (computation shows $I_{cd}/I \approx 0.019$at $z = 1x10^{-4}m$).

6.2.7 Voltage parameter study

The simple theories based on a cone with Taylor's angle appear to indicate that the single-cone regime is attained for a given liquid and flow rate only at a particular voltage *(V)*, somewhat lower than the starting voltage given by 3.15. Experimentally however, it is known that the single cone regime can be maintained within a narrow voltage window for a given configuration. The voltage window usually spans between 10% below the minimum extraction voltage and almost 40% above. A parameter study has been carried out to explore the effect of increasing the extraction voltage. The liquid used was water, $h_0 = 10\ \mu m$ and $L = 300\mu m$. All runs were carried out at $\eta = 1.55$.

The current plots can be seen in figure 6-16. The reference starting voltage (V=1372 V)

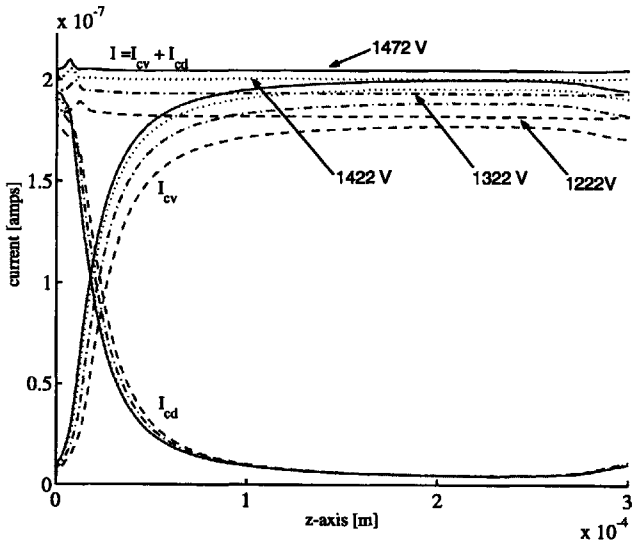

Figure 6-17: Convection (I_{cv}) and Conduction (I_{cd}) current vs Voltage behavior for water. $\eta = 1.55$, $h_0 = 10\mu m$, and $L = 300\mu m$. Reference starting voltage 1372 V

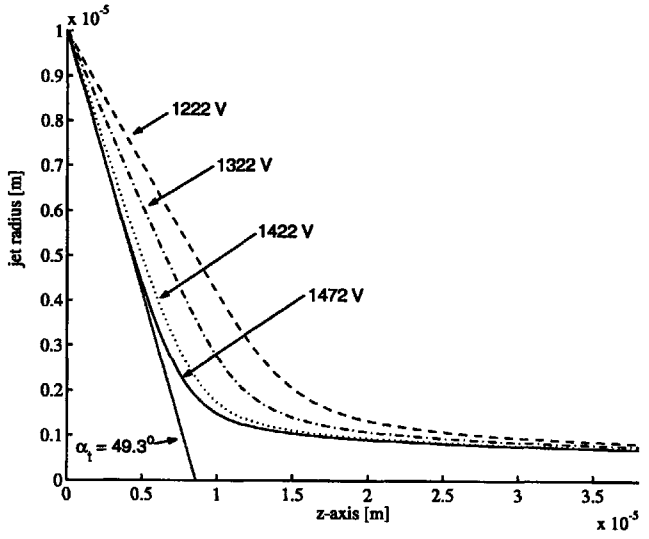

Figure 6-18: Effect on jet shape at different voltages. Liquid: Water at $\eta = 1.55$, $h_0 = 10\mu m$, and $L = 300\mu m$. Reference starting voltage 1372 V

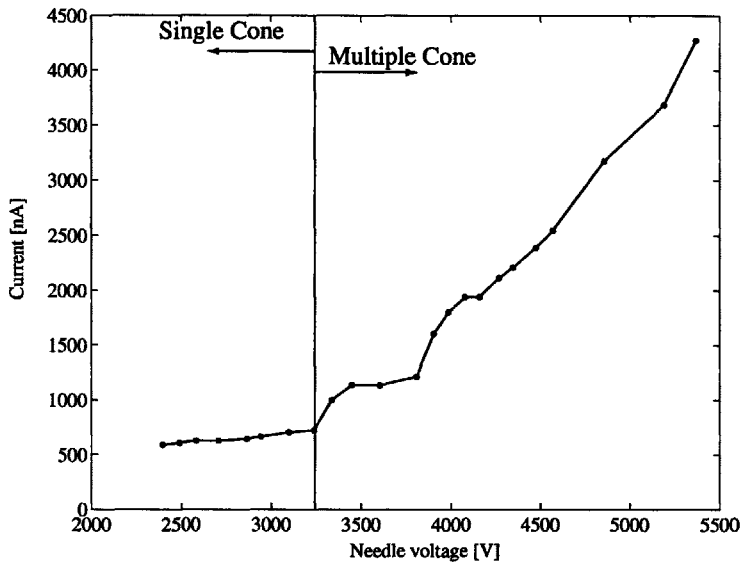

Figure 6-19: Experimental data from Gamero-Castaño [52] for glycerol. Needle $h_0 = 50\mu m$, $L = 4mm$ and fixed flow rate $Q_0 = 12.5ml/s$). Notice the change from single cone-jet mode to the multiple cone-jet mode (highly stressed regime)

was calculated using equation 3.15. Results show that the overall current does have a slight (approximately linear) dependence on the applied voltage. This almost linear dependence to the voltage has also been numerically calculated by Hartman *et al* for ethylene glycol solutions, [27].

The convection current I_{cv} (see figure 6-17) shows the strongest variation, increasing with applied voltage V, whereas the conduction current (I_{cd}) shows no important changes. A related effect of increasing the voltage is a deformation of the liquid cone surface. Figure 6-18 shows this effect on the cone-jet shape for the voltages shown in figure 6-16. A qualitative explanation for this effect is that the higher voltage augments the electric stress which in turn is balanced by the surface tension stress ($\delta P \propto \gamma/R$), (although a reduction in the liquid pressure is also present). The surface stress equilibrium is thus maintained by a steepening of the cone angle (i.e. reduction of the liquid curvature), see figure 6-18. Similar trends of the cone semi–angle vs applied voltage have been obtained before for the case of conducting liquid menisci subjected to an applied voltage, [62] [55]

Experimental data from Gamero-Castaño [52] for glycerol (needle $h_0 = 50\mu m$, $L = 4mm$ and fixed flow rate $Q_0 = 12.5ml/s$) also showed an initial linear behavior from the onset

voltage 2400 V to 3230 V. Pictures taken during the tests also showed a shrinking of the cone as the voltage increased. A sudden current increase was measured beyond this voltage and observations confirmed the bifurcation of the single cone-jet to a multi cone-jet configuration (highly stressed regime).

6.3 Summary

Numerical results for multiple liquids and flow rates have been presented. The predicted current and non-dimensional slope compare quite well with published experimental data of Fernández de la Mora & Loscertales [13]. Our results reproduce the effect of the dielectric permittivity on the non-dimensional current vs. square root of flow slope for different liquids as seen in the above mentioned paper. Further examination of our results shows that (except near the minimum flow) there still exists a finite conduction current in the jet downstream of the transition region. The conduction current fraction has been shown to be related to the degree of electrical relaxation that the liquid achieves, although no causal link has been identified.

Chapter 7

Results for mixed ion–droplet regime

In this chapter initial results for field enhanced ion evaporation are presented. As mentioned in chapter 3 ion evaporation becomes an important phenomenon only for high conductivity solutions ($K \approx 1$ Si/m). The maximum conductivity for which converged solutions have been obtained is K=0.07 Si/m which is well below the expected range. Following, the work of Higuera [29] the first approach has been to lower the solvation energy of the ions. The first set of results are shown in subsection 7.2. The concern with this approach is that the results are qualitative at best. There is no guarantee that this modification is physically sound or that it accurately predicts the mixed ion-drop regime.

7.1 Expected results

The results obtained with the ion evaporation model are shown next. The expected behavior is that seen experimentally by Gamero,[20, 47], see figure 7-1. The x-axis has the non–dimensional flow rate η and the y-axis shows the emitted current, I_{tot}, with the arrow pointing in the direction of increasing liquid conductivity, K. Notice that for the higher conductivities ($K \approx 1\ Si/m$) as the flow rate (η) decreases the emitted current (I_{tot}) reaches a minimum and then starts to increase again. It is in these cases when the current due to evaporated ions becomes of the order of the droplet current. The contribution of the accumulated ion current (I_i) to the total current (I_{tot}) as function of flow rate (Q) is easier to appreciate in figure 7-2 from Lozano, again for a formamide doped with NaI

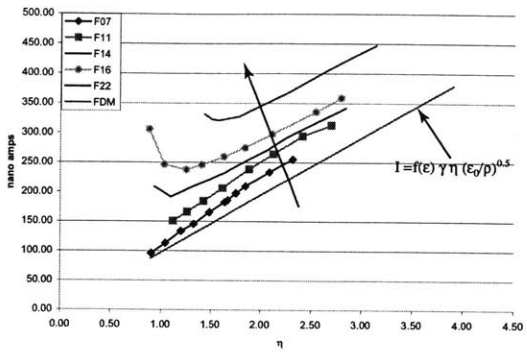

Figure 7-1: Fig. 11 from Gamero [20]. Current vs non–dimensional flow rate for formamide solutions of various conductivities. The arrow points to increasing conductivity. The minimum is associated with onset of ion evaporation. F07 (K=0.71 Si/m) through F22 (K= 2.20 Si/m)

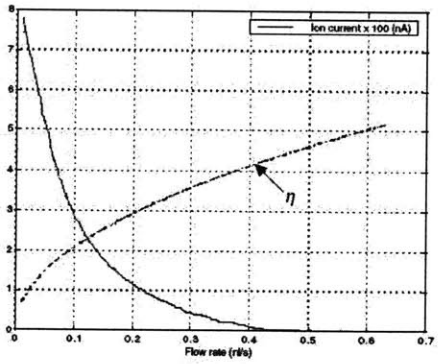

Figure 5.4.2. Ion current vs. flow rate. formamide + NaI. The dashed line corresponds to the value of the non-dimensional flow parameter η

Figure 7-2: Ion current vs flow rate. Formamide + NaI, dashed line corresponds to η, Figure 5.4.2, from Lozano, [47]

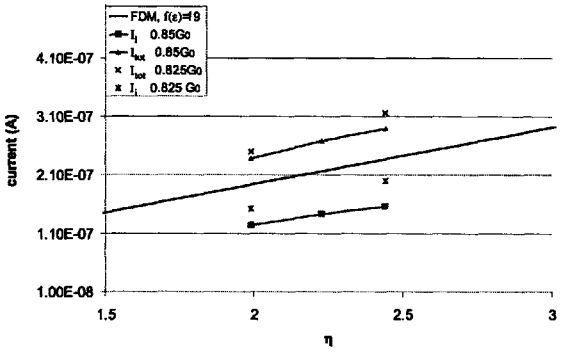

Figure 7-3: Current vs non–dimensional flow rate plot for formamide (K=0.01 Si/m). $h_0 = 2\mu m$. Two sets of results $G_0 = 0.85\ eV$ and $0.825eV$, I_{tot} is the total emitted current, I_i is the accumulated ion current. FDM is the predicted current for the pure droplet regime, Eq. 3.45.

($K = 2.9\ Si/m$). Note that the ion current is essentially zero with decreasing flow rate until a threshold value is reached and then a very fast growth is seen, [47].

7.2 Modified solvation energies

Due to the numerical stiffness associated with running simulations at high conductivities (and consequently low flow rates) we have been forced to limit ourselves to formamide solutions with $K = 0.01\ Si/m$. A consequence of the low conductivity of our simulation is that the maximum E-field obtained is roughly one order of magnitude below the necessary 1 V/nm for field evaporation. For this reason our first approach to the ion evaporation problem has been to lower the energy (G_0) required to extract the ions from the liquid surface. Preliminary results for these calculations are shown next.

Our initial results with a modified solvation energy predict, as expected, a higher total current than that for the pure droplet regime. Notice however, that the ion current is an increasing function of the flow rate which is at odds with the experimental evidence. Figure 7-3 has the non-dimensional flow rate η on the x-axis and the total emitted current I_{tot} as y-axis. Two sets of numerical results are shown, these correspond to two solvation energies: $G_0 = 0.85\ eV$ and $0.825\ eV$ respectively. For each set of results the total current (I_{tot}) and ion current (I_i) are plotted as function of η. For reference the emitted current predicted by Fernández de la Mora and Loscertales for the pure droplet case is included

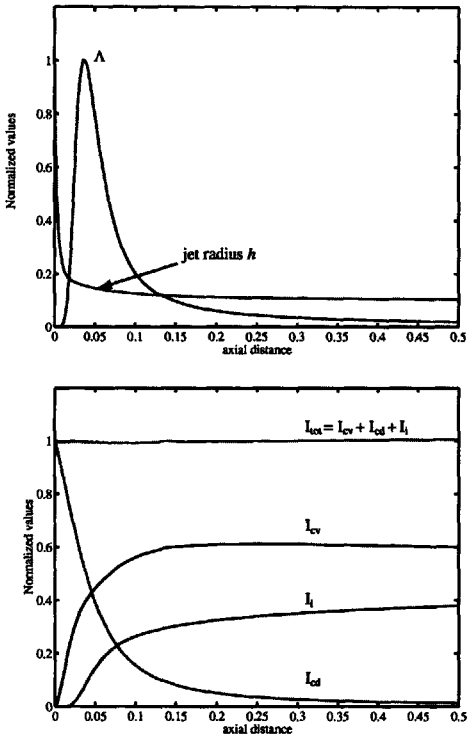

Figure 7-4: Top plot : Depiction of jet radius (h), and ion current per unit length [3.57] (Λ) vs axial position. Bottom plot: Electric currents vs axial position. I_{cv} jet convection current (4.21), I_{cd} jet conduction current (4.22), I_i accumulated ion current (3.58), I_{tot} total current

(FDM in the figure, Eq. 3.45). Notice that although the total current for both ion evaporation cases is higher than that for the pure droplet regime (in accordance with Gamero's data), the observed ion current is still an important function of flow rate, which is at odds with the results of Lozano, (Fig. 7-2, [47]).

In any case, some, important things can be learned from these results. From figure 7-4 we see the comparison of the jet shape along with the ion emitted current per unit length (Λ). These results have been normalized ($y* = y(z)/max(y)$) for each variable, and are only meant to show the relative behavior of the important variables. The maximum as one would expect is located a bit downstream from the transition region (coinciding with the maximum E_n field). Other interesting effects can be seen from analyzing the current profile of the jet. The conduction current (I_{cd}) is still dominant in the cone section of the jet with negligible contributions from the convection (I_{cv}) and accumulated ion current

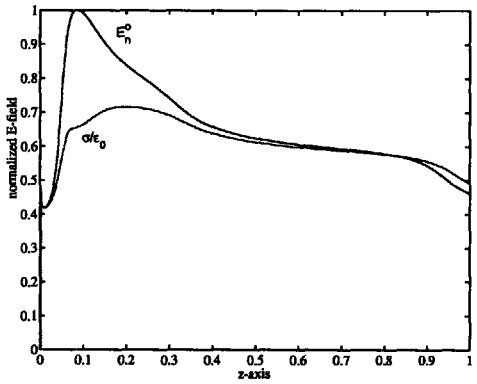

Figure 7-5: Comparison of surface charge behavior for droplets and mixed-regime. Compare to pure droplet cases, 6-13

(I_i). As the liquid traverses from the cone to the jet section the conduction current almost disappears and now most of the current is transported by the convection current and the ion current. The convection and ion current compete with each other since both draw from the available free surface charge (σ). If the ion evaporation is strong enough the ion current may dominate and overcome the convection current. A second effect is that the surface charge may develop a local depression at the location of maximum E-field (co-located with the maximum evaporation section), see figure 7-5. The depression is created by the continuous loss of ions (free charge) which cannot be replenished fast enough by the bulk of the liquid. In any case, although these effects may be qualitatively correct they should be taken with a grain of salt.

Another issue to which attention should be drawn too is that temperature may become significant near (but not necessarily at) the maximum evaporation location. A calculation of ohmic heating along the jet (see section 6.2.3) reveals that the point of maximum dissipation is not co-located with the maximum ion evaporation point (and E-field), 7-6. This effect may modify the ion evaporation region since the liquid temperature (T) does have an effect on ion desorption. A heat transfer model of the temperature distribution along the jet, is however, beyond the scope of this work. Nonetheless, it does mark a point to be considered for future research.

A second attempt with the reduced solvation energy, but now following the technique proposed by Higuera is presented next, [29]. Again, one can only expect to draw qualitative

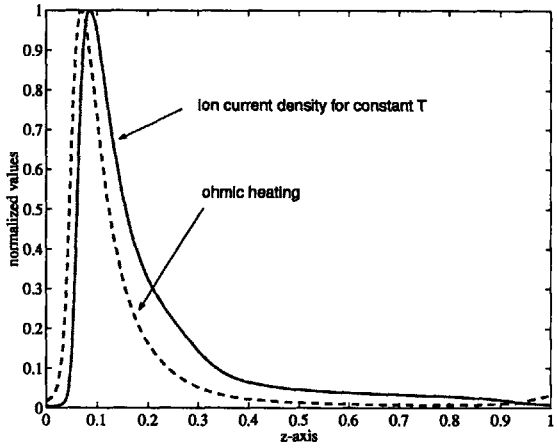

Figure 7-6: Normalized comparison of the ion current density (continuous line) and ohmic heating distribution $O = 2\pi K(E_t h)^2/(1+\cos\alpha)$, see section 6.2.3

conclusions from these simulations. The ion current density equation (3.59) is rewritten as:

$$j_i = \sigma \frac{K_B T}{2\pi\hbar} \exp\left(A^*[(\hat{E}_p)^{1/2} - (\hat{E}^*)^{1/2}]\right) \tag{7.1}$$

where $\hat{E}_p = E_p/E_0$ is the nondimensional form of the normal electric field modified to account for space charge effects (E_p), (Eq. 3.62. E^* is defined by equation 3.61 and nondimensionalized as $\hat{E}^* = E^*/E_0$. The sensitivity parameter A^* is then:

$$A^* = \left(\frac{q^3 c E_0}{4\pi\epsilon_0}\right)^{1/2} \frac{1}{K_B T} \tag{7.2}$$

where the only new addition is a sensitivity constant c. There are various options for the scaling E-field as described by Gamero,[21]. In this case we choose, for convenience:

$$E_0 = \left(\frac{\gamma}{\epsilon_0 R_d}\right)^{1/2} \tag{7.3}$$

where R_d has been previously defined as the inertial length scale, Eq. 3.19. As mentioned before (see chapter 3) ion evaporation becomes important once the maximum electric field approaches $E_{max} = 1\ V/nm$, which for formamide ($\eta = 1$) requires a conductivity is $K = 1.3\ Si/m$. The sensitivity parameter for a formamide solution under experimental conditions (at room temperature (T = 300K), $c = 1$, and for an assumed $E_0 = 1\ V/nm$) is $A^* = 46.34$. Higuera quotes a value for A^* of 112 for a formamide solution with $K = 1\ Si/m$,

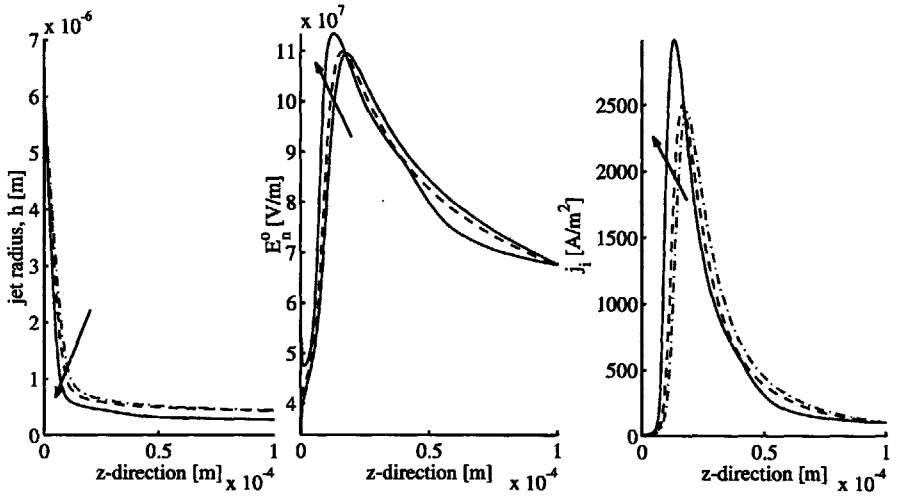

Figure 7-7: Results for ion evaporation using Higuera's method. Results for FM2 ($K = 0.01\ Si/m$), $G_0 = 0.8\ eV$, $c = 0.85$ for Na+ solvated ions. Plots show spatial evolution relative to z-axis; left:jet radius, center: Normal external E-field, right: evaporated ion current density. Arrows point towards lower flow rates $(Q = 4, 3, 2) \times 10^{-11} m^3/s$

but with a calculated $E_0 = 7\ V/nm$ which may be a bit high, [29]. The discrepancy with Higuera is due to the use of an alternative formula to estimate the maximum E-field.

In this case, the solvation energy G_0 is lowered as done before but now the A^* parameter is modified by a constant c. Basically, the factor c can be thought of as a modification of the local temperature: $T_m = T/\sqrt{c} > T$. This could be realistic depending on thermal balances. Again, these modifications can only hope to give us a qualitative feel for the physics at work.

Simulations with this approach, have been performed for a formamide solution with a conductivity ($K = 0.01\ Si/m$), emanating from a conducting needle of inner radius $h_0 = 6\mu m$, operating at a voltage of $V = 950\ V$ with the ground electrode set at a distance of $L = 150\mu m$. The solvation energy has been lowered to $G_0 = 0.8\ eV$ (from the original 1.7 eV i.e. 2.125 times), the A^* parameter is lowered by a factor of $c = 0.85$, the desorbed ions are singly charged and have the characteristics of solvated Na^+ ions extracted experimentally ($m = 275$ amu, $q/m = 350{,}000$ C/Kg). The results for three flow rates $(Q = 4, 3, 2) \times 10^{-11} m^3/s$ are seen in figure 7-7. The decreasing flow rates result in thinner jet radii as expected, coupled with an increase in peak normal external field E_n^o which in turn results in a higher ion current density, j_i.

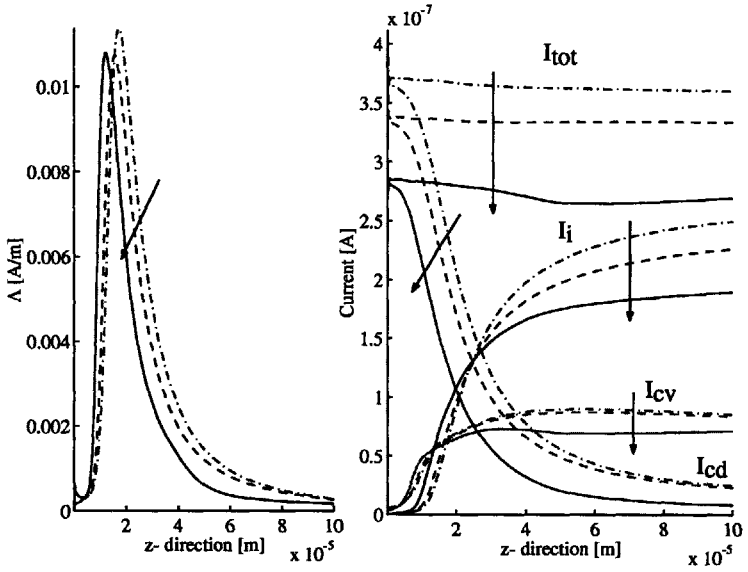

Figure 7-8: Results for ion evaporation using Higuera's method. Plots show spatial evolution relative to z-axis. Left: ion current per unit length; right: current plots: ion current I_i, convection current I_{cv}, conduction current I_{cd}, and total current $I_{tot} = I_i + I_{cv} + I_{cd}$. Arrows point towards lower flow rates $(Q = 4, 3, 2) \times 10^{-11} m^3/s$

The emitted currents for the same computational results are shown in figure 7-8. Notice two opposing trends: first the jet radius (h) will become smaller for decreasing flow rates; and second the ion evaporation current density (j_i) increases for decreasing flow rates. The relevance of this becomes apparent when one realizes that the ion current per unit length is $\lambda = 2\pi j_i h$. Our results show that for this artificially low G_0 and c parameter the jet radius still dominates over the ion evaporation effect and therefore when integrated to obtain I_i it gives the wrong trend, see figure 7-8. From these results, the conclusion is that the artificial values for the solvation energy are too high, and therefore the results are what one would expect. It may be that the values used for G_0 and c in these results may not be the necessary ones to obtain a proper ion evaporation behavior.

Again, this feels like playing God, but taken with a grain of salt this results may point to a qualitatively coherent picture of the onset of ion evaporation.

7.3 Summary

The first results obtained with the ion evaporation model showed some of the trends expected. However, the current vs flow rate results were not physically correct. The ion current keeps decreasing as the flow rate decreases instead of growing as experimental data shows. Although this results are not the best, at least the stage has been set for future work on this subject.

Chapter 8

Conclusions and recommendations

Every work has its beginning and its end, which we are often reluctant to accept. Perhaps this is so because endings often feel abrupt, a bit unnatural. I believe that this applies to research as well, how could a work end when so much still needs, cries, to be learned? Perhaps the right way to think about this, so the cliche says, is that it is like running where there really is no finish line, but only times when we stop to rest. There are always new things to learn and for me, that is the beauty of research.

8.1 Conclusions

This work picked up where Prof. Martínez-Sánchez and Vadim Khayms stopped and through it all we have learned many things. If any, in the next few paragraphs we provide a short summary of those things we have learned. Some of them are related to the physics of the problem, others to the mathematics and numerics of it, and a few others are nothing but comments and suggestions that may, hopefully, make someone else's work easier.

From the onset of the project I have seen this electrostatically accelerated jet as a subset of the more general problem of free jets. The equations we use to describe the colloid thruster are valid both for charged and uncharged jets. This point of view, is what originally drove us to consider the inclusion of viscous effects in our equations even if for the most part the electric current is a very weak function of it.

From the beginning of this project we have tried to compare and contrast our numerical results with existing experimental data, and theoretical estimates. Fortunately, in many

cases our results have compared favorably to others people's work. In what follows a short list of some of the comparisons made and used to benchmark our results:

- Comparison to current and flow rate experimental data
- Comparison to theoretical estimates of current, liquid properties, and flow rate
- Comparison to analytical estimates of jet diameter, and e-field at the jet and cone section
- Reproduced qualitative current vs Voltage behavior
- Analysis of transition length scales vs cone-jet transition radius, showed same trends as experimental data
- Qualitative cone-angle behavior as function of voltage
- Electrode effects as secondary variable
- Weak viscous effect on current

This benchmarking process along with the analysis of our results is treated in detail in chapter 6 and 7. In some cases, our results did not uncover new phenomena, but did confirm what has been seen experimentally and from other simplified models. In other words, some of the results we have obtained may have been hinted, or predicted via simplified models, in those cases the value of our results is that without making the simplifying assumptions we have reproduced that particular part of the cone-jet physics. What is valuable is that this code may be used to explore the range of validity of some of the assumptions made in simplified cases. This in turn allows us to gain a deeper understanding of the subject matter.

8.2 Recommendations

All this is good, but one cannot underestimate the importance of the numerical side. For this case, it may well be that we may have obtained as much mileage as we could from the Runge-Kutta solver. A better approach, which would allow calculations for even stiffer problems (i.e. low flow rates and high conductivities) would be a semi-implicit or implicit

solver. Said solver, would have to make use of an adaptive grid generator (already part of this work.) The overhead of implicit and semi-implicit codes is higher, but in the event of breakup may be the right choice.

Practical considerations are important, these are the ones that in the long run make our life easier. The conical version of the equations we have used remains a more natural way to describe the problem, but I believe that the simplicity of the cylindrical formulation constitutes a better compromise between accuracy and simplicity. Not to mention that cylindrical version of the flow equations may be more amenable to higher order approximations than the conical one.

The electrostatic part of the problem is currently solved using a panel method. This is perhaps a good compromise for those cases where space charge is not a concern. If however, one wishes to explore those cases where this effects are important it would pay off to seek alternatives. I think that pragmatism in this case is the answer. We are interested in the physics, not the advancement of numerical schemes. Other works have used third party Poisson solvers porting information between their code and the commercial code. Sometimes it is not worthwhile to reinvent the wheel.

8.3 Future work

The ion evaporation section of this work marks only the first steps in this direction. Clearly, the topic is rich and many things need to be done. First, and most important some means for reaching the required E-field must be found (1 V/nm). A second approach, may be through proper scaling of the solvation energy. At this point it is not clear, which path may be easier.

Ohmic dissipation along the jet may have an impact on the temperature distribution of the jet. Whether this will change dramatically the ion evaporation behavior remains to be seen, but it should not be forgotten.

Jet breakup and drop formation Even though jet breakup is beyond the scope of this work, we should point out that at least the some of the groundwork for this has been done. I think that one of the more exciting aspects for future work in this code , or similar code would be to address the jet breakup scenario. The information that could be obtained in that case would be invaluable for plume codes as their upstream boundary condition. Such

a code would also be capable of exploring the physics of main and satellite droplets as well as the nature of their charging. Another interesting aspect would be that a code that can deal with breakup may explore the physics of ion emission from the breakup point, droplets, and meniscus emission.

Bridging the gap between colloid and FEEP thrusters As mentioned by Lozano, this may be one of the most interesting problems. The physics of FEEP's and colloid thrusters are not that different. This problem would most likely benefit from a non-dimensional set of equations, since scales will change dramatically. In our experience the solver (the RK4), as would be expected, can cope only with some degree of stiffness. A rule of thumb may be that the solver starts to have problems once the ratio of maximum to minimum radii reaches a value of about 30. The message is, that designing a simulation that may bridge this gap will require careful thought about the numerical schemes.

Bibliography

[1] M.P. Brenner, J. Eggers, K. Joseph, S.R. Nagel, and X. Shi. Breakdown of scaling in droplet fission at high reynolds number. *Physics of Fluids*, 9(6):1573–1590, 1997.

[2] J.A. Carretero, M. Martínez-Sánchez, and F.J. Higuera. Numerical simulation of a single-emitter taylor cone electrospray. 2004. In preparation.

[3] S. Chapman. Carrier mobility spectra of spray electrified liquids. *Physical Review*, 52:184–190, 1937.

[4] D.-R. Chen and D.Y.H. Pui. Experimental investigation of scaling laws for electrospraying: dielectric constant effect. *Journal of Aerosol Science and Technology*, 27, 1997.

[5] D.K. Cheng. *Fundamentals of Engineering Electromagnetics.* Addison-Wesley, 1993.

[6] L.T. Cherney. Structure of taylor cone-jets: limit of low flow rates. *Journal of Fluids Mechanics*, 378:167–196, 1999.

[7] M. Cloupeau and B. Prunet-Foch. Electrohydrodynamic spraying functioning modes: a critical review. *Journal of Aerosol Science*, 25(6):1021–1036, 1989.

[8] E. Cohen, C.J. Somol, and D.A. Gordon. A 100kv, 10 w heavy particle thruster. In *Paper AIAA 65-377, AIAA 2dn Annual Meeting*, San Francisco, CA, 1965.

[9] J. Eggers. Nonlinear dynamics and breakup of free surface flows. *Reviews of modern physics*, 69(3):865–929, 1997.

[10] J. Eggers and T.F. Dupont. Drop formation in a one-dimensional approximation of the navier-stokes equations. *Journal of fluid mechanics*, 262:205–221, 1994.

[11] J.J. Feng. The stretching of an electrified non-newtonian jet: a model for electrospinning. *Physics of Fluids*, 14(11):3912–3926, 2002.

[12] J.B. Fenn, M. Mann, C.K. Meng, S.K. Wang, and C. Whitehouse. Electrospray ionization for mass spectrometry of large biomolecules. *Science*, 246:64–71, 1989.

[13] J. Fernández de la Mora and I.G. Loscertales. The current emitted by highly conducting taylor cones. *Journal of fluid mechanics*, 260:155–184, 1994.

[14] R.G. Forbes. Liquid-metal ion sources and electrosprays operating in the cone-jet mode: some theretical comparisons and comments. *Journal aerosol science*, 31(1):97–120, 2000.

[15] A. Gañán Calvo. Cone-jet analytical extension of taylor's electrostatic solution and the asymptotic universal scaling laws in electrospraying. *Physical Review Letters*, 79(2):217–220, 1997.

[16] A. Gañán Calvo. The surface charge in electrospraying: its nature and its universal scaling laws. *Journal of Aerosol Science*, 30(7):863–872, 1999.

[17] A. Gañán Calvo. On the general scaling theory for electrospraying. *Journal of Fluid Mechanics*, 507:203–212, 2004.

[18] A. Gañán Calvo, J. Davila, and A. Barrero. Current and droplet size in the electrospraying of liquids. scaling laws. *Journal of Aerosol Science*, 28(2):249–275, 1997.

[19] A. Gañán Calvo, C. Pantano, and A. Barrero. The equilibrium shapes of liquid menisci emitting liquid and charges in steady cone–jet mode. *Journal of Aerosol Science*, 27:S187–S188, 1996.

[20] M. Gamero-Castaño. Electric-field-induced ion evaporation from dielectric liquid. *Physical Review Letters*, 89(14), 2002.

[21] M. Gamero-Castaño and J. Fernández de la Mora. Direct measurement of ion evaporation kinetics from electrified liquid surfaces. *Journal of Chemical Physics*, 113(2):815–832, 2000.

[22] M. Gamero-Castaño and V. Hruby. Electric measurement of charged sprays emitted by cone-jets. *Journal of fluid mechanics*, 459:245–276, 2002.

[23] R. Gomer and L.W. Swanson. Theory of field desorption. *The journal of chemical physics*, 38(7), 1963.

[24] J.M. Grace and C.M. Marijnissen. A review of liquid atomization by electrical means. *Journal of aerosol science*, 25(6), 1994.

[25] A.E. Green. On the non-linear behavior of fluid jets. *Int. J. Eng. Sci.*, 14:49–63, 1976.

[26] Private communication with Bob Haimes, Principal Research Engineer ACDCL, Aero-Astro, MIT.

[27] R.P.A. Hartmann, D.J. Brunner, D.M.A. Camelot, J.C.M. Marijnissen, and B. Scarlett. Electrohydrodynamic atomization in the cone-jet mode. physical modeling of the liquid cone and jet. *Journal of Aerosol Science*, 30(7):823–849, 1999.

[28] F.J. Higuera. Flow rate and electric current emitted by a taylor cone. *Journal of Fluid Mechanics*, 484:303–327, 2003.

[29] F.J. Higuera. Ion evaporation from the surface of a taylor cone. *Physical Review E*, 68:016304–1–10, 2003.

[30] C. Hirsch. *Numerical computation of internal and external flows, Vol. 1.* John Wiley and Sons, 1992.

[31] C. Hirsch. *Numerical computation of internal and external flows, Vol. 2.* John Wiley and Sons, 1992.

[32] M. Hohmann, M. Shin, G. Rutledge, and M. Brenner. Electrospinning and electrically forced jets. ii. applications. *Physics of Fluids*, 13(8):2221–2236, 2001.

[33] J.V. Iribarne and B.A. Thompson. On the evaporation of small ions from charged droplets. *Journal of Chemical Physics*, 64(6):2287–2294, 1976.

[34] Note: The speficic impulse ($I_{sp} \approx c/g$), where c is the particle exhaust speed and g is gravity's acceleration. Isp can be interpreted is the total impulse per unit weight of propellant. Typical chemical rockets have $I_{sp} \approx 200 - 300$ sec while electric propulsion systems tend to have $500 < I_{sp} < 10000$ seconds.

[35] A. Jameson, W. Schmidt, and E. Turkel. Numerical solution of the euler equations by finite volume methods using runge kutta time stepping schemes. In *AIAA 5th computational fluid dynamics conference, Meeting Paper 81-1259*, 1981.

[36] J.T. Jeong and H.K. Moffatt. Free-surface cusps associated with flow at low reynolds number. *Journal of fluid mechanics*, 241:1–22, 1992.

[37] D.D. Joseph, J. Nelson, and M. Renardy. Two-dimensional cusped interfaces. *Journal of fluid mechanics*, 223:383–409, 1991.

[38] V. Khayms. *Advanced propulsion for microsatellites.* PhD dissertation, MIT, Department of Aeronautics and Astronautics, 2000.

[39] P.W. Kidd and H. Shelton. Life test (4350 hrs.) of an advanced colloid thruster module. In *Paper AIAA 73-1078, AIAA 10th Electric Propulsion Conf.*, Lake Tahoe, NV, 1973.

[40] V.E. Krohn Jr. Liquid metal droplets for heavy particle propulsion. In *Progr. In Astronautics and Rocketry*, volume 5. A. C. Press, N. Y. London.

[41] L.D. Landau and E.M. Lifshitz. *Electrodynamics of continuous media.* Number 8 in Course of theoretical physics. Pergamon Press, Addison-Wesley Publishing Co.Inc., 1960.

[42] H.C. Lee. Drop formation in a liquid jet. *IBM J of Res and Dev*, 18(4):364–369, 1974.

[43] J.M. López-Herrera, A. Barrero, A. Boucard, I.G. Loscertales, and M. Márquez. An experimental study of the electrospraying of water in air at atmospheric pressure. *Journal of the American Society of Mass Spectrometry*, 15:253–259, 2004.

[44] J.M. López-Herrera and A.M. Gañán Calvo. A note charged capillary jet breakup of conducting liquids: experimental validation of a viscous one-dimensional model. *Journal of fluid mechanics*, 501:303–326, 2004.

[45] J.M. López-Urdiales. *Progress in Colloid Propulsion.* SM thesis, MIT, Department of Aeronautics and Astronautics, 2004.

[46] I.G. Loscertales and J. Fernández de la Mora. Experiments on the kinetics of field evaporation of small ions from droplets. *Journal of Chemical Physics*, 103(12):5041–5060, 1995.

[47] P. Lozano. *Studies on the ion-droplet mixed regime in colloid thrusters.* PhD dissertation, MIT, Department of Aeronautics February 2003.

[48] P. Lozano and M. Martínez-Sánchez. Jets and sprays emitted from colloid thrusters–experiments and modeling. In *Proc. 3rd International Conference on Spacecraft Propulsion*, Cannes France, October 2000.

[49] P. Lozano and M. Martínez-Sánchez. Experimental measurements of colloid thruster plumes in the ion-droplet mixed regime. In *AIAA Meeting Paper 2002-3814*, Indianapolis, IN, July 2002.

[50] O. Mangoubi and P. Lozano. Shape characterization of cone–jets under various operating conditions. Internal report Space Propulsion Lab, MIT.

[51] M. Martinez-Sanchez. Colloid thruster class notes, 16.522 mit.

[52] M. Martínez-Sánchez, J. Fernández de la Mora, V. Hruby, M. Gamero-Castaño, and V. Khayms. Research on colloid thrusters. In *26th International Electric Propulsion Conference*, Kitkyushu, Japan., October 1999.

[53] Maxwell 2D, from Ansoft Corp. Student version.

[54] D.W. Moore. Resonances introduced by discretization. *IMA Journal of Applied Mathematics*, 31:1–11, 1983.

[55] C. Pantano, A. Gañán Calvo, and A. Barrero. Zeroth-order electrohydrostatic solution for electrospraying in cone-jet mode. *Journal of Aerosol Science*, 25(6):1065–1077, 1994.

[56] D.H. Peregrine. Waves in beaches. In Meyer R. E., editor, *Waves in Beaches*, page 95. Academic Press, New York, 1972.

[57] P.D. Prewett and G.L.R. Mair. *Focused Ion Beams from Liquid Metal Ion Sources.* Wiley, New York,, 1991.

[58] L. Prókay. *Field desorption mass spectrometry.* Marcel Dekker, Inc.,, 1991.

[59] D.A. Saville. Electrohydrodynamics: The taylor-melcher leaky dielectric model. *Annual review of fluid mechanics*, 29:27–64, 1997.

[60] T.E. Stern, B.S. Gossling, and R.H. Fowler. Further studies in the emission of electrons from cold metals. In *Proceedings Royal Society A124(1929)*, 699.

[61] H.A. Stone and L.G. Leal. The influence of initial deformation on drop breakup in subcritical time–dependent flows at low reynolds numbers. *Journal of fluid mechanics*, 206:223–263, 1989.

[62] G.I. Taylor. Disintegration of water drops in an electric field. *Proc. R. Soc., London A*, 280:383–397, 1964.

[63] M. Tjahjadi, H.A. Stone, and J.M. Ottino. Satellite and subsatellite formation in capillary breakup. *Journal of Fluid Mechanics*, 243:297–317, 1992.

[64] F. Yan, B. Farouk, and F. Ko. Numerical modeling of an electrostatically driven liquid meniscus in the cone-jet mode. *Journal of Aerosol Science*, 34:99–116, 2003.

[65] J. Zeleny. Instability of electrified liquid surfaces. *Phys. Rev.*, 10:1–6, 1917.